Electromagnetic modeling of large and non-uniform planar array structures using Scale-Changing Technique (SCT)

Aamir Rashid

THÈSE

En vue de l'obtention du

DOCTORAT DE L'UNIVERSITÉ DE TOULOUSE

Délivré par *l'Université Toulouse III - INP Toulouse*
Discipline ou spécialité : *Micro-ondes Electromagnétisme et Optoélectronique*

Présentée et soutenue par *Aamir RASHID*
Le *21 Juillet 2010*

Titre : *Electromagnetic modeling of large and non-uniform planar array structures using Scale Changing Technique (SCT)*

JURY
M. Hervé AUBERT (Directeur de Thèse), Professeur, ENSEEIHT, LAAS, Toulouse
M. Ronan SAULEAU (Rapporteur), Professeur, IETR, Rennes
Mme. Elodie RICHALOT (Rapporteur), Maître de conférences, ESYCOM, Marne-la-Vallée
M. Jun-Wu TAO, Professeur, ENSEEIHT, Toulouse
M. Manos M. TENTZERIS, Professeur, ATHENA, Georgia Tech, Etats-Unis
M. Fabio COCCETTI, Docteur, NovaMEMS, LAAS, Toulouse
INVITED
M. André BARKA (ONERA) M. Maxime ROMIER (CNES)

Ecole doctorale : *Ecole Doctorale Génie Electrique, Electronique, Télécommunications (GEET)*
Unité de recherche : *Laboratoire d'Analyse et d'Architecture des Systèmes (LAAS)*
Directeur(s) de Thèse : *M. Hervé AUBERT*
Rapporteurs : *M. Ronan SAULEAU, Mme. Elodie RICHALOT*

To my parents

and my sisters Tahira and Aasia

ACKNOWLEDGEMENTS

The research work presented in this manuscript has been carried out at LAAS (Laboratoire d'Analyse et d'Architecture des Systèmes) as part of the Research Group MINC. I would first of all like to extend my gratitude to Mr. Raja CHATILA (Director LAAS) for welcoming me to this lab and Mr. Robert PLANA (Director Group MINC) for accepting me as a member of his research group.

I am highly indebted to Hervé AUBERT, my thesis advisor, who has proposed this research topic to me and has rigorously followed and contributed to my research work over the last three and a half years of my thesis. I would like to thank him for his availability for advice and discussion in spite of his charged schedule. He has been a constant source of inspiration through both the highs and lows of my thesis.

Special thanks go to Ronan SAULEAU (Université de Rennes 1) and Elodie RICHALOT (Université Paris-Est Marne-la-Vallée) for accepting to review my thesis as 'rapporteurs' on a very short notice. I highly appreciate their in-depth review of this manuscript and their detailed comments and remarks that greatly helped me to improve the quality of this manuscript.

I am equally grateful to Jun-Wu TAO (INP-Toulouse), Manos TENTZERIS (Georgia Tech), Fabio COCCETTI (NovaMEMS), André BARKA (ONERA) and Maxime ROMIER (CNES) for accepting to be the part of the evaluation committee of my thesis defense. I highly appreciate their keen interest in my work as well as their precious comments and questions during the course of my defense.

I cannot forget the help and encouragement I got from Nathalie RAVEU (ENSEEIHT-INP Toulouse) during the first year of my thesis. I thank her for helping me in understanding the theoretical concepts of Scale Changing Technique as well as the MATLAB codes.

I would also like to thank my colleagues Euloge TCHIKAYA, Fadi KHALIL, and Farooq Ahmad TAHIR for the help, discussions and collaboration regarding my research work. I would also like to acknowledge the help of Ahmad ALI MOHAMED ALI (regarding IE3D), Alexandru TAKACS (regarding FEKO), Gaetan PRIGENT (regarding HFSS) and Sami HEBIB throughout the course of my thesis.

I would also like to extend my thanks to Hervé LEGAY (THALES) who has helped and collaborated in this work and provided with numerous important suggestions.

I am equally indebted to Brigitte DUCROCQ (secretary Group MINC) for her help in dealing with all the administrative stuff that allowed me to concentrate on my work.

I will a lways be grateful for the support and encouragement that I received from my colleagues of Group MINC. I am thankful to all of them for providing a healthy and friendly work environment. My special thanks go to my office mates (Mai, Euloge, Farooq, Sami and Dina) for a great company and support.

I am extremely grateful to my parents for their encouragement, patience, support and prayers throughout my thesis and to my younger sister Aasia for her funny anecdotes and family updates that kept my spirits high during the stressful times.

I am very thankful to a number of my friends who have made my stay in Toulouse joyous and exhilarating. I would like to extend my thanks to Rameez Khalid and Asif Inam who helped me to settle when I was new in the city. I cannot thank enough my friend Naveed who has always been there ready to help and w hose delicious m eals I will alwa ys miss. I woul d also like to thank my friends A li Nizam ani, Usman Zabit, Ahmad Hayat, Mohamed Cheikh, Assia Belbachir, Lavindra de silva for such a great time.

Last but not the least I would like to acknowledge the financial support by Thales Alenia Space and Regional council of Midi-pyrennes wit hout which this research work would not have been possible.

TABLE OF CONTENTS

ABSTRACT

GENERAL INTRODUCTION

SECTION I: THEORY OF SCALE-CHANGING TECHNIQUE

SECTION II: ELECTROMAGNETIC MODELING USING SCALE-CHANGING TECHNIQUE (SCT)

APPENDIX B

THESIS SUMMARY (FRENCH)

REFERENCES

PUBLICATIONS

ABSTRACT

Large sized planar structures are increasingly being employed in satellite and radar applications. Two major kinds of such structures i.e. FSS and Reflectarrays are particularly the hottest domains of RF design. But due to their large electrical size and complex cellular patterns, full-wave analysis of these structures require enormous amount of memory and processing requirements. Therefore conventional techniques based on linear meshing either fail to simulate such structures or require resources not available to a common antenna designer. An indigenous technique called Scale-changing Technique addresses this problem by partitioning the cellular array geometry in numerous nested domains defined at different scale-levels in the array plane. Multi-modal networks, called Scale-changing Networks (SCN), are then computed to model the electromagnetic interaction between any two successive partitions by Method of Moments based integral equation technique. The cascade of these networks allows the computation of the equivalent surface impedance matrix of the complete array which in turn can be utilized to compute far-field scattering patterns. Since the computation of scale-changing networks is mutually independent, execution times can be reduced significantly by using multiple processing units. Moreover any single change in the cellular geometry would require the recalculation of only two SCNs and not the entire structure. This feature makes the SCT a very powerful design and optimization tool. Full-wave analysis of both uniform and non-uniform planar structures has successfully been performed under horn antenna excitation in reasonable amount of time employing normal PC resources.

GENERAL INTRODUCTION

The accurate prediction of the plane wave scattering by finite size arrays is of great practical interest in the design and optimization of modern frequency selective surfaces, reflectarrays and transmittarrays. A complete full-wave analysis of these structures demands enormous computational resources due to their large electrical dimensions which would require prohibitively large number of unknowns to be resolved. Thus the unavailability of efficient and accurate design tools for these applications limits the engineers with the choice of low performance simplistic designs that do not require enormous amount of memory and processing resources.

Moreover the characterization of large array structures would normally require a second step for optimization and fine-tuning of several design parameters since the initial design procedure assumes several approximations e.g. in the case of reflectarrays the design is usually based on a single cell scattering parameters under normal incidence, which is not the case practically. Therefore a full-wave analysis of the initial design of the complete structure is necessary prior to fabrication, to ensure that the performance conforms to the design requirements. A modular analysis technique which is capable of incorporating small changes at individual cell-level without the need to rerun the entire simulation is extremely desirable at this stage.

Historically several approaches have been followed when analyzing large planar structures [Huang07]. In the case of uniform arrays, where we have periodicity in the geometry, an infinite approach is often used. By using Floquet's theorem, the analysis is effectively reduced to solving for a single unit-cell; thus significantly reducing the unknowns and therefore the simulation times [Pozar84] [Pozar89]. Although the periodic boundary conditions take into account the effect of mutual coupling in the periodic environment, the approximation may not hold for the arrays where individual cell geometries are very different. In addition this is a very poor approximation for the cells lying at the edges of the array.

A simple method based on Finite Difference Time Domain (FDTD) technique has been proposed to precisely account for the mutual coupling effects. It consists of illuminating a single cell in the array in the presence of nearest neighbor cells and calculating the reflected wave. Though it allows precise excitation and boundary conditions for each cell in the array it is not very practical to design large arrays due to extremely long execution times [Cadoret2005a].

Different conventional methods have been tested for a full-wave analysis of periodic structures e.g. Method of Moments (MOM) used in the spectral domain for multilayered structures [Mittra88] [Wan95], Finite Element Method (FEM) [Bardi02] and FDTD [Harms94]. But all of these methods would require prohibitive resources for the cases where the local periodicity assumption cannot be applied. A spectral domain immitance approach has been used in the full-wave analysis of a 2-D planar dipole array along with the Galerkin's procedure using entire domain basis functions [Pilz97].

The method of moments for the global electromagnetic simulation of finite size arrays requires high CPU time and memory especially when the patch geometries are non-canonical and therefore sub-domain basis functions have to be used. The memory problem may be resolved by using various iterative techniques (e.g. Conjugate Gradient iterative approach) [Sarkar82] [Sarkar84] at the cost of further increase in the execution time. A promising improvement of the MOM, called the *Characteristic Basis Method of Moment* was proposed for reducing the execution

time and memory storage for large-scale structures [Mittra05] [Lucente06]. However the convergence of numerical results remains delicate to reach systematically.

In order to overcome the above-mentioned theoretical and practical difficulties, an original monolithic formulation for the electromagnetic modeling of multi-scale planar structures has been proposed [Aubert09]. The power of this technique called the *Scale-changing Technique (SCT)* comes from the modular nature of its problem formulation. Instead of modeling the whole planar-surface as a single large discontinuity problem, it is split into a set of many small discontinuity problems each of which can be solved independently using mode-matching variational methods [Tao91]. Each of the sub-domain discontinuity solution can be expressed in the matrix form characterizing a multiport-network called *Scale-Changing Network* (SCN). SCT models the whole structure by interconnecting all scale-changing networks, where each network models the electromagnetic coupling between adjacent scale levels.

The cascade of Scale Changing Networks allows the global electromagnetic simulation of all sorts of multi-scaled planar geometries. The global electromagnetic simulation of structures via the cascade of scale-changing networks has been applied with success to the design and electromagnetic simulation of specific planar structures such as multi-frequency selective surfaces of infinite extent [Voyer06], discrete self-similar (pre-fractal) scatterers [Voyer04] [Voyer05], patch antennas [Perret04] [Perret05] and reconfigurable phase-shifters [Perret06] [Perret06a]. The objective of this work is to validate SCT in the case of various planar array geometries including FSS arrays, reflectarrays and transmittarrays.

Another modular approach based on spectral-domain MOM has been used in the case of multilayer periodic structures [Wan95] which consists of characterizing each array layer by a generalized scattering matrix (GSM) and then analyzing the complete structure by a simple cascade of these GSMs. SCT differs from this approach because in case of SCT partitioning is applied to the same array-plane and therefore SCT is applicable for the single-layer array problems. For multilayer arrays SCT can be used in hybrid with the fore-mentioned approach for the efficient modeling of more complex electromagnetic problems e.g. in the case of variable

sized stacked patch-arrays [Encinar99] [Encinar01] [Encinar03] and aperture-coupled arrays [Robinson99] [Keller00].

This thesis is divided into two main sections. In the first section the theory behind the scale-changing technique is presented in a general context using an example of a generic discontinuity plane. Several concepts related to the technique are introduced and elaborated. How the discontinuity problem can be expressed in terms of equivalent circuit components is demonstrated [Aubert03]. The problem is then formulated in terms of matrix equations from this equivalent circuit and solved using MOM based technique. The second part of this section demonstrates the application of SCT to periodic reflectarrays.

In the second section of the thesis, SCT is used to model finite and non-uniform single layered planar arrays. First it is shown that SCT effectively models the electromagnetic coupling between the neighboring cells of an array. Later the technique is used to model linear arrays of non-uniform metallic strips and patches. The simulation results as well as the simulation times are compared to the classic simulation tools. Finally, SCT is applied to find the free-space diffraction patterns of two-dimension planar arrays. Both uniform and non-uniform arrays are simulated under plane-wave and horn-antenna excitations and the scattering field plots are compared to results obtained by other techniques.

SECTION I:

THEORY OF SCALE-CHANGING TECHNIQUE

I.1. INTRODUCTION

Presently the most common method to compute the scattering fields from the planar structures is by solving the integral equation formulation of the Maxwell's equations. This approach permits to express the open boundary electromagnetic problem in terms of an integral equation formulated over the finite planar surface. This reduction of one spatial dimension makes this method very efficient in the case of planar geometries. Yet this method in its traditional formulation is not particularly adapted for large planar structures containing scaled geometries and complex metallic patterns. Rapid and fine-scale variations in the structure geometry can cause abrupt changes in electromagnetic field patterns requiring local meshing at a very minute scale which in turn would require immense storage and computational resources.

We propose to resolve this problem by introducing local description of fields for different regions of the planar surface. The procedure can be outlined in the following steps:

1) The planar surface is decomposed in several sub-domain surface regions.
2) The electromagnetic fields are expressed on the modal-basis of each of these sub-domains bounded by their respective boundary conditions.

3) Modal contributions are treated separately for lower order modes and higher order modes. Higher order modes are considered to contribute only locally where as lower order modes define coupling with the domain at the higher scales.
4) Electromagnetic coupling between two successive scales is modeled by a scale-changing network defined by the lower order modes of the two sub-domains.
5) A global electromagnetic solution is obtained by a simple cascade of these scale-changing networks.

These concepts will be explained in further detail in the subsequent sections.

I.2. SCALE-CHANGING TECHNIQUE (SCT)

I.2.1. Introduction

Electrically large (many orders of the wavelength) structures e.g. multiband frequency selective surfaces, non-uniform reflectarrays and self-similar fractal structures are said to be complex when their geometrical dimensions vary over a large range of scale. In other words we have very fine patterns and large patterns in the same structure. As mentioned previously linear meshing in these structures requires tremendous amount of computational resources and may lead to ill-conditioned matrices.

The higher the number of scale-levels the higher is the complexity. Scale-changing technique (SCT) gets its name from scaled partitioning of the planar structure and the modeling of the electromagnetic interactions between these scale-levels [Aubert09]. In this section we will focus on the electromagnetic simulation of a generic multi-scale structure consisting of metallic patterns printed on a dielectric planar surface.

I.2.2. Discontinuity Plane

To understand the concepts and workings of the Scale-changing Technique we will study a general case of an arbitrary discontinuity. Consider multiple metallic patterns with the dimension varying over a wide range of scale, printed on a planar dielectric surface. Suppose that the largest patterns are several orders of magnitude bigger than the finest patterns. This discontinuity plane may be modeled by placing it at a cross-section of a waveguide or can simply be located in the free-space. The two half-regions i.e. the left-hand region and the right hand region are assumed to be composed of multilayered and loss-less dielectric media.

I.2.2.1. Partitioning of the Discontinuity Plane

The starting point of proposed approach involves the coarse partitioning of the discontinuity plane domain into large sub-domains of arbitrary shape and comparable sizes. This partitioning step corresponds to the first order of the magnitude of discontinuity plane patterns. The second step consists of partitioning each of the domains formed in the first step by introducing smaller sub-domains of comparable sizes corresponding to the next order of magnitude. This procedure of partitioning the domains into smaller sub-domains is repeated until the smallest scale is reached. Such hierarchical domain-decomposition allows rapid focusing on increasing details of the planar geometry unlike a linear meshing approach.

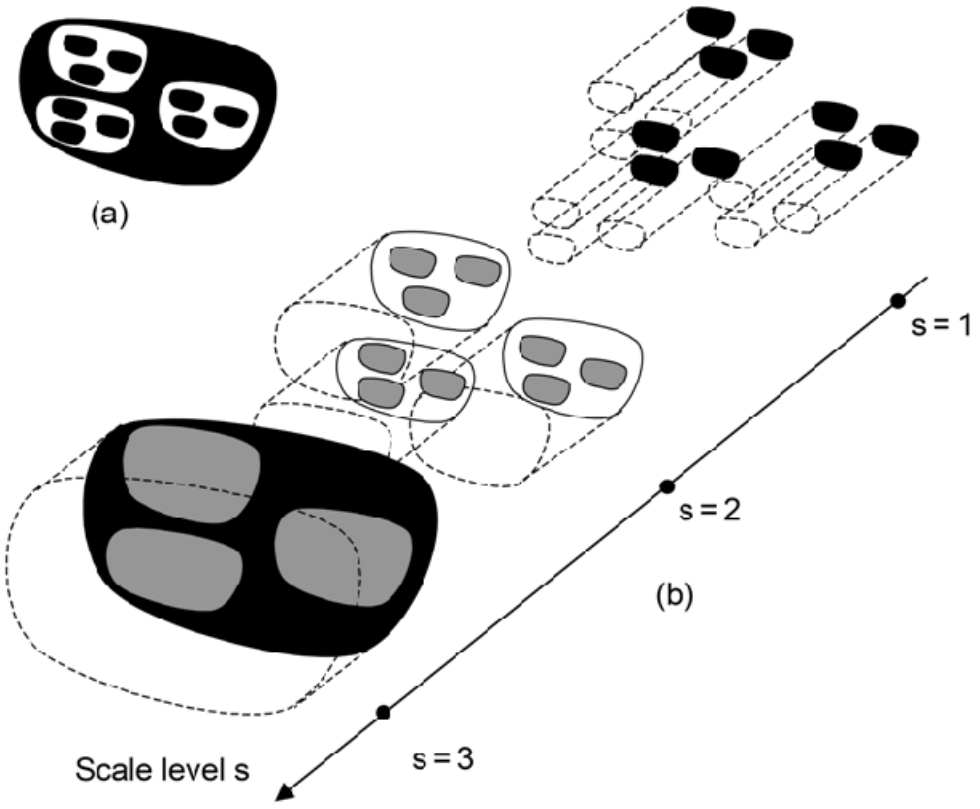

Figure I.1: An example of discontinuity plane presenting 3 scale-levels (black is metal and white is dielectric) and the scattered view of the various sub-domains generated by the partitioning process

This manner of partitioning allows us to define separate scale-levels for the co-planar domains and sub-domains and this can be represented as shown in

Figure- I.1. The smallest sub-domains are assigned the bottom most scale or scale-level one whereas the largest domain i.e. the entire discontinuity plane gets the highest scale-level $\mathbf{s_{max}}$. It is important to note that the scattered representation of the domains is only for the sake of clarity, essentially all the domains and sub-domains lie in the same plane.

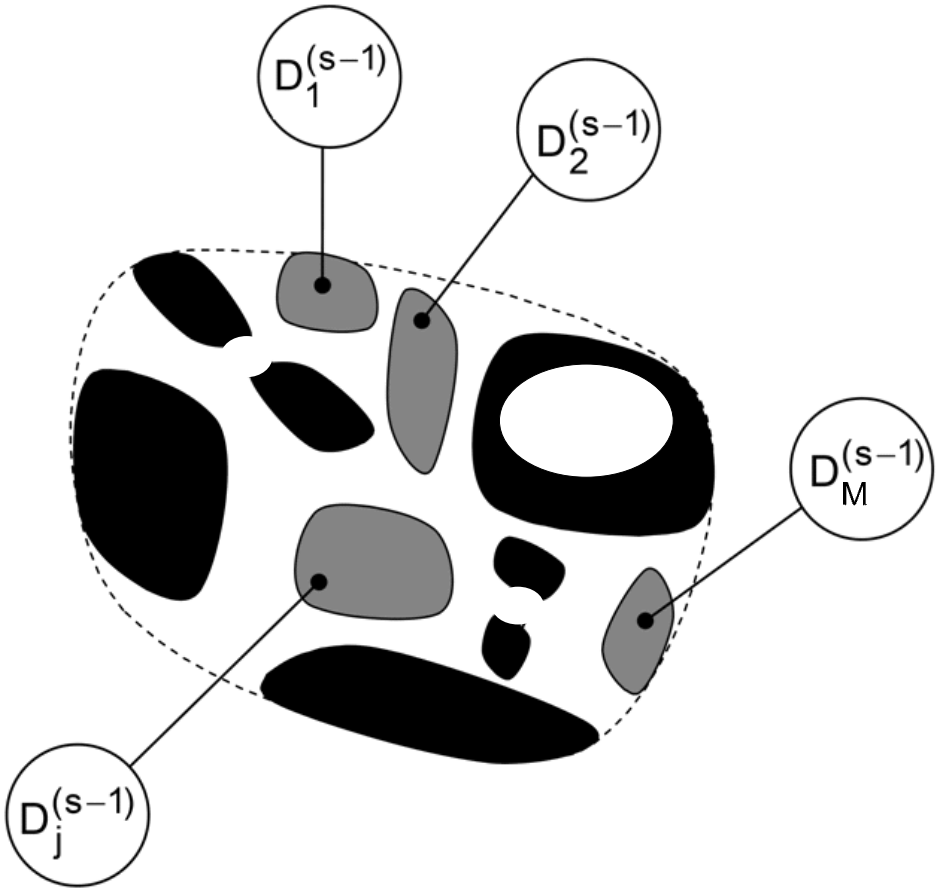

Figure I.2: The *i*th generic domain resulting from the partition process at scale level 's' (black is metal, white is dielectric and grey indicates the location of sub-domains $\mathbf{D_j^{(s-1)}}$ (with j = 1, 2, … , M)

Let's consider once again the case of the generic discontinuity plane of Figure-I.2. Assuming it to be the $\boldsymbol{i}$th domain of a general scale-level $\mathbf{s}$ it can be denoted for convenience as $\mathrm{D_i^{(s)}}$. where, $\mathrm{i} = 1 - N$, N being the total number of domains at the scale-level $\mathbf{s}$. And $\mathbf{s}$ ranging from 1 to $\mathbf{s_{max}}$. Using the above described partitioning procedure it can be decomposed into M sub-domains denoted

by $D_j^{(s-1)}$, (where $j = 1 - M$) defined at scale-level $\mathbf{s - 1}$. In addition the discontinuity plane may contain simple metallic and dielectric domains where further partitioning is not needed [Aubert09].

I.2.2.2. Choice of Boundary Conditions:

Artificial boundary conditions are introduced along the contours of all these domains and sub-domains. These boundary conditions are introduced only on the contours of the sub-domains lying in the discontinuity plane and not in the two half-regions on each side of this discontinuity. The boundary conditions are selected from

1) Perfect Electric Boundary Conditions (PEC)
2) Perfect Magnetic Boundary Conditions (PMC)
3) A combination of the above two conditions
4) Periodic Boundary Conditions (PBC)

The physics of the problem should be considered in the choice of the boundary conditions around any domain. In practice boundary conditions can be tried on the contours of each sub-domain and tested for accuracy, execution time and numerical convergence depending on a particular geometry.

The purpose of introducing the boundary conditions at the sub-domain level is essentially to define a new boundary value problem at a local level that can be solved independently by expressing the tangential fields in the region on the modal-basis respecting these boundary conditions. At sub-domain level each boundary value electromagnetic problem is resolved by writing the field equations in integral equation formulation and applying the Galerkin's method to solve for the surface fields and currents.

Since now we have many smaller independent problems, the number of unknowns in the matrix equations are reduced and therefore much less memory resources are required. It is to be noted here that due to introduction of artificial boundary condition the scale-changing technique is not an exact technique but an

approximate method. And these approximations need to be chosen carefully not to significantly perturb the accuracy of the solution [VoyerTh].

I.2.2.3. Field Expansion on Orthogonal Modes:

In the sub-domain $\mathrm{D}_{\mathrm{i}}^{(\mathrm{s})}$ bounded by the artificial boundary conditions the modal expansion of the tangential electromagnetic field can be performed. Therefore the $\boldsymbol{n}$th mode of the modal basis $\vec{\boldsymbol{F}}_{\boldsymbol{n}}^{(\boldsymbol{i},\boldsymbol{s})}$ is solution to the following Helmholtz equation [Collin91].

$$\left[\nabla_T^2 \; + \; k_n^{(i,s)^2}\right] \vec{\boldsymbol{F}}_{\boldsymbol{n}}^{(\boldsymbol{i},\boldsymbol{s})} = \vec{0} \qquad \textbf{(I.1)}$$

In the above equation ∇_T^2 is the transverse Laplacian operator and $k_n^{(i,s)}$ is the cut-off wave-number of the nth mode of the ith sub-domain of the sth scale-level i.e. $\mathrm{D}_{\mathrm{i}}^{(\mathrm{s})}$. The $\vec{\boldsymbol{F}}^{(\boldsymbol{i},\boldsymbol{s})}$ is the orthogonal modal-basis which satisfies the boundary conditions at the contours of the sub-domain. The condition of orthognality dictates;

$$\langle \vec{\boldsymbol{F}}_{\boldsymbol{m}}^{(\boldsymbol{i},\boldsymbol{s})}, \vec{\boldsymbol{F}}_{\boldsymbol{n}}^{(\boldsymbol{i},\boldsymbol{s})} \rangle = \iint_{D_i^{(s)}} \left[\vec{\boldsymbol{F}}_{\boldsymbol{m}}^{(\boldsymbol{i},\boldsymbol{s})}\right]^* \cdot \vec{\boldsymbol{F}}_{\boldsymbol{n}}^{(\boldsymbol{i},\boldsymbol{s})} ds = \begin{Bmatrix} 0 & for\ m \neq n \\ A_{mn} & for\ m = n \end{Bmatrix} \qquad \textbf{(I.2)}$$

The $*$ operator represents the complex conjugate. And ***m*** and ***n*** are any two modal indexes of the orthogonal modal basis $\vec{\boldsymbol{F}}^{(\boldsymbol{i},\boldsymbol{s})}$.

I.2.2.4. Active and Passive Modes:

Now that we have the modal representation of the tangential electromagnetic field in the sub-domain, the field contributions due to lower-order and higher-order modes can be treated separately. As the order of the modes increases, the energy diffracted at the metal interface for that harmonic becomes more and more localized within the vicinity [Collin91]. Therefore it is safe to assume that after a certain number

of modes, the higher order modes will contribute only to very fine-scale variations of the electromagnetic field that are localized to that particular sub-domain. On the other hand the lower order modes describe the large-scale variations of the field that couples with the tangential fields of the sister sub-domains.

For example in case of the generic sub-domain $\mathrm{D}_{\mathrm{i}}^{(\mathrm{s})}$ the fine-scale variations are described as a linear combination of infinite number of higher-order modes of $\vec{\boldsymbol{F}}_{\boldsymbol{n}}^{(\boldsymbol{i},\boldsymbol{s})}$which are spatially localized in the vicinity of discontinuities, sharp edges and various contours of the domain and therefore does not significantly contribute to the electromagnetic coupling between the various sub-domains $\mathrm{D}_{\mathrm{j}}^{(\mathrm{s}-1)}$. For this reason these higher-order modes are called *passive modes*.

The large-scale contribution to the field in $\mathrm{D}_{\mathrm{i}}^{(\mathrm{s})}$ is due to the electromagnetic coupling between the constitutive sub-domains $\mathrm{D}_{\mathrm{j}}^{(\mathrm{s}-1)}$. This coupling can be modeled as the combination of only a limited number of lower-order modes in the spectral domain. Because these lower-order modes are involved in the description of electromagnetic coupling they are called *active modes*. Finally, the coupling between the active modes of the domain $\mathrm{D}_{\mathrm{i}}^{(\mathrm{s})}$ and the passive modes of sub-domains $\mathrm{D}_{\mathrm{j}}^{(\mathrm{s}-1)}$ is very weak due to the large difference in their spatial frequencies.

It follows from the above-mentioned physical considerations that the electromagnetic coupling between two subsequent scale-levels, e.g. the scale-level $\boldsymbol{s}$ and the lower scale $\boldsymbol{s}-\boldsymbol{1}$, can be defined in term of the mutual interactions of the active modes of the domain $\mathrm{D}_{\mathrm{i}}^{(\mathrm{s})}$ and the active modes of the sub-domains $\mathrm{D}_{\mathrm{j}}^{(\mathrm{s}-1)}$.

I.2.3. Scale-changing Network (SCN)

The mutual coupling of the active modes described in the previous section can be represented by a multiport of Figure I.3. Each port in the network represents an active mode. The ports on the left hand side models the active modes in domain $\mathrm{D}_{\mathrm{i}}^{(\mathrm{s})}$ whereas the M set of ports on the right hand side denote the active modes of M sub-

domains $D_j^{(s-1)}$(where $j = 1 - M$) of scale level $\mathbf{s-1}$. As this multiport allows to relate the fields at scale s to fields at the lower scale s-1, it is named the *Scale-changing network (SCN)*.

For relating the electromagnetic fields at scale $\mathbf{s}$ to that of another scale $\mathbf{s-2}$, the interconnection of scale-changing networks may be performed as shown in Figure I.4, each network being previously computed separately. Consequently, the modeling of interaction among the multiple scales of a complex discontinuity plane is reduced to simple cascade of appropriate scale-changing networks, where each network models the interaction between two scales.

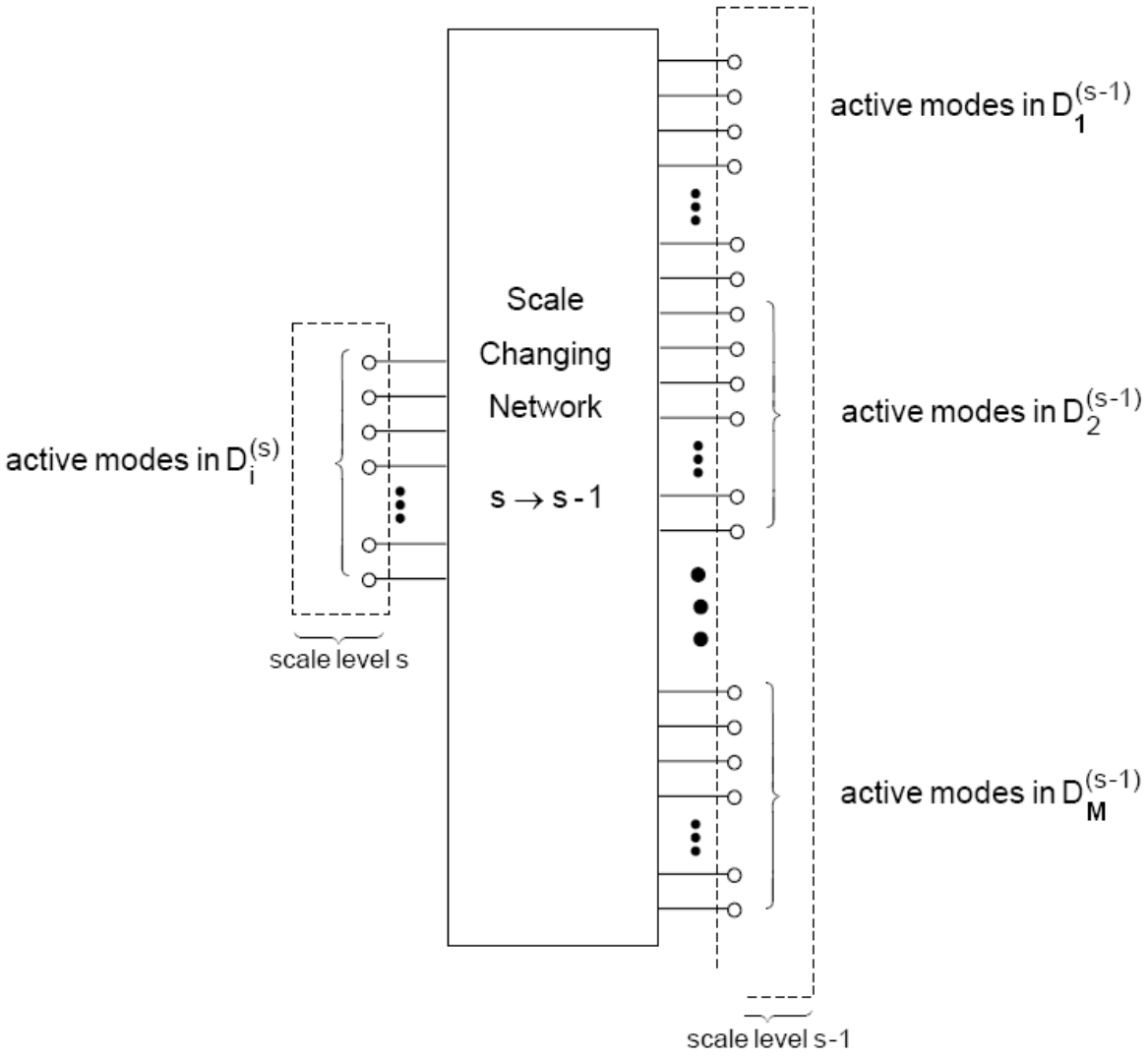

Figure I.3: The Scale Changing Network coupling the active modes in the domain $\mathbf{D_i^{(s)}}$ (scale level s) and its constitutive sub-domains $\mathbf{D_j^{(s-1)}}$ (scale level s–1)

It is important to note that the computation of these scale-changing networks is mutually independent. Therefore each network can be computed by using a separate processing node. This modular nature of scale-changing technique can be exploited in multiprocessing environments to cut simulation times in the case of very large and complex structures. Moreover any single change at any scale-level will only need the re-computation of two scale-changing networks and not the SCNs for all other scales. This means that small geometric changes will not require the entire simulation of the structure all over again. This feature is an essential quality of a good parametric tool. Therefore SCT designs will have the capability of rapid simulations in the cases where the effects of certain modifications are studied on the design.

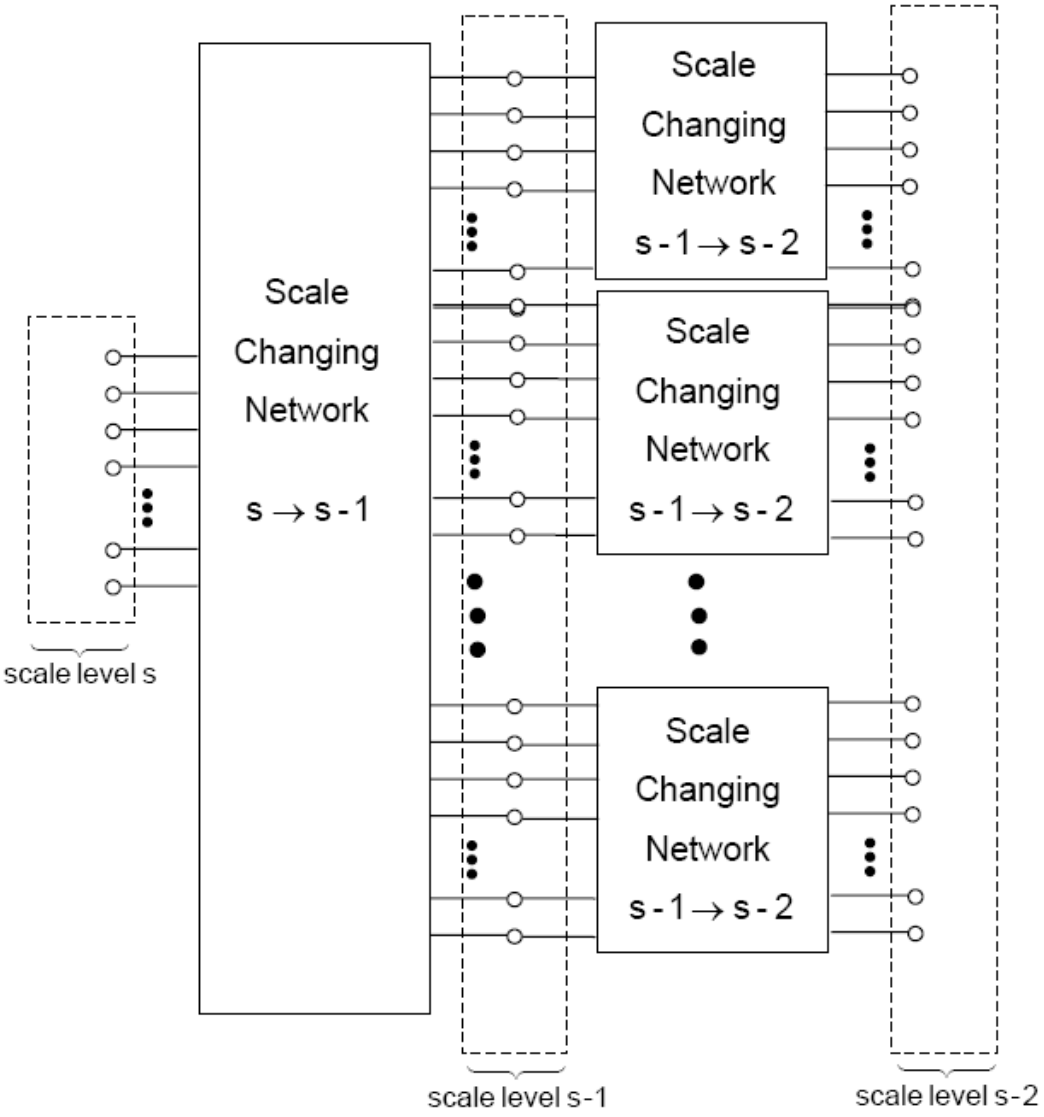

Figure I.4: The cascade of Scale Changing Networks allow to relate the transverse electromagnetic field at scale 's' to that at scale 's–2'

The derivation of scale-changing network's characterization matrix requires the definition of artificial electromagnetic sources named the *scale-changing sources* in various sub-domains obtained from the partitioning process.

I.2.4. Scale-changing Sources

The derivation of scale-changing network that couples the scale $\mathbf{s}$ to the adjacent scale $\mathbf{s-1}$ requires the resolution of a boundary value problem. Active modes of the domain at scale-level $\mathbf{s}$ will act as the excitation sources called *scale changing sources* for the problem.

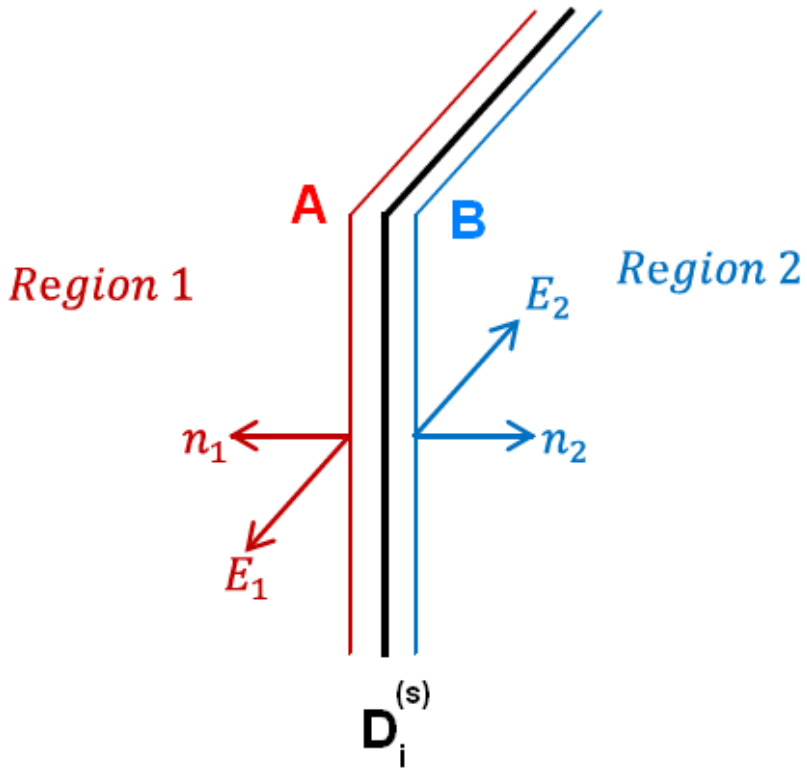

Figure I.5: The discontinuity plane along with the two parallel side-planes A and B in the two half-regions

To derive the mathematical expressions for scale changing sources lets consider once again the generic discontinuity plane $D_i^{(s)}$. Figure I.5 represents the discontinuity plane along with two planes A and B placed infinitely close to the either side of the discontinuity plane. The unit-vectors $\overrightarrow{\mathbf{n_1}}$ and $\overrightarrow{\mathbf{n_2}}$ are the normal vectors of

the two planes. The tangential electric and magnetic fields ($\vec{\boldsymbol{E}}_{\boldsymbol{\alpha}}^{(i,s)}$ and $\vec{\boldsymbol{H}}_{\boldsymbol{\alpha}}^{(i,s)}$) on the domains of the two parallel planes ($\alpha = 1,2$) can be expressed on a modal-basis $\vec{\boldsymbol{F}}_{\boldsymbol{n}}^{(i,s)}$.

$$\vec{\boldsymbol{E}}_{\boldsymbol{\alpha}}^{(i,s)} = \sum_{n=1}^{\infty} V_n^{(i,s,\alpha)} \vec{\boldsymbol{F}}_{\boldsymbol{n}}^{(i,s)} \tag{I.3}$$

$$\vec{\boldsymbol{J}}_{\boldsymbol{\alpha}}^{(i,s)} = \vec{\boldsymbol{H}}_{\boldsymbol{\alpha}}^{(i,s)} \times \overrightarrow{\mathbf{n}_{\boldsymbol{\alpha}}} = \sum_{n=1}^{\infty} I_n^{(i,s,\alpha)} \vec{\boldsymbol{F}}_{\boldsymbol{n}}^{(i,s)} \tag{I.4}$$

$V_n^{(i,s,\alpha)}$and $I_n^{(i,s,\alpha)}$ denote respectively, the voltage and current amplitudes of the *n*th mode in $\mathrm{D}_{\alpha}^{(s)}$. Tangential electric field and the surface current density on each of the domain can be expressed separately with active and passive modes defining the large scale and fine scale variation of these quantities respectively.

$$\begin{cases} \vec{\boldsymbol{E}}_{\boldsymbol{\alpha}}^{(i,s)} = \sum_{n=1}^{N_{\alpha}} V_n^{(i,s,\alpha)} \vec{\boldsymbol{F}}_{\boldsymbol{n}}^{(i,s)} + \sum_{n=N_{\alpha}+1}^{\infty} V_n^{(i,s,\alpha)} \vec{\boldsymbol{F}}_{\boldsymbol{n}}^{(i,s)} \\ \vec{\boldsymbol{E}}_{\boldsymbol{\alpha}}^{(i,s)} = \vec{\boldsymbol{E}}_{\boldsymbol{\alpha}}^{(i,s)}\Big|_{\boldsymbol{large}} + \vec{\boldsymbol{E}}_{\boldsymbol{\alpha}}^{(i,s)}\Big|_{\boldsymbol{fine}} \end{cases} \tag{I.5}$$

where $\boldsymbol{N_{\alpha}}$ is the number of active modes in each of the domain. Similarly for surface current density we can write.

$$\begin{cases} \vec{\boldsymbol{J}}_{\boldsymbol{\alpha}}^{(i,s)} = \sum_{n=1}^{N_{\alpha}} I_n^{(i,s,\alpha)} \vec{\boldsymbol{F}}_{\boldsymbol{n}}^{(i,s)} + \sum_{n=N_{\alpha}+1}^{\infty} I_n^{(i,s,\alpha)} \vec{\boldsymbol{F}}_{\boldsymbol{n}}^{(i,s)} \\ \vec{\boldsymbol{J}}_{\boldsymbol{\alpha}}^{(i,s)} = \vec{\boldsymbol{J}}_{\boldsymbol{\alpha}}^{(i,s)}\Big|_{\boldsymbol{large}} + \vec{\boldsymbol{J}}_{\boldsymbol{\alpha}}^{(i,s)}\Big|_{\boldsymbol{fine}} \end{cases} \tag{I.6}$$

The passive modes being highly evanescent are shunted by their purely reactive modal admittances ($Y_n^{(i,s,\alpha)}$). Consequently,

$$I_n^{(i,s,\alpha)} \approx Y_n^{(i,s,\alpha)} V_n^{(i,s,\alpha)} \qquad \text{for } n > N_{\alpha} \tag{I.7}$$

Using the above formulation in Equation I.6 we obtain;

$$\vec{\boldsymbol{J}}_{\boldsymbol{\alpha}}^{(i,s)} \approx \vec{\boldsymbol{J}}_{\boldsymbol{\alpha}}^{(i,s)}\Big|_{\boldsymbol{large}} + \sum_{n=N_{\alpha}+1}^{\infty} Y_n^{(i,s,\alpha)} V_n^{(i,s,\alpha)} \vec{\boldsymbol{F}}_{\boldsymbol{n}}^{(i,s)} \tag{I.8}$$

which can be formally written in the operator form as:

$$\vec{\boldsymbol{J}}_{\boldsymbol{\alpha}}^{(\boldsymbol{i},\boldsymbol{s})} = \vec{\boldsymbol{J}}_{\boldsymbol{\alpha}}^{(\boldsymbol{i},\boldsymbol{s})}\Big|_{\boldsymbol{large}} + \hat{Y}_{\alpha}^{(i,s)}\vec{\boldsymbol{E}}_{\boldsymbol{\alpha}}^{(\boldsymbol{i},\boldsymbol{s})} \tag{I.9}$$

with $\hat{Y}_{\alpha}^{(i,s)} = \sum_{\boldsymbol{n}=\boldsymbol{N}_{\boldsymbol{\alpha}}+\boldsymbol{1}}^{\infty}\left|\vec{\boldsymbol{F}}_{\boldsymbol{n}}^{(\boldsymbol{i},\boldsymbol{s})}\right\rangle Y_n^{(i,s,\alpha)}\left\langle\vec{\boldsymbol{F}}_{\boldsymbol{n}}^{(\boldsymbol{i},\boldsymbol{s})}\right|$ where $\hat{Y}_{\alpha}^{(i,s)}$ is an admittance operator.

Now the tangential electric field and surface current density on the discontinuity plane $\mathrm{D}_{\mathrm{i}}^{(\mathrm{s})}$can be determined from using the following boundary conditions.

$$\begin{cases}\vec{\boldsymbol{E}}_{\boldsymbol{i}}^{(\boldsymbol{s})} = \vec{\boldsymbol{E}}_{\boldsymbol{A}}^{(\boldsymbol{i},\boldsymbol{s})} = \vec{\boldsymbol{E}}_{\boldsymbol{B}}^{(\boldsymbol{i},\boldsymbol{s})} \\ \vec{\boldsymbol{J}}_{\boldsymbol{i}}^{(\boldsymbol{s})} = \vec{\boldsymbol{J}}_{\boldsymbol{A}}^{(\boldsymbol{i},\boldsymbol{s})} + \vec{\boldsymbol{J}}_{\boldsymbol{B}}^{(\boldsymbol{i},\boldsymbol{s})}\end{cases} \tag{I.10}$$

Using the above equations we can solve for the field quantities on the discontinuity plane as follows:

$$\begin{gathered}\sum_{\boldsymbol{n}=\boldsymbol{1}}^{\infty} V_n^{(i,s)}\,\vec{\boldsymbol{F}}_{\boldsymbol{n}}^{(\boldsymbol{i},\boldsymbol{s})} = \sum_{\boldsymbol{n}=\boldsymbol{1}}^{\infty} V_n^{(i,s,A)}\,\vec{\boldsymbol{F}}_{\boldsymbol{n}}^{(\boldsymbol{i},\boldsymbol{s})} = \sum_{\boldsymbol{n}=\boldsymbol{1}}^{\infty} V_n^{(i,s,B)}\,\vec{\boldsymbol{F}}_{\boldsymbol{n}}^{(\boldsymbol{i},\boldsymbol{s})} \\ \Rightarrow V_n^{(i,s)} = V_n^{(i,s,A)} = V_n^{(i,s,B)}\end{gathered} \tag{I.11}$$

Similarly $\vec{\boldsymbol{J}}_{\boldsymbol{i}}^{(\boldsymbol{s})}$ can be written as

$$\vec{\boldsymbol{J}}_{\boldsymbol{i}}^{(\boldsymbol{s})} = \vec{\boldsymbol{J}}_{\boldsymbol{i}}^{(\boldsymbol{s})}\Big|_{\boldsymbol{large}} + \hat{Y}_{i}^{(s)}\vec{\boldsymbol{E}}_{\boldsymbol{i}}^{(\boldsymbol{s})} \tag{I.12}$$

where

$$\begin{cases}\vec{\boldsymbol{J}}_{\boldsymbol{i}}^{(\boldsymbol{s})}\Big|_{\boldsymbol{large}} = \sum_{\boldsymbol{\alpha}=\boldsymbol{A},\boldsymbol{B}}\vec{\boldsymbol{J}}_{\boldsymbol{\alpha}}^{(\boldsymbol{i},\boldsymbol{s})}\Big|_{\boldsymbol{large}} = \sum_{\boldsymbol{n}=\boldsymbol{1}}^{\boldsymbol{N_A}} I_n^{(i,s,A)}\,\vec{\boldsymbol{F}}_{\boldsymbol{n}}^{(\boldsymbol{i},\boldsymbol{s})} + \sum_{\boldsymbol{n}=\boldsymbol{1}}^{\boldsymbol{N_B}} I_n^{(i,s,B)}\,\vec{\boldsymbol{F}}_{\boldsymbol{n}}^{(\boldsymbol{i},\boldsymbol{s})} \\ \hat{Y}_{i}^{(s)} = \hat{Y}_{A}^{(i,s)} + \hat{Y}_{B}^{(i,s)} = \sum_{\boldsymbol{\alpha}=\boldsymbol{A},\boldsymbol{B}}\sum_{\boldsymbol{n}=\boldsymbol{N}_{\boldsymbol{\alpha}}+\boldsymbol{1}}^{\infty}\left|\vec{\boldsymbol{F}}_{\boldsymbol{n}}^{(\boldsymbol{i},\boldsymbol{s})}\right\rangle Y_n^{(i,s,\alpha)}\left\langle\vec{\boldsymbol{F}}_{\boldsymbol{n}}^{(\boldsymbol{i},\boldsymbol{s})}\right|\end{cases} \tag{I.13}$$

If the same number of active modes are taken in the domains A and B i.e. $N_A = N_B = N_i$, the current scale changing sources at scale-level s and domain $\mathrm{D}_{\mathrm{i}}^{(\mathrm{s})}$can be rewritten in the simplified form as under:

$$\begin{cases}\vec{\boldsymbol{J}}_{\boldsymbol{i}}^{(\boldsymbol{s})}\Big|_{\boldsymbol{large}} = \sum_{\boldsymbol{n}=\boldsymbol{1}}^{\boldsymbol{N}_{\boldsymbol{i}}} I_n^{(i,s)}\,\vec{\boldsymbol{F}}_{\boldsymbol{n}}^{(\boldsymbol{i},\boldsymbol{s})} \\ \hat{Y}_{i}^{(s)} = \sum_{\boldsymbol{n}=\boldsymbol{N}_{\boldsymbol{i}}+\boldsymbol{1}}^{\infty}\left|\vec{\boldsymbol{F}}_{\boldsymbol{n}}^{(\boldsymbol{i},\boldsymbol{s})}\right\rangle Y_n^{(i,s)}\left\langle\vec{\boldsymbol{F}}_{\boldsymbol{n}}^{(\boldsymbol{i},\boldsymbol{s})}\right|\end{cases} \tag{I.14}$$

where $I_n^{(i,s)} = I_n^{(i,s,A)} + I_n^{(i,s,B)}$ is the amplitude of the nth active mode in $\mathrm{D}_\mathrm{i}^{(\mathrm{s})}$ and $Y_n^{(i,s)} = Y_n^{(i,s,A)} + Y_n^{(i,s,B)}$ is the total modal admittance viewed by $\mathrm{D}_\mathrm{i}^{(\mathrm{s})}$ in case of passive modes. Equation I.12 can be represented as a Norton equivalent Network shown in Figure I.6.

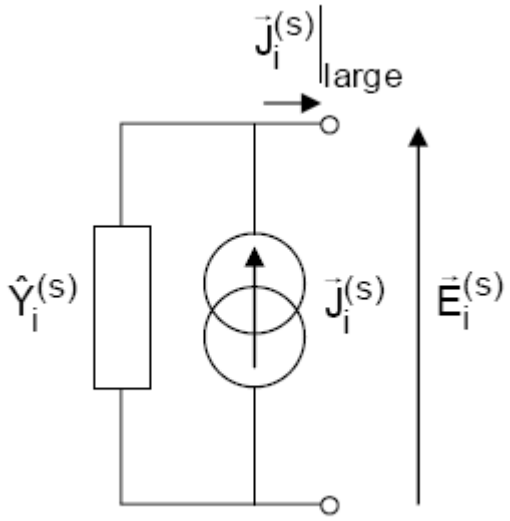

Figure I.6: Symbolic representation of current scale-changing source at scale level 's' in the domain $\mathbf{D}_\mathbf{i}^{(\mathbf{s})}$

In the computation of a scale changing network between a domain $\mathrm{D}_\mathrm{i}^{(\mathrm{s})}$at scale ***s*** and the sub-domains $\mathrm{D}_\mathrm{j}^{(\mathrm{s}-1)}$at scale ***s-1***, the scale-changing sources of the sub-domains are defined on the active modes of the respective sub-domain only. This is due to the assumption that we made in the earlier section that active modes of the larger domain interacts very weakly to the passive modes of its constituent sub-domains.

I.3. MODELING OF A PASSIVE PLANAR REFLECTOR CELL USING SCALE-CHANGING TECHNIQUE (SCT)

I.3.1. Introduction

In the previous sections we have developed the basic concepts needed to understand the scale changing technique. Now we will apply these concepts to a practical case of passive planar reflector cell.

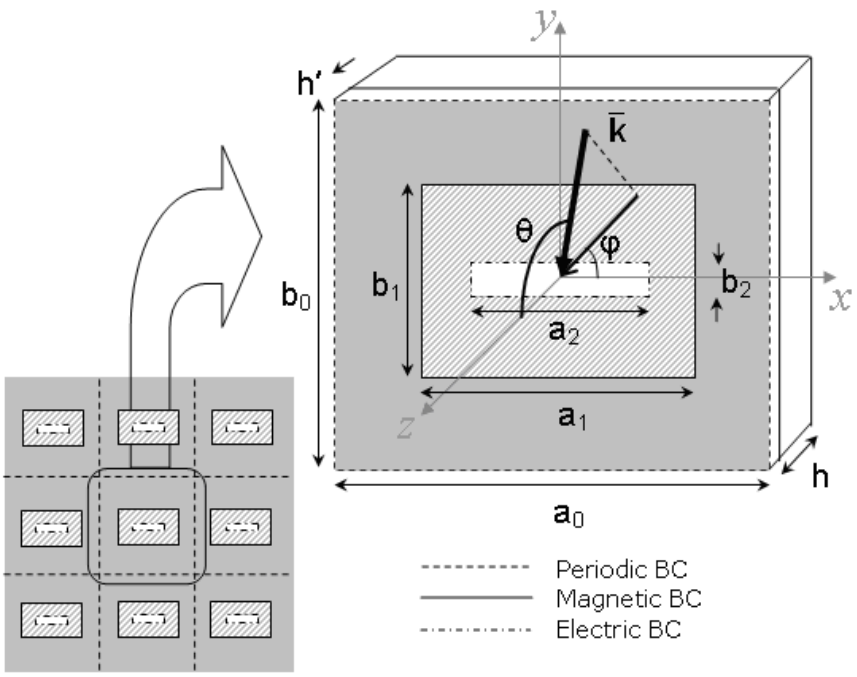

Figure I.7: A 2-D infinite reflect-array with enlarged unit-cell: Dimensions: a_0=b_0=15mm, a_1=12mm, b_2=1mm, b_1 and a_2 are variable. Substrate thickness h'=0.1mm (ε_r=3.38), air gap height h=4mm.

I.3.2. Geometry of the Problem

Consider an infinite array of Figure I.7 under plane wave excitation. This problem is equivalent to resolving the same problem for a single unit-cell under periodic boundary conditions. The computation of phase-shift introduced to an incident plane-wave by unit-cell reflectors when bounded by periodic boundary conditions is an essential step of a reflectarray design process. Characterization of each unit-cell under infinite array environment is considered as an approximation of

the behavior of that cell in the real array. Therefore we will consider here the problem of finding the scattering matrix of a planar reflector under infinite array conditions.

I.3.3. Application of Scale-changing Technique

I.3.3.1. Partitioning of Discontinuity Plane:

Application of scale-changing technique requires the partitioning of the discontinuity plane. In our case simplicity of the geometry allows us to define three nested scales (Figure I.8). In this simple case we have only one domain at each scale-level. Domain $D_1^{(3)}$ of scale-level 3 encompasses the entire reflector plane. Domain $D_1^{(2)}$ at second scale-level consists of patch and slot whereas the domain $D_1^{(1)}$ on the bottom scale is comprised of slot only.

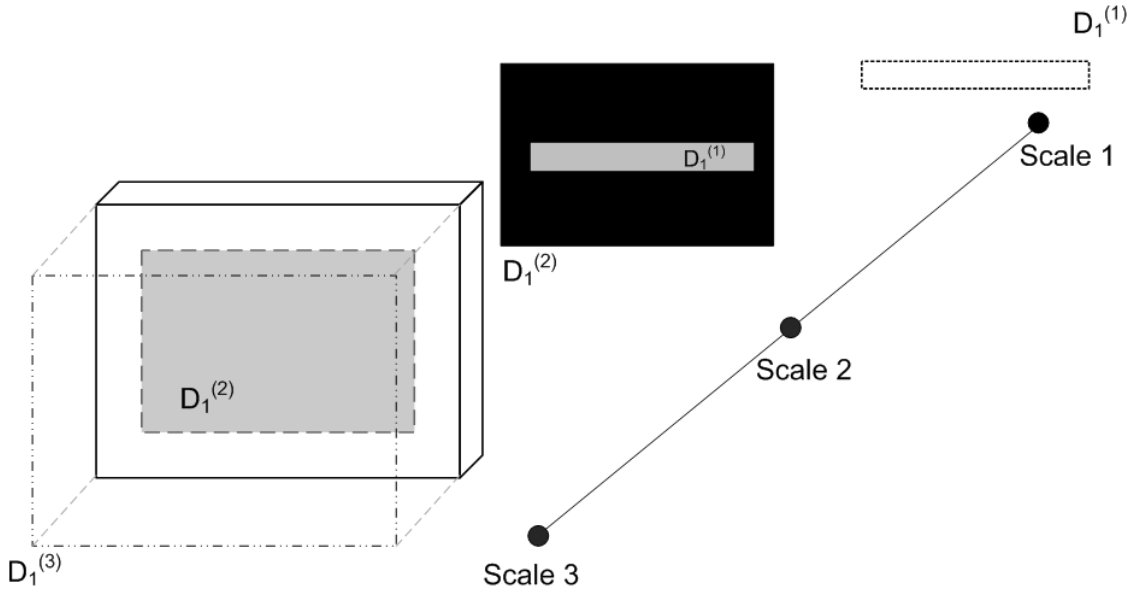

Figure I.8: Partitioning the discontinuity plane of the planar reflector in its constituent domains and sub-domains at three scales. White portions represent dielectric, Black represents metal and grey parts represent un-partitioned sub-domains.

This problem requires the computation of one scale-changing network i.e. between the scale-level 3 and scale-level 2 modeling the interaction between the

active modes of $D_1^{(3)}$ and $D_1^{(2)}$. This SCN will be cascaded with a surface impedance multipole computed on the active modes of $D_1^{(2)}$ as shown in Figure I.9.

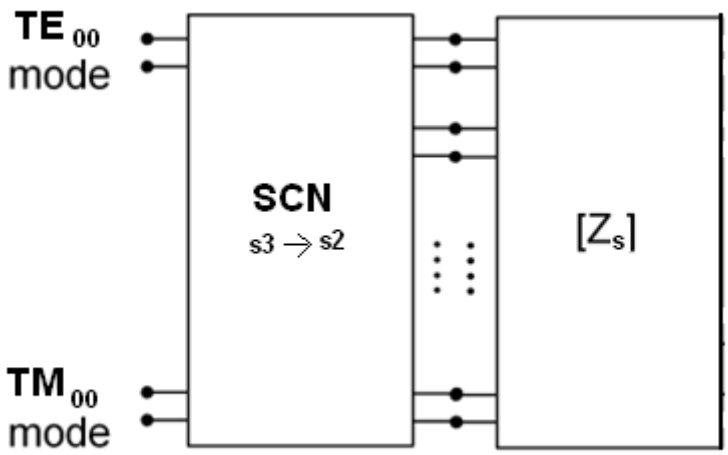

Figure I.9: Global simulation of the planar reflector involves the cascade of the scale-changing network multipole and the surface impedance multipole.

The two multipoles can be computed separately by decomposing the original problem in two separate problems each modeling two successive scale-levels as shown in the Figure I.10. The resolution of the structure in Figure I.10 (a) will give the scale changing network multipole while the surface impedance multipole can be obtained from the structure of Figure I.10 (b).

I.3.3.2. Surface Impedance Multipole Computation:

The surface impedance multipole is represented in Figure I.10 (b). The ports on the LHS represent the active modes in domain $D_1^{(2)}$ of scale-level 2. The boundary value problem in this case is shown in the same figure above the surface impedance multipole. Here we have the slot domain $D_1^{(1)}$ nested inside the patch domain $D_1^{(2)}$, both resting on a dielectric slab of relative permittivity $\boldsymbol{\varepsilon_r}$. This boundary value problem can be represented in terms of the equivalent circuit of Figure I.11.

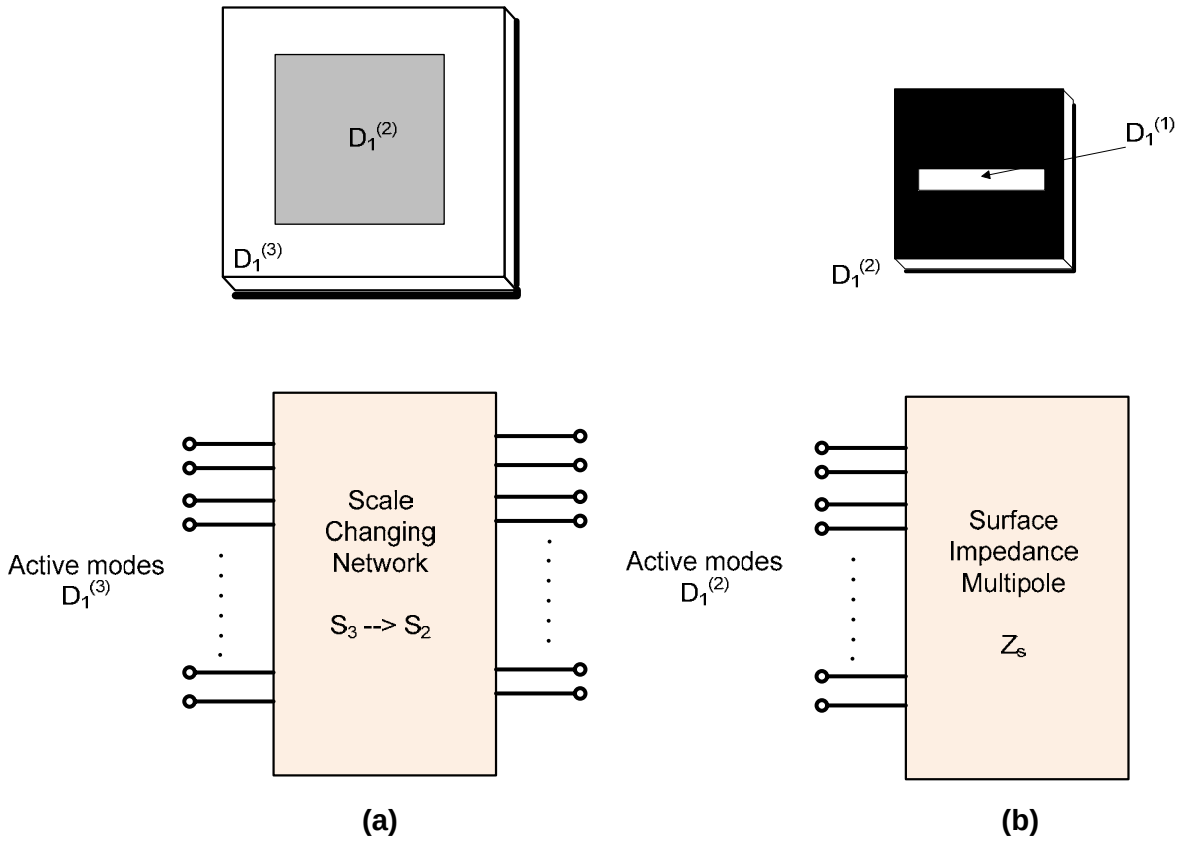

Figure I.10: Decomposition of the problem in two sub-problems. (a) SCN is computed from the structure shown above the SCN multipole (b) Surface Impedance Multipole is computed from the problem involving patch and slot domain only.

The left part of the circuit i.e. the source $J_1^{(2)}$ along with the admittance operator $\hat{Y}_M$ is the Norton equivalent excitation defined on the discrete orthogonal modal-basis of $D_1^{(2)}$ ($\vec{F}_n^{(1,2)}$).

$$\begin{cases} \vec{J}_1^{(2)} = \vec{H}_1^{(2)} \times \vec{n} = \sum_{n=1}^{N^{(1,2)}} I_n^{(1,2)} \vec{F}_n^{(1,2)} \\ \vec{E}_1^{(2)} = \sum_{n=1}^{\infty} V_n^{(1,2)} \vec{F}_n^{(1,2)} \end{cases} \quad \textbf{(I.15)}$$

$$\hat{Y}_M = \sum_{n=N^{(1,2)}+1}^{\infty} \left| \vec{F}_n^{(1,2)} \right\rangle Y_n^{(1,2)} \left\langle \vec{F}_n^{(1,2)} \right| \quad \textbf{(I.16)}$$

$N^{(1,2)}$ is the number of active modes of the domain $D_1^{(2)}$. $I^{(1,2)}$ and $V^{(1,2)}$ are the column vectors of size $N^{(1,2)}$ listing the coefficients in the matrix form.

$$I^{(1,2)} = \begin{bmatrix} I_1^{(1,2)} \\ \vdots \\ I_{N^{(1,2)}}^{(1,2)} \end{bmatrix} \qquad V^{(1,2)} = \begin{bmatrix} V_1^{(1,2)} \\ \vdots \\ V_{N^{(1,2)}}^{(1,2)} \end{bmatrix} \tag{I.17}$$

$Y_n^{(1,2)}$ is the admittance of nth mode. The expressions for the modal admittances for TE and TM modes are as follows:

$$Y_n^{(i)} = \begin{cases} \frac{\gamma_n^{(i)}}{j\omega\mu_0} & TE\ modes \\ \frac{j\omega\varepsilon}{\gamma_n^{(i)}} & TM\ modes \end{cases} \tag{I.18}$$

with $\gamma_n^{(i)}$ the propagation constant of nth mode in medium i. The expression of $\gamma^{(i)}$ for a TE or TM mode is $\gamma^{(i)} = \sqrt{k_c^2 - k_0^2 \varepsilon_r^{(i)}}$

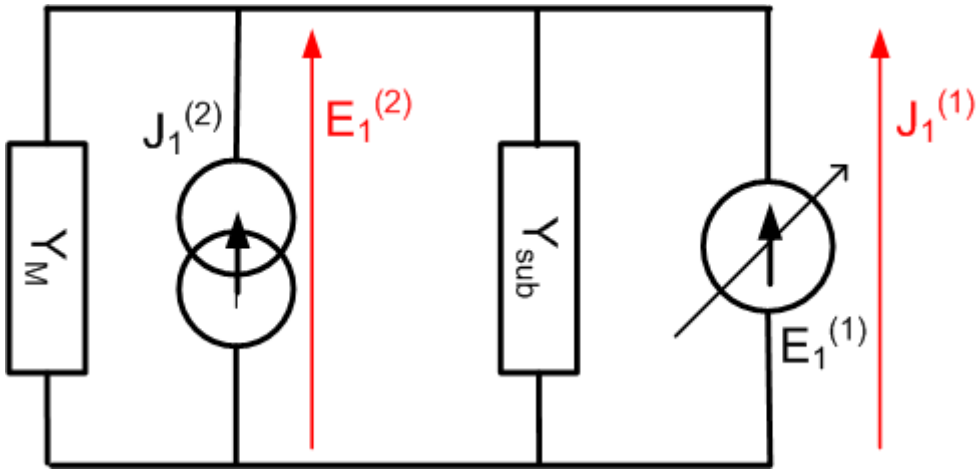

Figure I.11: Equivalent circuit diagram to compute the surface impedance multipole.

The dielectric side of the discontinuity plane is modeled as a shorted dielectric waveguide. Therefore the operator $\hat{Y}_{sub}$ represents the modes of the domain $D_1^{(2)}$ short circuited by ground through the dielectric. If h is the thickness of the dielectric and γ_{nsub} the propagation constant of nth mode in the substrate then the admittance operator can be written as

$$\hat{Y}_{sub} = \sum_{n=1}^{\infty} \left| \vec{F}_n^{(1,2)} \right\rangle Y_{nsub}^{(1,2)} \coth(\gamma_{nsub} h) \left\langle \vec{F}_n^{(1,2)} \right| \tag{I.19}$$

The electric field source $\mathrm{E}_1^{(1)}$ is a virtual source defined in the slot domain $\mathrm{D}_1^{(1)}$ (scale 1). The name *virtual sources* imply that unlike real sources they deliver no electromagnetic energy and are therefore represented with an arrow across the source. The virtual sources serve to represent two different boundary conditions at a time in one equivalent circuit. For example in this case the field source $\mathrm{E}_1^{(1)}$ defined in $\mathrm{D}_1^{(1)}$ models dielectric boundary conditions where as the dual quantity $\mathrm{J}_1^{(1)}$ which is only defined outside $\mathrm{D}_1^{(1)}$ models the perfect electric boundary conditions of the metallic surface.

It is to be noted here that both the quantities $\mathrm{E}_1^{(1)}$ and $\mathrm{J}_1^{(1)}$ cannot be non-zero at the same time and therefore the energy supplied by the source which is the product of the two quantities $\mathbf{E}$ and $\mathbf{J}$ is zero everywhere [Aubert03]. $\mathrm{E}_1^{(1)}$ serves to represent the tangential electric field in the slot domain on an orthogonal set of entire domain trial functions [Nadarassin95] defined in $\mathrm{D}_1^{(1)}$ ($\vec{\boldsymbol{F}}_{\boldsymbol{n}}^{(1,1)}$) as under.

$$\begin{cases} \vec{\boldsymbol{E}}_1^{(1)} = \sum_{\boldsymbol{n=1}}^{\boldsymbol{N^{(1,1)}}} V_n^{(1,1)} \vec{\boldsymbol{F}}_{\boldsymbol{n}}^{(1,1)} \\ \vec{\boldsymbol{J}}_1^{(1)} = \vec{\mathbf{0}} \end{cases} \quad \boldsymbol{in}\ \mathrm{D}_1^{(1)} \qquad \textbf{(I.20)}$$

$N^{(1,1)}$ being the number of active modes in $\mathrm{D}_1^{(1)}$. The column-vector $V^{(1,1)}$ of dimensions $N^{(1,1)}$ lists the weights of the test functions.

$$V^{(1,1)} = \begin{bmatrix} V_1^{(1,1)} \\ \vdots \\ V_{N^{(1,1)}}^{(1,1)} \end{bmatrix} \qquad \textbf{(I.21)}$$

Following matrix equations can be written from the equivalent circuit by using Kirchoff's laws.

$$\begin{bmatrix} \mathrm{E}_1^{(2)} \\ \mathrm{J}_1^{(1)} \end{bmatrix} = \begin{bmatrix} 0 & 1 \\ -1 & \hat{Y}_M + \hat{Y}_{sub} \end{bmatrix} \times \begin{bmatrix} \mathrm{J}_1^{(2)} \\ \mathrm{E}_1^{(1)} \end{bmatrix} \qquad \textbf{(I.22)}$$

This boundary value problem may be solved by applying the Galerkin's method. The above matrix equation can therefore be written in terms of coefficient matrices.

$$\begin{bmatrix} V^{(1,2)} \\ 0 \end{bmatrix} = \begin{bmatrix} 0 & P_1 \\ -P_1^T & P_1^T Y_{sub} P_1 + P_2^T (Y_M + Y_{sub}) P_2 \end{bmatrix} \times \begin{bmatrix} I^{(1,2)} \\ V^{(1,1)} \end{bmatrix} \quad \textbf{(I.23)}$$

T denotes the complex conjugate transpose of a matrix. $[P_1]$ is the projection matrix of dimensions $N^{(1,2)} \times N^{(1,1)}$ of active modes of modal-basis $\vec{\boldsymbol{F}}_{\boldsymbol{n}}^{(1,2)}$on $\vec{\boldsymbol{F}}_{\boldsymbol{n}}^{(1,1)}$.

$$[P_1] = \begin{bmatrix} \langle F_1^{(1,2)}, F_1^{(1,1)} \rangle & \cdots & \langle F_1^{(1,2)}, F_{N^{(1,1)}}^{(1,1)} \rangle \\ \vdots & \ddots & \vdots \\ \langle F_{N^{(1,2)}}^{(1,2)}, F_1^{(1,1)} \rangle & \cdots & \langle F_{N^{(1,2)}}^{(1,2)}, F_{N^{(1,1)}}^{(1,1)} \rangle \end{bmatrix} \quad \textbf{(I.24)}$$

Similarly $[P_2]$ is the projection matrix of dimensions $\left(M^{(1,2)} - N^{(1,2)}\right) \times N^{(1,1)}$ of passive modes of modal-basis $\vec{\boldsymbol{F}}_{\boldsymbol{n}}^{(1,2)}$on $\vec{\boldsymbol{F}}_{\boldsymbol{n}}^{(1,1)}$.

$$[P_2] = \begin{bmatrix} \langle F_{N^{(1,2)}+1}^{(1,2)}, F_1^{(1,1)} \rangle & \cdots & \langle F_{N^{(1,2)}+1}^{(1,2)}, F_{N^{(1,1)}}^{(1,1)} \rangle \\ \vdots & \ddots & \vdots \\ \langle F_{M^{(1,2)}}^{(1,2)}, F_1^{(1,1)} \rangle & \cdots & \langle F_{M^{(1,2)}}^{(1,2)}, F_{N^{(1,1)}}^{(1,1)} \rangle \end{bmatrix} \quad \textbf{(I.25)}$$

$[Y_M]$ is a diagonal matrix of passive modal admittances. Its dimensions are $\left(M^{(1,2)} - N^{(1,2)}\right) \times \left(M^{(1,2)} - N^{(1,2)}\right)$

$$[Y_M] = \begin{bmatrix} Y_{N^{(1,2)}+1}^{(1,2)} & \cdots & 0 \\ \vdots & \ddots & \vdots \\ 0 & \cdots & Y_{M^{(1,2)}}^{(1,2)} \end{bmatrix} \quad \textbf{(I.26)}$$

$[Y_M]$ is a diagonal matrix of dimensions $M^{(1,2)} \times M^{(1,2)}$

$$[Y_{sub}] = \begin{bmatrix} Y_{1sub}^{(1,2)} \coth(\gamma_{1sub} h) & \cdots & 0 \\ \vdots & \ddots & \vdots \\ 0 & \cdots & Y_{M^{(1,2)}sub}^{(1,2)} \coth(\gamma_{Msub} h) \end{bmatrix} \quad \textbf{(I.27)}$$

From equation (**I.23**) surface impedance can be written as

$$[Zs^{(1,2)}] = P_1 \times (P_1^T Y_{sub} P_1 + P_2^T (Y_M + Y_{sub}) P_2)^{-1} \times P_1^T \quad \textbf{(I.28)}$$

with

$$[V^{(1,2)}] = [Zs^{(1,2)}] \times [I^{(1,2)}] \quad \textbf{(I.29)}$$

I.3.3.3. Scale-changing Network Computation:

Equivalent circuit of Figure I.12 (a) represents the boundary value problem of Fig I.10 (a). In this case the discontinuity plane represented by the middle branch is modeled with two sources. The current source $j_e^{(2)}$ is the virtual source defined in $D_1^{(2)}$ defining perfect electric boundary conditions while the electric field source $e^{(2)}$ is the scale-changing source modeling the electromagnetic coupling with the sub-domain as explained in section I. Assuming that both sources are defined by the same set of orthogonal modes the equivalent circuit can be simplified to that of Figure I.12 (b) [PerretTh].

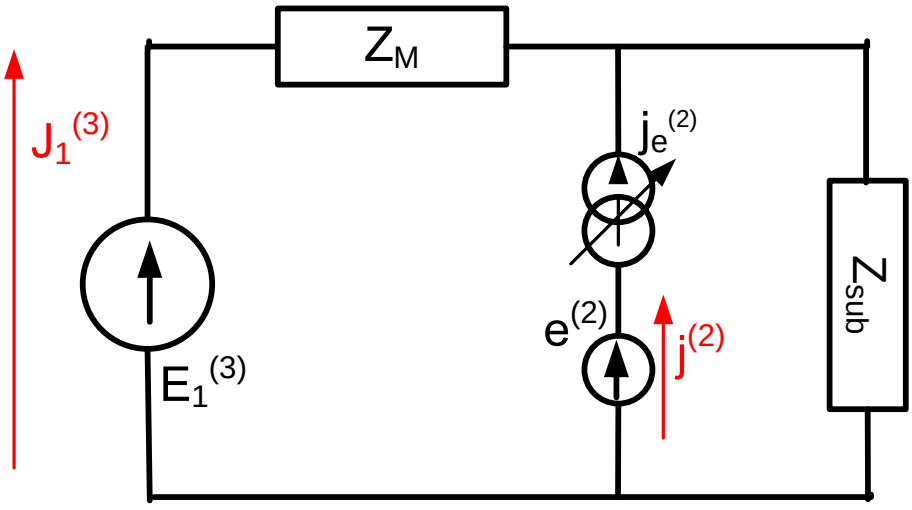

(a)

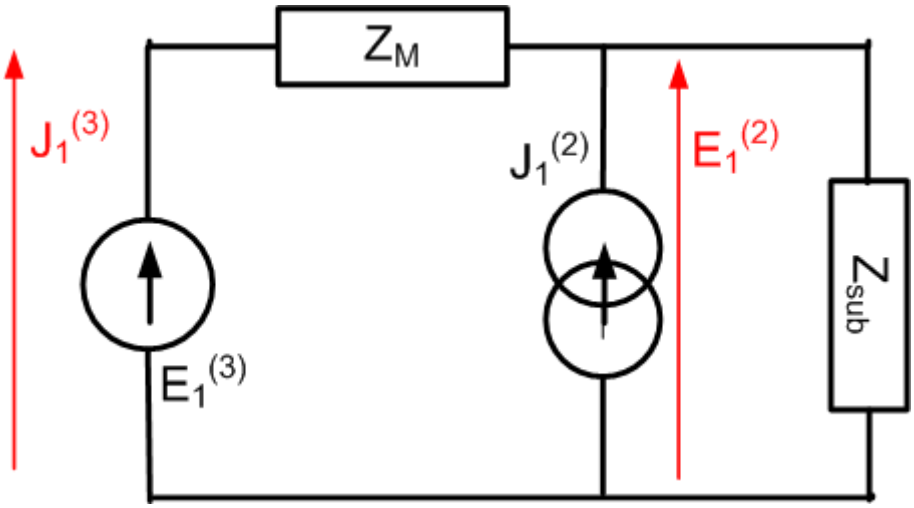

(b)

Figure I.12: (a) Equivalent circuit diagram to compute the scale-changing network multipole. (b) Simplified Equivalent Circuit.

$\vec{E}_1^{(3)}$ is the excitation source defined on $N^{(1,3)}$ active modes of the orthogonal modal-basis of $\mathrm{D}_1^{(3)}$ ($\vec{F}_n^{(1,3)}$). Floquet modal basis is chosen at this scale to model the periodicity of the infinite array. Floquet modes TE_{00} and TM_{00} are chosen to represent the two plane-wave polarizations. The expressions for the Floquet modal basis can be found in Appendix A.

$$\begin{cases} \vec{E}_1^{(3)} = \sum_{n=1}^{N^{(1,3)}} V_n^{(1,3)} \vec{F}_n^{(1,3)} \\ \vec{J}_1^{(3)} = \sum_{n=1}^{\infty} I_n^{(1,3)} \vec{F}_n^{(1,3)} \end{cases} \quad \textbf{(I.30)}$$

$V^{(1,3)}$ and $I^{(1,3)}$ are the column vectors of dimensions $N^{(1,3)}$.

$$I^{(1,3)} = \begin{bmatrix} I_1^{(1,3)} \\ \vdots \\ I_{N^{(1,3)}}^{(1,3)} \end{bmatrix} \qquad V^{(1,3)} = \begin{bmatrix} V_1^{(1,3)} \\ \vdots \\ V_{N^{(1,3)}}^{(1,3)} \end{bmatrix} \quad \textbf{(I.31)}$$

Operators $\hat{Z}_M$ and $\hat{Z}_{sub}$ are defined as usual

$$\begin{cases} \hat{Z}_M = \sum_{n=N^{(1,3)}+1}^{\infty} \left| \vec{F}_n^{(1,3)} \right\rangle Z_n^{(1,3)} \left\langle \vec{F}_n^{(1,3)} \right| \\ \hat{Z}_{sub} = \sum_{n=1}^{\infty} \left| \vec{F}_n^{(1,3)} \right\rangle Z_{nsub}^{(1,3)} \tanh\left(\gamma_{nsub} h\right) \left\langle \vec{F}_n^{(1,3)} \right| \end{cases} \quad \textbf{(I.32)}$$

with modal impedances defined as

$$Z_n^{(i)} = \begin{cases} \frac{j\omega\mu_0}{\gamma_n^{(i)}} & TE\ modes \\ \frac{\gamma_n^{(i)}}{j\omega\varepsilon} & TM\ modes \end{cases} \quad \textbf{(I.33)}$$

Using Kirchoff's circuit laws following matrix equation can be written from the equivalent circuit of Fig (b)

$$\begin{bmatrix} \mathrm{J}_1^{(3)} \\ \mathrm{E}_1^{(2)} \end{bmatrix} = \begin{bmatrix} \left(\hat{Z}_M + \hat{Z}_{sub}\right)^{-1} & -\hat{Z}_{sub}\left(\hat{Z}_M + \hat{Z}_{sub}\right)^{-1} \\ \hat{Z}_{sub}\left(\hat{Z}_M + \hat{Z}_{sub}\right)^{-1} & \hat{Z}_M\hat{Z}_{sub}\left(\hat{Z}_M + \hat{Z}_{sub}\right)^{-1} \end{bmatrix} \times \begin{bmatrix} \mathrm{E}_1^{(3)} \\ \mathrm{J}_1^{(2)} \end{bmatrix} \quad \textbf{(I.34)}$$

Applying Galerkin's method we get

$$\begin{bmatrix} I^{(1,3)} \\ V^{(1,2)} \end{bmatrix} = \begin{bmatrix} H11 & H12 \\ H21 & H22 \end{bmatrix} \times \begin{bmatrix} V^{(1,3)} \\ I^{(1,2)} \end{bmatrix} \quad \textbf{(I.35)}$$

With projection matrices defined as under:

$[H_{11}]$ is a diagonal matrix of dimensions $N^{(1,3)} \times N^{(1,3)}$

$$[H_{11}] = \begin{bmatrix} \left(Z_{1sub}^{(1,3)} \tanh\left(\gamma_{1sub} h\right)\right)^{-1} & \cdots & 0 \\ \vdots & \ddots & \vdots \\ 0 & \cdots & \left(Z_{N^{(1,3)}sub}^{(1,3)} \tanh\left(\gamma_{N^{(1,3)}sub} h\right)\right)^{-1} \end{bmatrix} \quad \textbf{(I.36)}$$

$[H_{12}]$ is a unitary matrix of dimensions $N^{(1,3)} \times N^{(1,2)}$

$$[H_{12}] = \begin{bmatrix} -1 & \cdots & 0 \\ \vdots & \ddots & \vdots \\ 0 & \cdots & -1 \end{bmatrix} \quad \textbf{(I.37)}$$

with $[H_{21}] = -[H_{12}]^T$ and $[H_{22}] = P_2^T Z P_2$

$[P_2]$ is the projection matrix of dimensions $\left(M^{(1,3)} - N^{(1,3)}\right) \times N^{(1,2)}$ of passive modes of modal-basis $\vec{F}_n^{(1,3)}$ on $\vec{F}_n^{(1,2)}$.

$$[P_2] = \begin{bmatrix} \langle F^{(1,3)}_{N^{(1,3)}+1}, F^{(1,2)}_1 \rangle & \cdots & \langle F^{(1,3)}_{N^{(1,3)}+1}, F^{(1,2)}_{N^{(1,2)}} \rangle \\ \vdots & \ddots & \vdots \\ \langle F^{(1,3)}_{M^{(1,3)}}, F^{(1,2)}_1 \rangle & \cdots & \langle F^{(1,3)}_{M^{(1,3)}}, F^{(1,2)}_{N^{(1,2)}} \rangle \end{bmatrix} \quad \textbf{(I.38)}$$

and Z is a diagonal matrix of size $\left(M^{(1,3)} - N^{(1,3)}\right) \times \left(M^{(1,3)} - N^{(1,3)}\right)$

$$[Z] = \begin{bmatrix} \frac{Z^{(1,3)}_{N^{(1,3)}+1} Z^{(1,3)}_{N^{(1,3)}_{sub+1}} \tanh\left(\gamma_{N^{(1,3)}_{sub+1}} h\right)}{Z^{(1,3)}_{N^{(1,3)}+1} + Z^{(1,3)}_{N^{(1,3)}_{sub+1}} \tanh\left(\gamma_{N^{(1,3)}_{sub+1}} h\right)} & \cdots & 0 \\ \vdots & \ddots & \vdots \\ 0 & \cdots & \frac{Z^{(1,3)}_{M^{(1,3)}} Z^{(1,3)}_{M^{(1,3)}_{sub}} \tanh\left(\gamma_{M^{(1,3)}_{sub}} h\right)}{Z^{(1,3)}_{M^{(1,3)}} + Z^{(1,3)}_{M^{(1,3)}_{sub}} \tanh\left(\gamma_{M^{(1,3)}_{sub}} h\right)} \end{bmatrix} \quad \textbf{(I.39)}$$

I.3.3.4. Network Cascade:

In this step cascade of two networks is performed to obtain the equivalent surface impedance of the complete structure $[Z]$ as viewed by the excitation modes at the surface of the discontinuity plane (see Figure I.9)

$$\begin{bmatrix} I^{(1,3)} \\ V^{(1,2)} \end{bmatrix} = \begin{bmatrix} H11 & H12 \\ H21 & H22 \end{bmatrix} \times \begin{bmatrix} V^{(1,3)} \\ I^{(1,2)} \end{bmatrix} \quad \textbf{(I.40)}$$

Note the negative sign in the surface impedance multipole equation to signify the reversal of the currents in the cascading procedure.

$$\left[V^{(1,2)}\right] = -\left[Zs^{(1,2)}\right] \times \left[I^{(1,2)}\right] \quad \textbf{(I.41)}$$

From the above equations following equation for the overall multipole can be extracted

$$\left[I^{(1,3)}\right] = [Ys] \times \left[V^{(1,3)}\right] \quad \textbf{(I.42)}$$

with

$$[Ys] = [H_{11}] + [H_{12}]\left(\left[Zs^{(1,2)}\right] + [H_{22}]\right)^{-1}[H_{12}]^T \quad \textbf{(I.43)}$$

Scattering parameter matrix is calculated by using

$$[S] = \left(\sqrt{[Z_M]}\right)^{-1}([Z] - [Z_M]) \times ([Z] + [Z_M])^{-1}\sqrt{[Z_M]} \quad \textbf{(I.44)}$$

with $[Z] = [Ys]^{-1}$ and $[Z_M]$ is the modal impedance of excitation modes in air.

I.3.4. Results Discussion

I.3.4.1. Planar Reflector under Normal Incidence:

A planar unit-cell reflector depicted in Figure I.13 has been modeled and simulated using the approach outlined in the previous section. The discontinuity plane of the reflector cell is comprised of slotted patch centered on two dielectric layers. The dimensions are indicated in the figure captions. The simulations have been performed for nine distinct unit-cell geometries obtained by varying metallic patch width (b1) and slot length (a2) (Table-I.1). This infinitely thin metal patch rests on a 100µm lossless dielectric ($\varepsilon_r = 3.38$) which is in turn placed on a 4mm air-cavity with a ground-plane at the bottom. Normal plane wave with electric field linearly polarized perpendicular to slot-length is considered as excitation source. The results presented are for the phase of the reflection coefficient (S_{11}) calculated at the plane of the discontinuity plane.

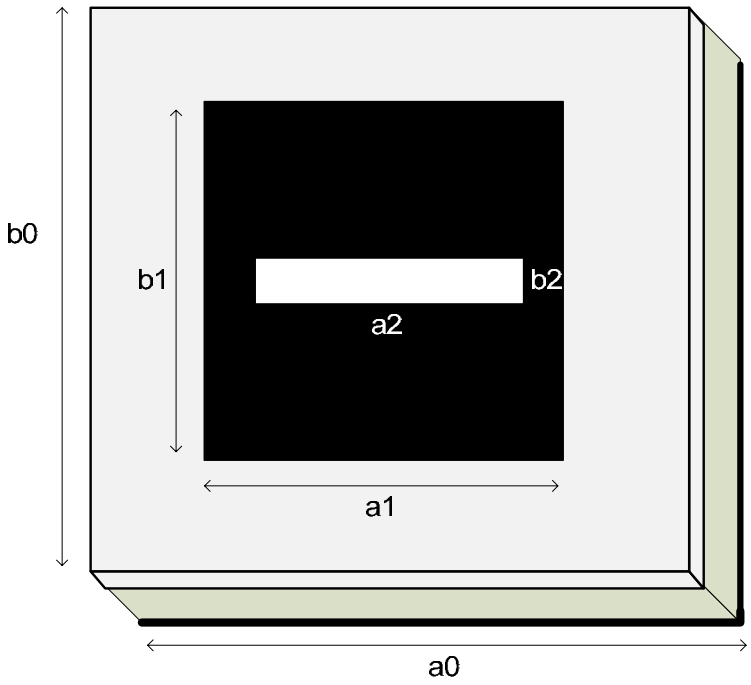

Figure I.13: Geometry of Planar unit-cell reflector. Dimensions: a_0=b_0=15mm, a_1=12mm, b_2=1mm, b_1 and a_2 are variable. Substrate thickness *h1*=0.1mm (ε_r=3.38), air gap height *h2*=4mm.

I.3.4.1.1. Convergence Study:

As described in the previous section, the tangential electromagnetic field in different regions of the discontinuity plane is defined by the orthogonal set of modes of the domain. Precise description of field quantities would require adequate number of active and passive modes to be considered at each scale-level. Appropriate number of modes may be chosen by a systematic convergence study. This study involves plotting reflection coefficient phase results with respect to the number of modes at each domain to find the appropriate number for which the results converge.

Case	1	2	3	4	5	6	7	8	9
b1	2 4 4 6				6	8	10	10 12	
a2	7 4 6 4				10	8	6	10 10	

Table I.1: Above nine planar unit-cell geometric configurations are simulated. Dimension b1 and a2 (in mm) are the width of the patch and the length of the slot respectively.

Convergence study results for the sixth reflector-cell configuration at the centre frequency of 12.1GHz are shown in Figure I.14. Figure I.14 (a) shows the convergence of the reflection coefficient phase with respect to the number of active modes $N^{(1,2)}$ in the patch domain $\mathrm{D}_1^{(2)}$ and the number of passive modes $M^{(1,3)}$ taken inside the periodic waveguide (discontinuity domain $\mathrm{D}_1^{(3)}$. It is apparent that there is no significant variation in phase results for waveguide modes greater than 2500. Similarly around 600 active modes in the patch domain are required for the phase convergence with in 3º margin.

Figure I.14 (b) plots the convergence curves with respect to patch active modes and the number of active modes $N^{(1,1)}$ taken in the slot domain $\mathrm{D}_1^{(1)}$. Here, again the flat part of the curves demonstrates the convergence of reflected phase. It is evident from the curves that convergence is achieved if the number of patch active modes is taken between 600 and 1000 and the number of slot active modes is taken between 80 and 120. However, if the number of slot active modes exceeds a certain limit, matrices become ill-conditioned leading to the loss of convergence as can be seen by the sudden drop in two lower curves. This numerical problem can be

attributed to the use of entire domain trial functions and is analogous to the one observed classically in the Mode Matching Technique [Lee71].

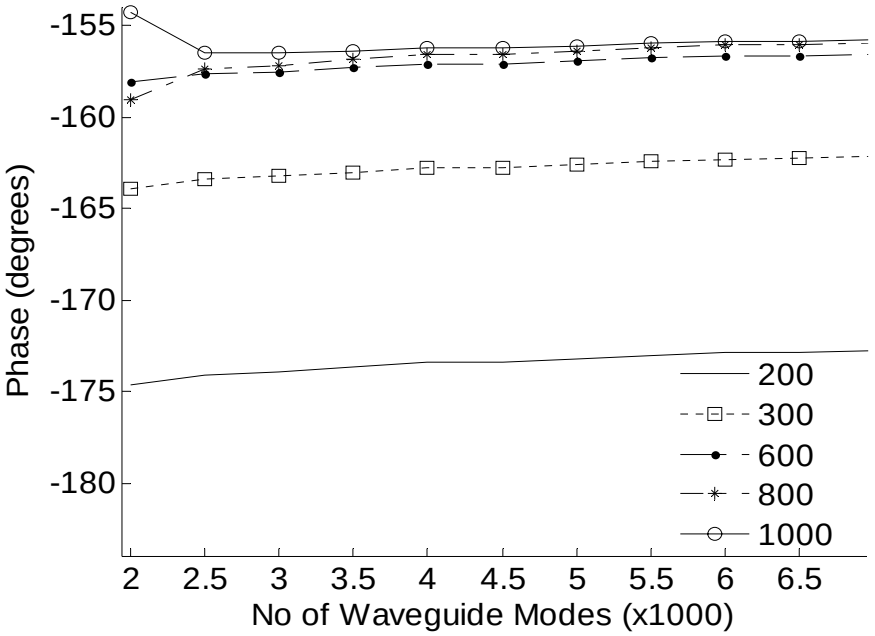

(a)

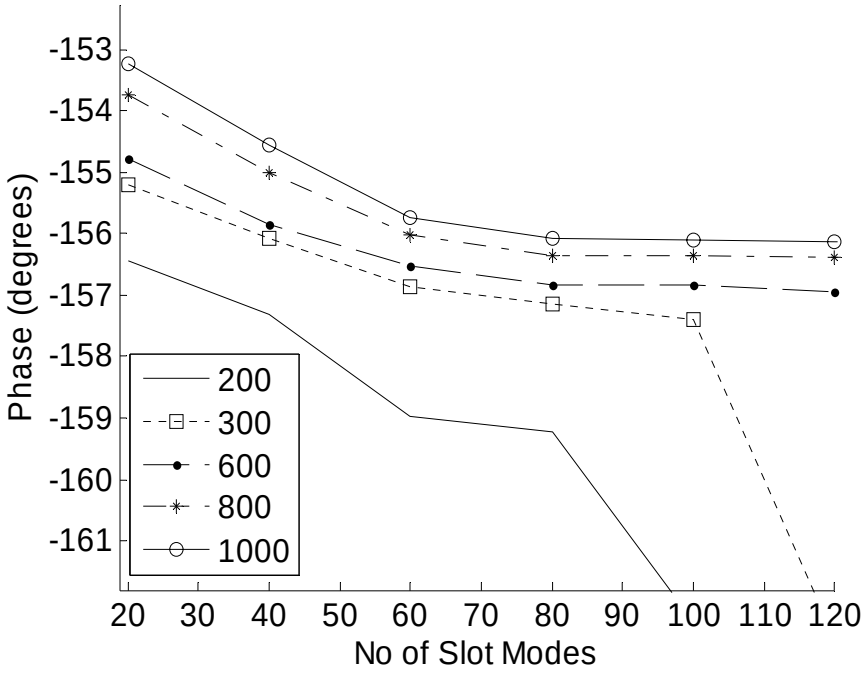

(b)

Figure I.14: Convergence study of phase of reflection coefficient for case6 (b1,a2)=>(8,8), Frequency 12.1GHz : (a) Convergence with respect to number of modes in the waveguide (Legend indicates number of patch modes); (b) Convergence with respect to number of modes in the slot (Legend indicates number of patch modes).

For this reflector-cell configuration we have chosen 5000 waveguide modes, 1000 antenna active modes and 120 slot active modes. For these numbers, the convergence achieved is within 1º margin. It should be noted here that the phase convergence is not very sensitive to number of passive modes in a domain as long as a significant number is taken. 1000 passive modes were taken in the patch domain $M^{(1,2)}$for the simulation results presented in this section. However a rigorous convergence study is required to determine the number of active modes which characterize the mutual coupling between different scales.

I.3.4.1.2. Results for the phase of Reflection Coefficient:

The nine unit-cell configurations are simulated using Scale-changing Technique over the frequency range of 11.7GHz to 12.5GHz using the convergence results at the centre frequency for each configuration. Same structures were simulated using Finite Element Method based commercial software (HFSS *ver*11) under periodic boundary conditions and Floquet port excitation. Table-I.2 lists the values of the reflected phase obtained by SCT and HFSS simulations for all nine configurations at center frequency (12.1GHz) under normal incidence conditions. Difference in the results between the two techniques is listed in the third row. It is evident that the results agree nicely with a maximum difference of 6.1º for the fifth configuration. The overall average difference between two techniques for all the configurations is 3.1º at the center frequency.

Case	1	2	3	4	5	6	7	8	9
SCT	45.86º	26.12º	20.41º	-23.28 º	116.25 º	-156.12º	-144.53º	116.9º	117.2º
HFSS	46.21º	27.94º	20.93º	-21.54 º	122.35 º	-151.49º	-143.01º	123º	122.4º
Diff	0.35º	1.82º	0.52º	1.74 º	6.1 º	4.63º	1.52º	6º	5.24º

Table I.2: A comparison of the S_{11} phase (in degrees) obtained by SCT and HFSS at centre frequency (12.1GHz) for all the nine cases under normal incidence. Third row lists the absolute difference between the two results.

Usually the results over the entire frequency band are required to visualize the phase variation with frequency. In Figure I.15 the phase curves for the first seven

configurations are plotted over the entire frequency band i.e. 11.7 to 12.5 GHz. The results of HFSS simulations are represented on the same figure for comparison purposes. Again the two results agree very closely with maximum difference of 6º for the fifth case. The convergence criterion used in case of HFSS simulations is Δs equal to 2% which means mesh refinement stops when the difference in the S-parameter matrix for two consecutive passes is less than 2%.

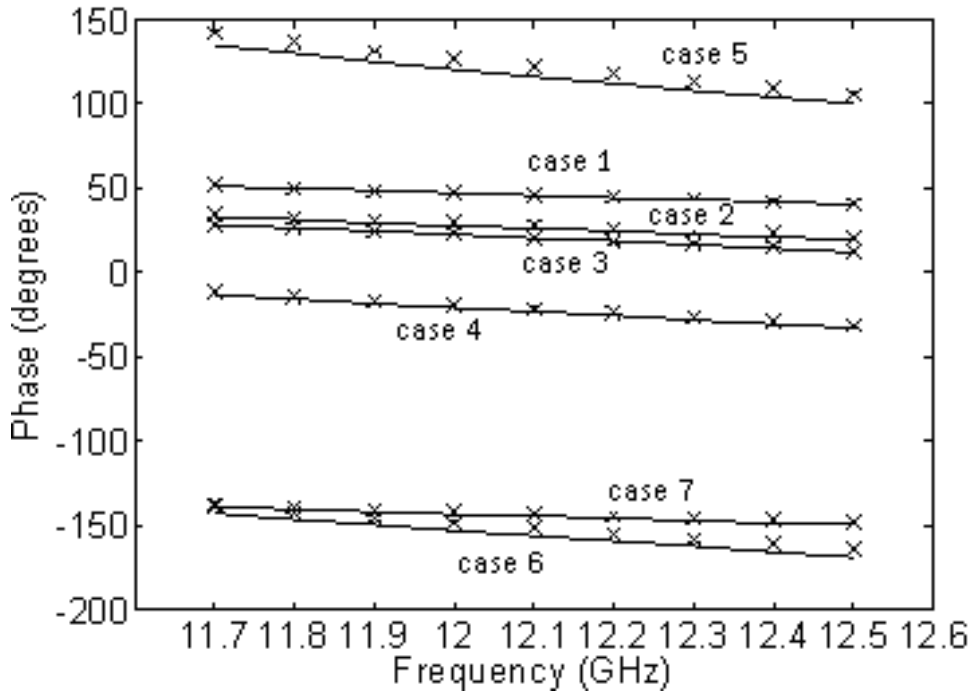

Figure I.15: Phase results over the entire frequency range (11.7 – 12.5GHz) for the first seven geometric cases. (——) SCT (x x x) HFSS.

I.3.4.2. Planar Reflector under Oblique Incidence:

The same nine unit-cell configurations have been studied under oblique incidence excitation. To simply the geometry only a single layer of dielectric is considered shorted by a ground plane. Therefore the results presented in this section are for the configurations in which only the air-cavity acts as the dielectric. All other dimensions remain unchanged.

Plane-wave incidence is defined by the angle θ and φ as shown in the Figure-I.7. The horizontal and vertical polarizations of the plane-wave are characterized by TE_{00} and TM_{00} Floquet propagation modes.

θ	0°		10°		20°		30°		40°		DIFF
	HFSS	**SCT**	**HFSS**	**SCT**	**HFSS**	**SCT**	**HFSS**	**SCT**	**HFSS**	**SCT**	
1	46	47.2	47.1	49	54.7	55	65	67.1	78.5	78.5	**1.02**
2	24.3	29.7	28.9	31	36.8	38	48.4	50	64.2	65	**2.02**
3	20.7	24.6	23.5	26	32.4	34	45	46	61.7	62	**1.95**
4	-21.7	-17	-19.1	-15	-11.1	-8	0.71	4	13.7	17.53	**3.62**
5	123	122.9	122	107	119	104	114	102	109	101	**8.92**
6	-148	-151.5	-151	-153	-155	-158	-166	-169.2	-195	-198	**2.92**
7	-144	-143.8	-146	-143.7	-152	-151	-169	-166.5	-214	-208	**2.8**
8	125	117	118	114.5	111	108.6	101	102.6	89	92.5	**4.8**
9	124	116.5	116	111.5	99.6	102	77.6	96	37.4	56	**9.91**
DIFF	**3.44**		**4.31**		**3.21**		**5.44**		**4.77**		

Table I.3: A comparison of the S_{11} phase (corresponding to the reflection co-efficient of Mode TE_{00}) at the centre frequency 12.5GHz under incidence oblique (φ=0°)

θ	0°		10°		20°		30°		40°		DIFF
	HFSS	**SCT**	**HFSS**	**SCT**	**HFSS**	**SCT**	**HFSS**	**SCT**	**HFSS**	**SCT**	
1	149	147.8	150	149	149	148	144	146.4	135	143	**2.42**
2	172	173.5	172	173	171	171	167	167.5	153	156	**1.20**
3	171	173.9	172	173	171	172	166	168	153	156	**1.82**
4	-173	-171.5	-173	-172	-174	-173.3	-179	-178.4	-195	-194	**1.19**
5	-174	-170.6	-174	-171	-176	-172.5	-179	-177	-196	-193	**2.60**
6	-163	-160.8	-162	-160.8	-164	-162.1	-169	-167.4	-185	-184	**1.80**
7	-157	-152.4	-156	-153.1	-157	-154.6	-161	-161.3	-178	-176	**2.70**
8	-155	-152.3	-155	-151	-156	-153	-161	-158	-178	-173.7	**3.12**
9	-152	-148.7	-151	-150	-152	-154	-157	-163	-173	-173.6	**2.42**
DIFF	**1.55**		**1.34**		**1.88**		**1.99**		**2.89**		

Table I.4: A comparison of the S_{22} phase (corresponding to the reflection co-efficient of Mode TM_{00}) at the centre frequency 12.5GHz under incidence oblique (φ=0°)

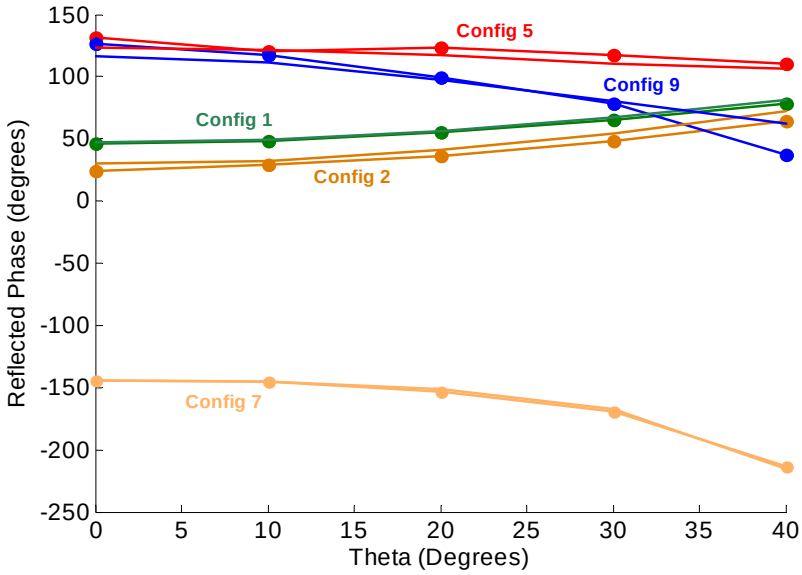

(a)

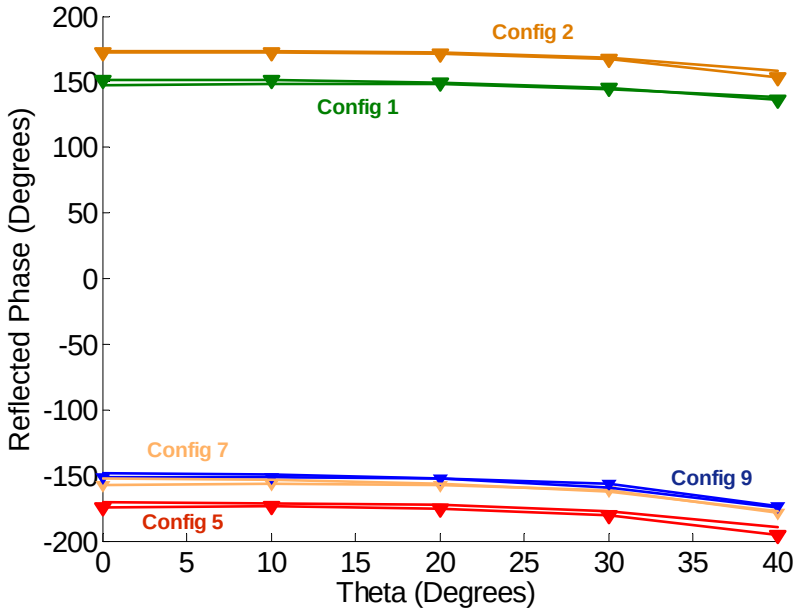

(b)

Figure I.16: Phase results over the entire frequency band. Simple lines represent SCT results. Lines with markers represent HFSS results (a) TE_{00} (b) TM_{00}

Table I.3 lists the reflection phase results of TE_{00} mode for several different angles of incidence. In this case we have varied the angle theta from 0º to 40º in φ=0º plane. The results are compared to those found with HFSS simulations. The last column of the table gives the average difference between the SCT and HFSS results for that particular configuration whereas the last row gives the average difference for all the configurations at a particular incidence. We find a good agreement between the results of two techniques i.e. within ±3º range except for

configuration 5 and 9. The slightly larger difference in results for these two cases can be attributed to the convergence issues of their HFSS simulations.

Table I.4 lists the phase results of the reflection coefficient corresponding to the vertical polarization i.e. TM_{00} for the same incidence angles. Here again the results compare nicely to the results obtained by HFSS. It is important to note that at 12.5GHz and for the incidences given we have only two Floquet propagation modes i.e. TE_{00} and TM_{00}. The incidences are chosen to avoid the appearance of spurious modes.

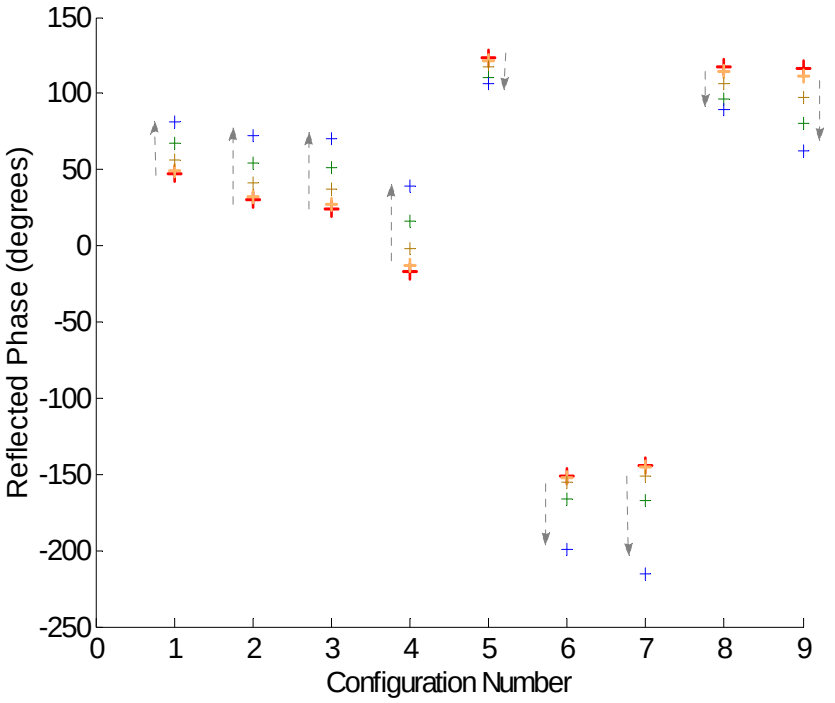

Figure I.17: Variation of S_{11} phase with respect to the angle of incidence (θ from 0º to 40º)

Figure-I.16(a) and Figure-I.16(b) plot the phase results for the two polarizations over the entire frequency band. Only the results of a limited number of configurations are depicted to avoid over-crowding of the figures. Simple lines represent the SCT results while the lines containing markers plot the HFSS results. Again a good agreement between the results of the two methods can be seen over the entire frequency band. Here in the case of both HFSS and SCT the convergence criterion for each configuration is determined at the centre frequency only and the

results over the entire frequency band are calculated using this convergence criterion (mesh description in the case of HFSS and the number of modes in the case of SCT).

It would be interesting to plot the variation of reflection coefficient phase with respect to the change in the incidence. The variation of phase results of TE_{00} mode with the change in the incidence angle can be seen in Figure I.17. It can be seen that for certain configurations the variation of phase is over a much larger range than the others. The direction of the phase change for each configuration is indicated by the grey arrows.

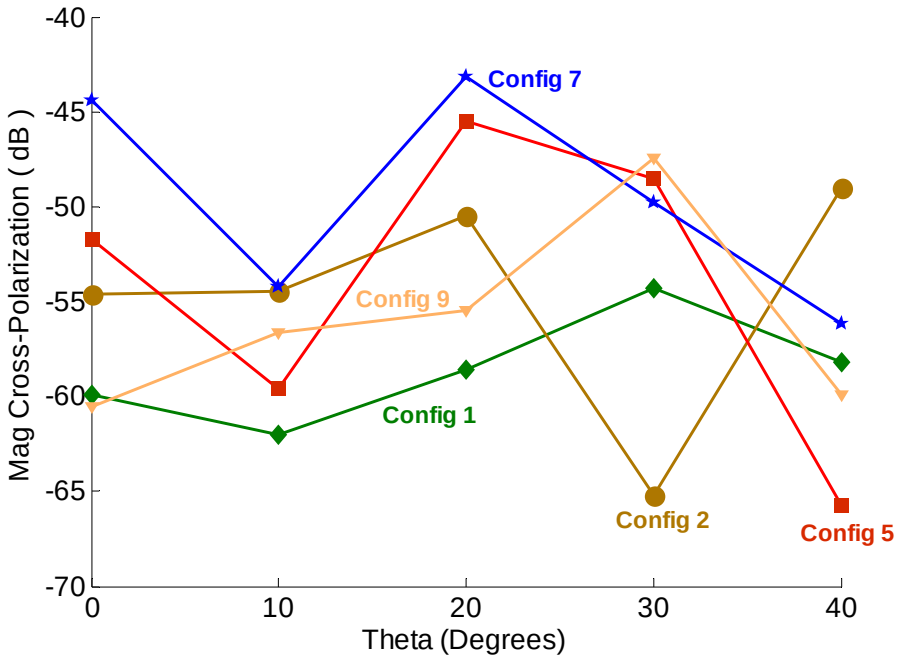

Figure I.17: Variation of the magnitude of S_{12} with respect to the incidence angle.

The coupling between the modes TE_{00} and TM_{00} gives the measure of cross-polarization component of the back-scattered field. The magnitude of $\mathbf{S_{12}}$ is plotted in Figure I.18 for five different configurations. It is apparent from the results that the inter-modal coupling is very small (lower than -40dB) for all configurations and for all incidence angles in $\varphi=0^{o}$ plane.

I.4. CONCLUSIONS

In this chapter we have presented the underlying theory of the Scale-changing Technique and explained certain concepts involved in the application of this technique to the planar structures. It has been shown that the Scale-changing Technique is particularly suited for the applications that require large complex planar geometries with patterns varying over a wide scale-range. The concept of scale-changing network to model electromagnetic coupling between adjacent scale-levels is introduced and it is shown that the computation of these SCNs is mutually independent. This formulation, by its very nature is highly parallelizable, which gives SCT a huge advantage over other techniques that have to be adapted for distributed processing.

In the second half of this chapter the Scale-changing technique is applied to the case of a typical reflector cell under infinite array conditions. The results for the phase-shift introduced to a linearly polarized plane-wave under both normal and oblique incidence are calculated and compared to the results obtained by another simulation tool. The good agreement between the results demonstrates that SCT is a reliable design and simulation technique.

SECTION II:

ELECTROMAGNETIC MODELING USING SCALE-CHANGING TECHNIQUE (SCT)

II.1. INTRODUCTION

In the previous section we have detailed the underlying theory and working of scale-changing technique with the example of passive reflector under infinite array conditions. In this section we will see how this technique can be used to efficiently model large arrays of non-uniform geometry.

First of all we will introduce the concept of a bifurcation multipole which is essentially a scale-changing network to model the electromagnetic coupling between neighboring cells in an array. Mutual coupling between two planar dipoles will be characterized with the help of this scale-changing network and it will be demonstrated that in the case of a planar dipole array the mutual coupling effect is accurately taken into account when modeled using SCT. Later we will use the bifurcation scale-changing network to compute the surface impedances of 1-D arrays of metallic strips and patches inside a parallel plate waveguide. A comparison of simulation-times with that of conventional techniques will be made to emphasize the efficiency of SCT.

Later in the section, the concept of this bifurcation scale-changing network is enhanced to incorporate the mutual coupling in 2-D arrays. Large non-uniform planar array structures are analyzed for plane-wave scattering problem and a good agreement is obtained with the simulation results of conventional simulation tools. Later these structures are analyzed using pyramidal horn as an excitation source. Results are presented for two source configurations i.e. when the source horn is placed at a vertical distance from the centre of the array and when the horn is placed at an offset with an angle of incidence. A comparison of simulation times is given for each case.

II.2. MODELING OF INTER-CELLULAR COUPLING

II.2.1. Bifurcation Scale-changing Network

Consider a small array of two unit-cells placed side by side horizontally. Each of the unit-cells can be characterized independently by its *surface-impedance matrix* (SIM) using an ortho-normal modal-basis defined on unit-cell's domain. To model the overall behavior of this simple two-cell array, mutual electromagnetic interactions between the cells have to be taken into account. These mutual interactions are characterized by a scale-changing network which when cascaded with the surface impedance matrices of individual unit-cells will give the overall surface impedance or admittance that characterizes this array. The parent-domain Ω_0 along with the sub-domains Ω_1 and Ω_2 (unit-cell domains) can be visualized as the openings of a bifurcated waveguide as shown in Figure II.1, the scale-changing network multipole is therefore dubbed as the *bifurcation multipole*.

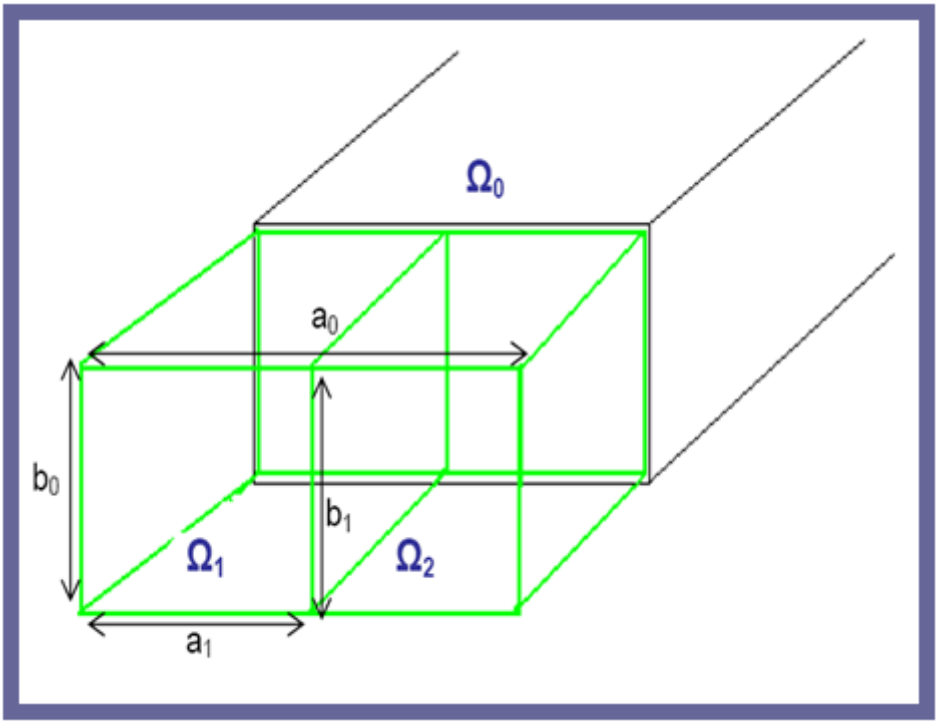

Figure II.1: Electromagnetic coupling between two adjacent unit-cell domains D_1 and D_2 modeled by a waveguide bifurcation. Inter-modal coupling between parent domain D_0 and daughter domains D_1 and D_2 can be represented by a bifurcation Scale-changing network.

Note that in the case of a linear array (unit-cells arranged in one dimension) of non-uniform cells, electromagnetic modeling of an entire array is a simple iterative cascade of the *bifurcation scale-changing networks* as shown in the Figure II.2.

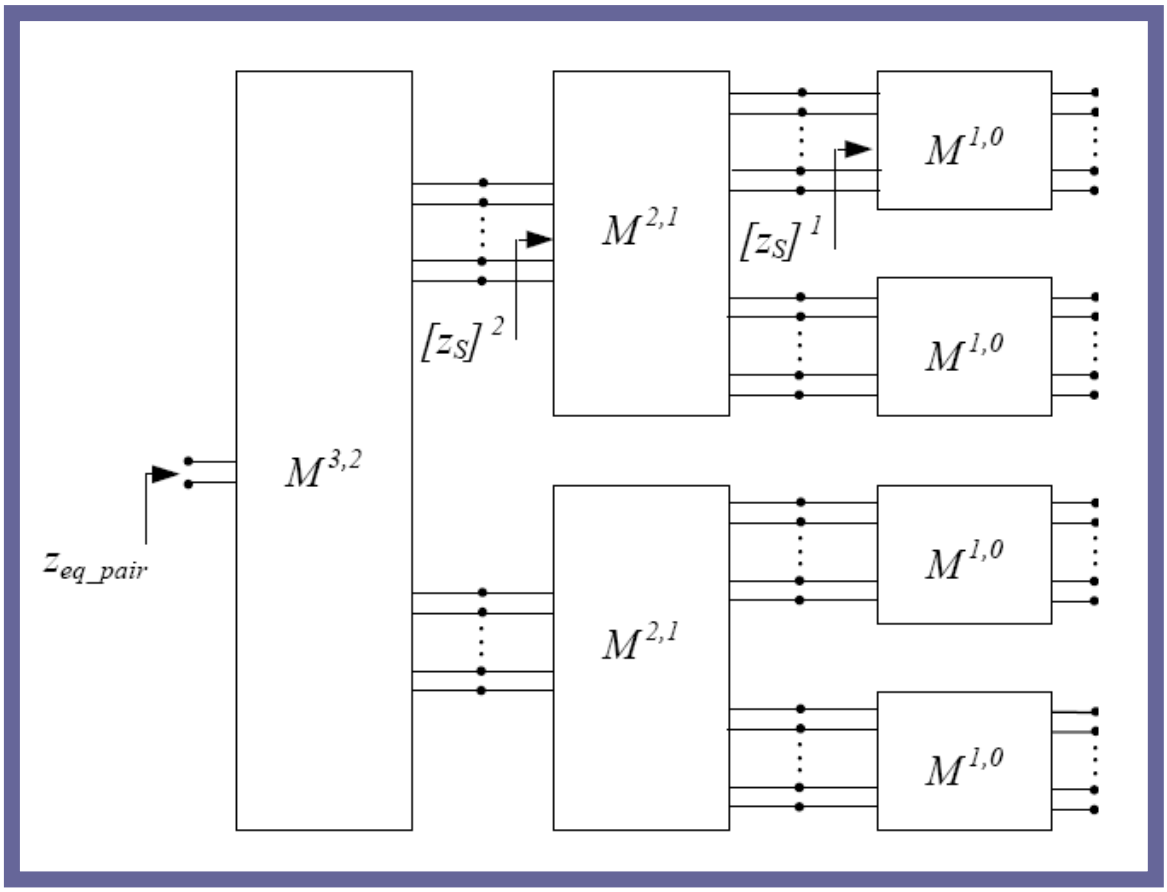

Figure II.2: Cascade of Bifurcation Multipoles to model the mutual coupling of a linear array.

II.2.1.1. Equivalent Circuit Diagram:

The equivalent circuit to compute the bifurcation scale-changing network between a generic scale *s* and its subsequent scale *s-1* is represented in Figure II.3. Electromagnetic sources forming the two branches of the circuit model the transverse fields in the two sub-domains lying at scale *s-1*. The source part of the circuit represents the excitation electromagnetic fields of scale-level *s* as described in Section-I of this thesis.

The current sources $j_e^{(1)}$ and $j_e^{(2)}$ are the virtual-sources defined in the aperture domains to model the perfect dielectric boundary conditions. The electric field scale-changing sources $e^{(1)}$ and $e^{(2)}$ on the other hand represent the tangential electromagnetic fields in the aperture domains. The tangential electromagnetic field in the parent domain D_0 (at scale *s*) is represented by the source **E**. Virtual sources and the scale-changing sources when defined in the same domain and using the same modal-basis can be modeled by a single equivalent source [PerretTh Pg-27]. This simplification reduces the analytical calculations of the circuit. A simplified version of equivalent circuit is thus shown in Figure II.4 with the new equivalent current sources $j^{(1)}$ and $j^{(2)}$.

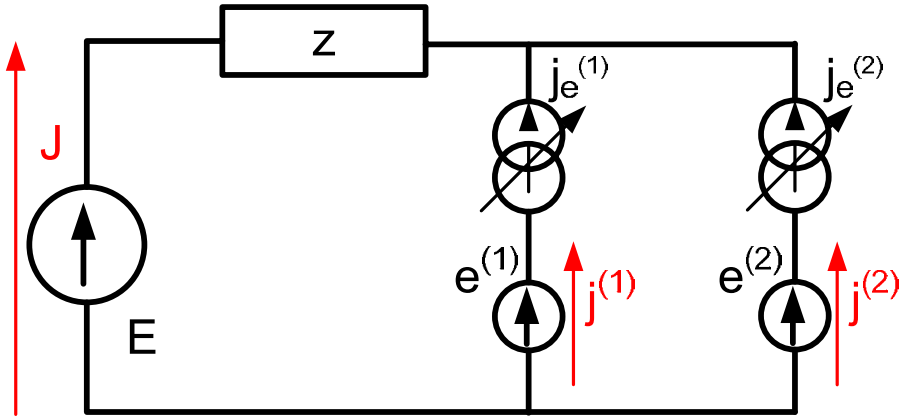

Figure II.3: Equivalent circuit diagram of a bifurcation Scale-changing Network. The dual quantities are shown in red.

Assuming N1 active modes in D_0 and N2 in each of the daughter domains (D_1, D_2) we can express the electromagnetic field quantities in terms of mathematical equations written using the equivalent circuit of Figure II.4.

$$\begin{cases} \vec{E} = \sum_{n=1}^{N1} V_n \vec{F}_n \\ \vec{J} = \sum_{n=1}^{\infty} I_n \vec{F}_n \end{cases} \quad \textbf{(II.1)}$$

$\vec{F}_n$ is the orthogonal modal-basis defined in D_0. Similarly,

$$\hat{Z} = \sum_{n=N1+1}^{\infty} \left|\vec{F}_n\right\rangle Z_n \left\langle\vec{F}_n\right| \quad \textbf{(II.2)}$$

where Z_n is the equivalent parallel modal impedance in the two half-regions. For example, if we have two different substrates at the two sides of the discontinuity plane, assuming air on one side and a dielectric with relative permittivity ε_r on the other, modal impedance of the nth passive mode Z_n is the parallel equivalent of modal impedances of that mode in each of the dielectric domain and is written as:

$$Z_n = \frac{Z_n^{\varepsilon_0} Z_n^{\varepsilon_r}}{Z_n^{\varepsilon_0} + Z_n^{\varepsilon_r}} \tag{II.3}$$

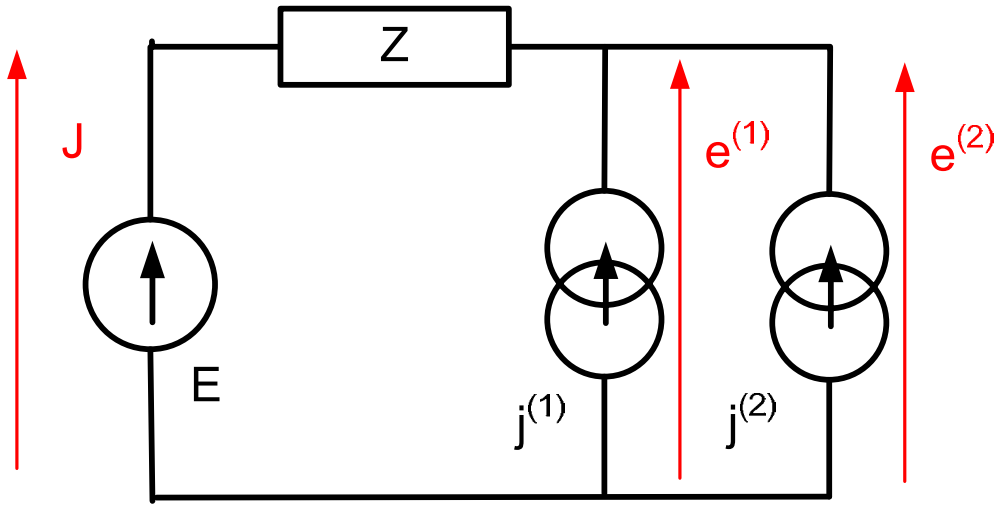

Figure II.4: Simplified Equivalent circuit. Virtual source and the scale-changing source of each branch (when defined in the same domain and using same orthogonal modal-basis) can be replaced by a single current source.

$[I]$ and $[V]$ are the column vectors of size $N1$ listing the coefficients of equation II.1.

$$[I] = \begin{bmatrix} I_1 \\ \vdots \\ I_{N1} \end{bmatrix} \qquad [V] = \begin{bmatrix} V_1 \\ \vdots \\ V_{N1} \end{bmatrix} \tag{II.4}$$

Considering the modal-basis $\boldsymbol{f_n^{(1)}}$ and $\boldsymbol{f_n^{(2)}}$ in the two sub-domains the tangential fields in them can be expressed on their respective modal-basis. For sub-domain D_1

$$\begin{cases} \overrightarrow{\boldsymbol{J^{(1)}}} = \sum_{n=1}^{\infty} i_n^{(1)} \overrightarrow{\boldsymbol{f_n^{(1)}}} \\ \overrightarrow{\boldsymbol{e^{(1)}}} = \sum_{n=1}^{\infty} v_n^{(1)} \overrightarrow{\boldsymbol{f_n^{(1)}}} \end{cases} \tag{II.5}$$

similarly for sub-domain D_2,

$$\begin{cases} \overrightarrow{\boldsymbol{J^{(2)}}} = \sum_{\boldsymbol{n=1}}^{\infty} i_n^{(2)} \overrightarrow{\boldsymbol{f_n^{(2)}}} \\ \overrightarrow{\boldsymbol{e^{(2)}}} = \sum_{\boldsymbol{n=1}}^{\infty} v_n^{(2)} \overrightarrow{\boldsymbol{f_n^{(2)}}} \end{cases} \quad \textbf{(II.6)}$$

with the coefficient vectors of eq-II.5 and eq-II.6 are defined on the active-modes in each sub-domain.

$$\left[i^{(k)}\right] = \begin{bmatrix} i_1^{(k)} \\ \vdots \\ i_{N2}^{(k)} \end{bmatrix} \qquad \left[v^{(k)}\right] = \begin{bmatrix} v_1^{(k)} \\ \vdots \\ v_{N2}^{(k)} \end{bmatrix} \quad \forall\, k = 1,2 \qquad \textbf{(II.7)}$$

In order to compute the multipole-matrix that characterizes the bifurcation multipole, we need to find a relation between the quantities defined in the parent domain to that defined in sub-domains. As these quantities are defined on the active-modes of their respective modal-basis, they form the ports through which tangential fields at one scale can interact with the tangential fields of the other. The relation between the fields at two scales can be written from the equivalent circuit of Fig-II.4 using Kirchoff's laws.

$$\begin{bmatrix} J \\ e^{(1)} \\ e^{(2)} \end{bmatrix} = \begin{bmatrix} 0 & -1 & -1 \\ 1 & \hat{Z} & \hat{Z} \\ 1 & \hat{Z} & \hat{Z} \end{bmatrix} \times \begin{bmatrix} E \\ j^{(1)} \\ j^{(2)} \end{bmatrix} \quad \textbf{(II.8)}$$

Solving the matrix equation of eq-II.8 by applying Galerkin's method gives the following:

$$\begin{bmatrix} [I] \\ \left[v^{(1)}\right] \\ \left[v^{(2)}\right] \end{bmatrix} = \begin{bmatrix} 0 & -P_1^{(1)} & -P_1^{(2)} \\ P_1^{(1)T} & P_2^{(1)T} Z P_2^{(1)} & P_2^{(1)T} Z P_2^{(2)} \\ P_1^{(2)T} & P_2^{(2)T} Z P_2^{(1)} & P_2^{(2)T} Z P_2^{(2)} \end{bmatrix} \times \begin{bmatrix} [V] \\ \left[i^{(1)}\right] \\ \left[i^{(2)}\right] \end{bmatrix} \quad \textbf{(II.9)}$$

where T denotes the complex conjugate transpose. If M denotes the multipole-matrix that characterizes the bifurcation-multipole which relates the tangential fields at scale *s* and *s-1* defined on the active modes, then eq-II.9 can be rewritten as under:

$$\begin{bmatrix} [I] \\ \left[v^{(1)}\right] \\ \left[v^{(2)}\right] \end{bmatrix} = [M] \times \begin{bmatrix} [V] \\ \left[i^{(1)}\right] \\ \left[i^{(2)}\right] \end{bmatrix} \quad \textbf{(II.10)}$$

The constituent sub-matrices of M are defined here. $\left[P_1^{(k)}\right]$ is the projection matrix of dimensions $N1 \times N2$ of active modes of modal-basis $\vec{\boldsymbol{F}}_{\boldsymbol{n}}$ on $\vec{\boldsymbol{f}}_{\boldsymbol{n}}^{(k)}$;

$$\left[P_1^{(k)}\right] = \begin{bmatrix} \langle F_1, f_1^{(k)} \rangle & \cdots & \langle F_1, f_{N2}^{(k)} \rangle \\ \vdots & \ddots & \vdots \\ \langle F_{N1}, f_1^{(k)} \rangle & \cdots & \langle F_{N1}, f_{N2}^{(k)} \rangle \end{bmatrix} \quad \forall\, k = 1,2 \qquad \textbf{(II.11)}$$

Similarly $\left[P_2^{(k)}\right]$ is the projection matrix of dimensions $(M - N1) \times N2$ of passive modes of modal-basis $\vec{\boldsymbol{F}}_{\boldsymbol{n}}$ on $\vec{\boldsymbol{f}}_{\boldsymbol{n}}^{(k)}$.

$$\left[P_2^{(k)}\right] = \begin{bmatrix} \langle F_{N1+1}, f_1^{(k)} \rangle & \cdots & \langle F_{N1+1}, f_{N2}^{(k)} \rangle \\ \vdots & \ddots & \vdots \\ \langle F_M, f_1^{(k)} \rangle & \cdots & \langle F_M, f_{N2}^{(k)} \rangle \end{bmatrix} \quad \forall\, k = 1,2 \qquad \textbf{(II.12)}$$

The bifurcation multipole defined by the matrix $[M]$ characterizes the electromagnetic coupling between two consecutive scale-levels and serves as a basic block to model the mutual coupling between the elements of an array structure.

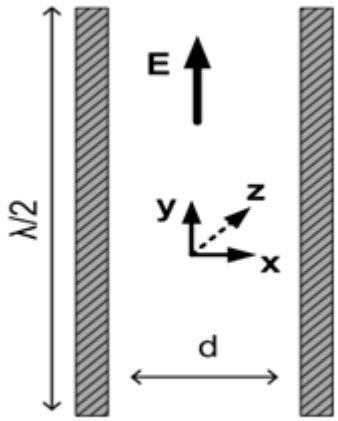

Figure II.5: Scattered Electric Field from two half-wavelength dipoles separated by a distance 'd' allows characterizing the mutual coupling with respect to distance.

II.2.2. Mutual Coupling between half-wave dipoles

To demonstrate that the scale-changing network described in the previous section accurately models the mutual coupling between the elements of an array, a classical example of mutual coupling between two half-wave dipoles has been considered in this section.

Two thin metallic strips of half-wavelength dimensions are represented in Figure II.5 separated by a distance ***d*** between them. Given a plane-wave incidence, a half-wave dipole reradiates the field uniformly around its axis but in the elevation cut-plane the maximum radiated energy is along θ=0º direction (z-axis taken out of the plane containing dipoles). We will use the magnitude of electric field in the maximum energy direction as a parameter of measure for the mutual coupling between the two dipoles.

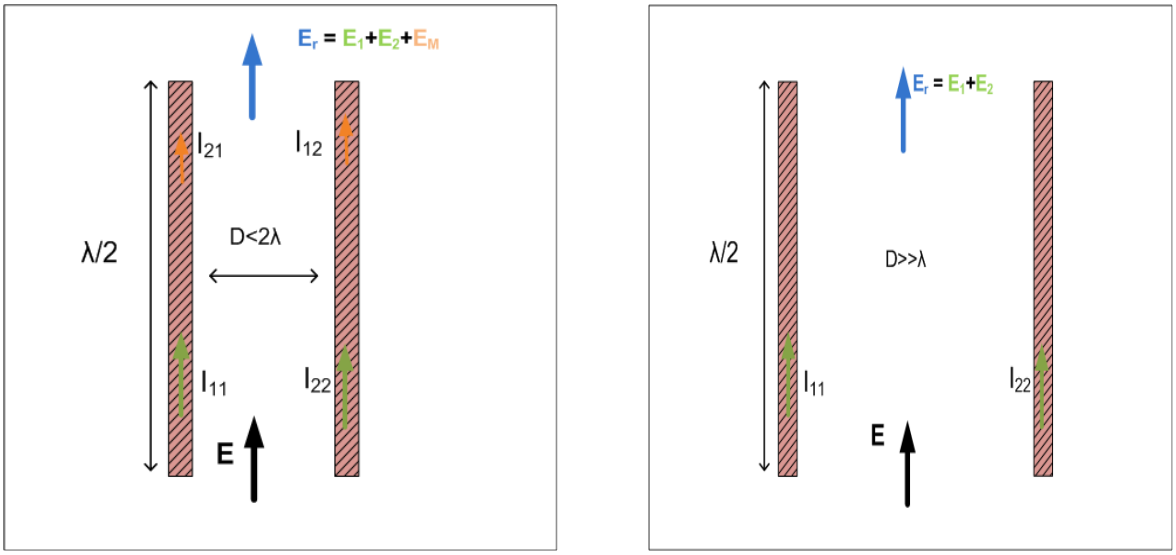

Figure II.6: Mutual coupling effect disappears when the separation D is many orders of wavelength.

The phenomenon can be illustrated as shown in Fig-II.6. An incidence field **E** induces the surface currents I_{11} and I_{22} on the two dipoles. These induced currents will in turn induce coupling currents I_{21} and I_{12} on the neighboring dipole. The radiated field $\mathbf{E_r}$ is thus comprised of three components; E_1 and E_2 are radiated by current sources I_{11} and I_{22} where component E_M is radiated by the coupling currents I_{21} and I_{12} and is a function of dipole separation. In the absence of mutual coupling e.g. when

the distance between the two dipoles is many orders of wavelength, E_M is zero and the total radiated field $\mathbf{E_r}$ is a simple summation of the individual fields radiated by each dipole.

Figure II.7 plots the Radar cross-section ratio (SER ratio) of a couple of dipoles to that of an isolated dipole computed analytically. The analytical expression is given by the following equation:

$$\frac{\sigma}{\sigma_0} = \frac{4}{\left|1 + \frac{Z_{12}}{Z_{22}}\right|^2}$$

where Z_{22} is the input impedance of a single dipole as seen by the incident plane-wave and is constant. Z_{12} on the other hand is the mutual impedance of the two dipoles and is a function of separation (d) between them. In the absence of the mutual coupling Z_{12} reduces to zero and we have a fixed value of the SER ratio that computes to 6dB. When *d* is equal to zero, the two dipoles overlap and are essentially seen as a single dipole and the SER ratio reduces to one (or 0 dB). As the separation is progressively increased a steadily decreasing sinusoidal behavior is observed around fixed SER ratio of 6dB. The sinusoidal nature can be attributed to the constructive or destructive nature of mutual interactions between the coupling currents induced by the incident wave on the two dipoles. As the separation increases in terms of wavelength, the mutual interactions tend to die out and the SER ratio tends towards the fixed SER ratio of 6dB.

As the radar cross-section is directly proportional to the scattered field E_r a similar behavior can be seen when E_r is plotted against *d* and therefore the radiated field can be used to characterize the effect of mutual coupling between two dipoles.

$$\sigma = 4\pi r^2 \frac{\left|\vec{E}_r\right|^2}{\left|\vec{E}_{inc}\right|^2}$$

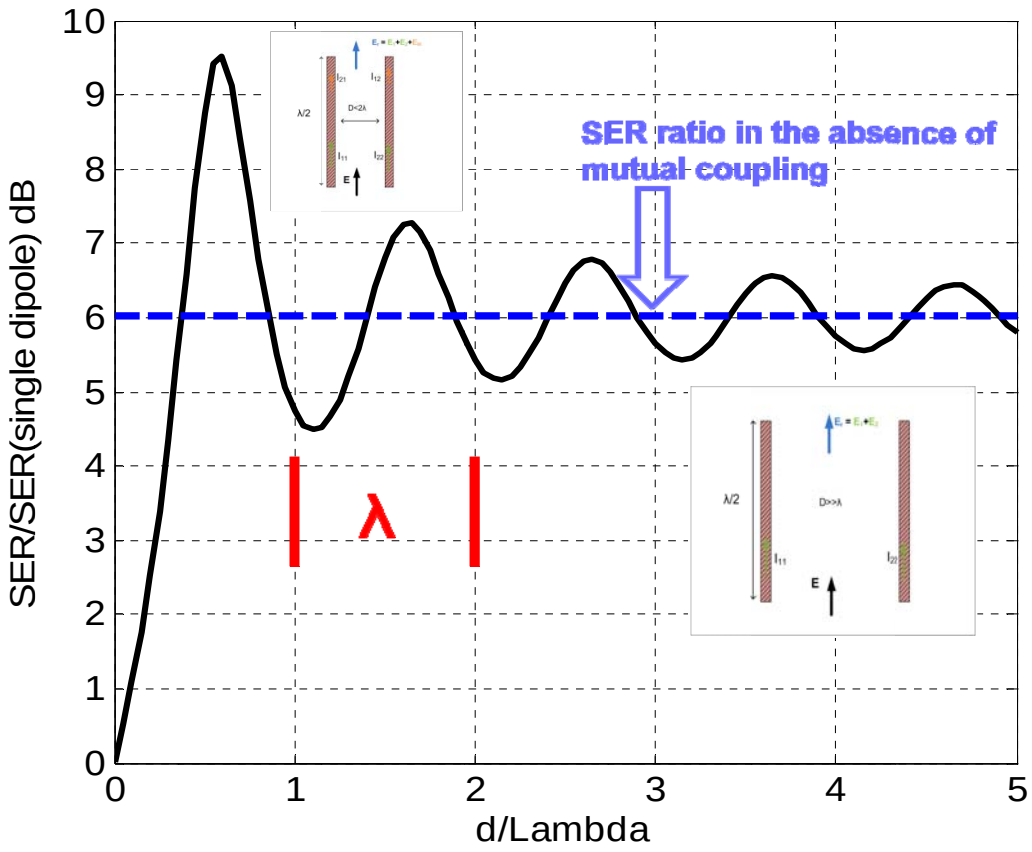

Figure II.7: Variation of the SER ratio of the dipoles with respect to separation 'd'. Blue dotted line shows the SER ratio in the absence of mutual coupling.

II.2.2.1 Simulation Results

Two rectangular dipole strips of lengths 12mm each are simulated as a simple two cell array under plane-wave incidence. A single scale-changing network is required to characterize the mutual coupling between the two strips. The strips were simulated multiple times by varying the distance between them. The radiated E-field (computed along θ=0º φ=0º direction) is plotted against the separation ***d*** varied over one wavelength (Fig-II.8).

The steadily decreasing sinusoidal behavior with respect to the separation *d* is apparent from the results of Fig-II.8. The reradiated field in the absence of mutual coupling can be found by simple summation of reradiated fields by isolated dipoles. This is represented by the dotted straight line at the centre of the plot.

Although the sinusoidal nature of the curve shows the presence of significant mutual coupling between the dipoles, to validate that the bifurcation scale-changing network can accurately model its effect, the SCT results need to be compared to those obtained by another full-wave analysis method. The same problem was simulated using a MOM based technique (IE3D) and the results are presented in the plot of Fig-II.8 for validation purposes. It is found that the results obtained by two techniques agree closely which validates the point that SCT accurately characterizes the effects of mutual coupling between the elements of an array.

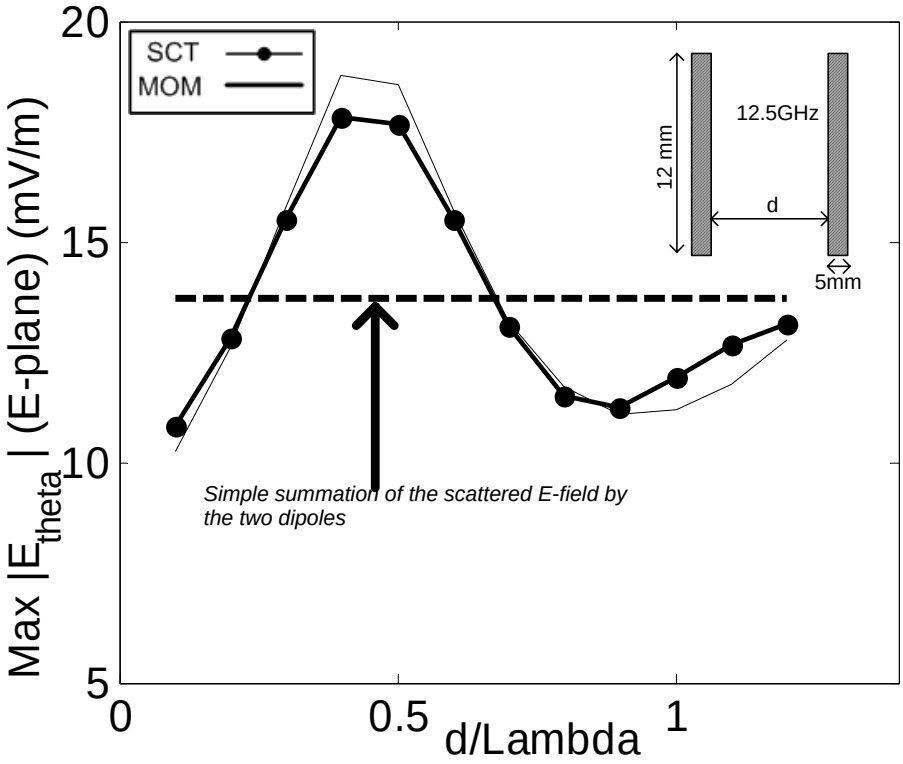

Figure II.8: Characterization of mutual coupling for two dipole strips at 12.5GHz. SCT results (-o-) IE3D results (---)

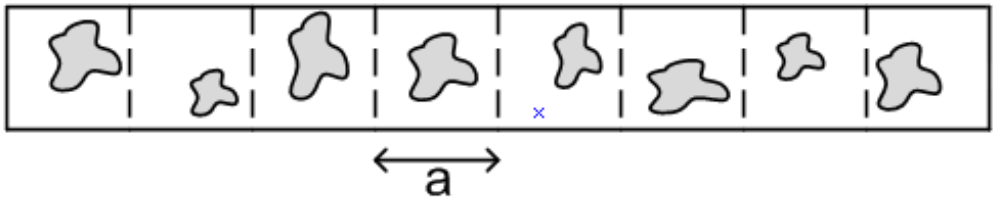

Figure II.9: One dimensional (linear) array of non-uniform unit-cells. Dotted lines mark the unit-cell boundaries. Non-uniformity arises from the arbitrary shape of the metallic pattern of each unit-cell.

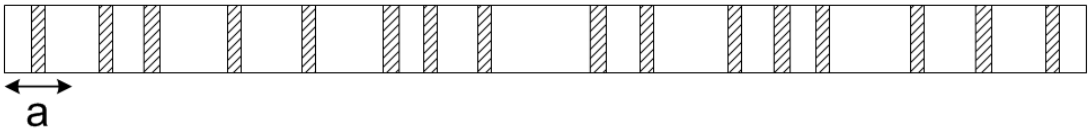

(a)

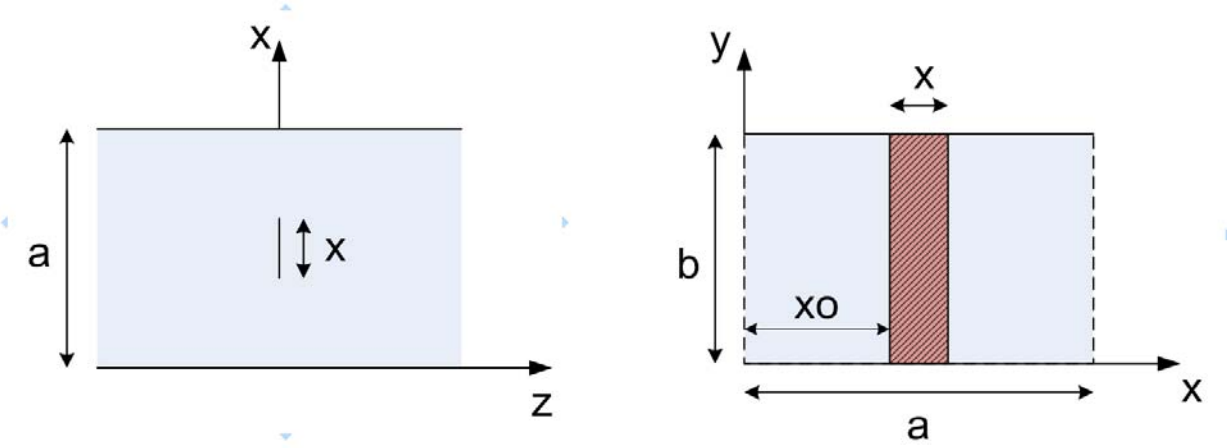

(b) **(c)**

Figure II.10: (a) A finite 1-D non-uniform array of infinitely thin and lossless metallic strips (b) A typical unit-cell when placed inside a parallel plate waveguide (c) Transverse discontinuity plane at z=0. Dotted lines represent PMBC. Solid lines (top and bottom) represent PEBC. a=10mm b=9mm x=2mm @ 5 GHz

II.3. MODELING OF NON-UNIFORM LINEAR ARRAYS (1-D)

II.3.1. Introduction

In this section the characterization of linear arrays using iterative cascading of bifurcation scale-changing networks will be demonstrated. Later on in this chapter a similar procedure will be employed to the full-wave analysis of large 2-D planar arrays.

A general 1-D non-uniform finite array of arbitrary shaped patches is shown in Figure II.9. The non-uniformity arises from the fact that each unit cell has a different geometry from that of its neighboring cells. Therefore the mutual coupling between cells can vary over a large scale between various neighbors. Analysis techniques used for uniform array structures which assume uniform mutual coupling between all cells may not be applied in this case and can lead to inaccurate results especially near the resonance frequencies of the metallic patterns where mutual coupling is strong.

The tools capable of modeling precise mutual coupling in non-uniform arrays promise more robust designs. To demonstrate the advantages of SCT in modeling of finite non-uniform array problems it is applied to a special case of 1-D non-uniform array of thin metallic strips. The strips are of uniform width though the position of each strip within the unit-cell is variable. As the distance between neighboring strips varies the mutual coupling between them is not constant.

II.3.2. Characterization of a metallic-strip array

The problem of electromagnetic diffraction from a thin lossless metallic strip is very well known. It has been shown that the higher order modes excited by the presence of a lossless metallic strip discontinuity inside a rectangular waveguide are purely inductive in nature [Collin91]. Therefore a linear array of metallic strips can be characterized by its equivalent inductance inside a parallel-plate waveguide.

A finite, non-uniform 1-D array of perfectly conducting thin metallic strips is shown in Figure II.10 (a). A unit-cell consisting of a single strip is shown in Figure

II.10 (b) and Figure II.10 (c). Position of the strip along x-axis can be varied to obtain several different unit-cell configurations. Several of these unit-cells can then be combined to form a 1-D array.

II.3.2.1 Application of Scale-changing Technique

The application of Scale-changing Technique requires the partitioning of array-plane in domains and sub-domains defined at various scale levels. For instance an array consisting of 8 unit-cells can be partitioned as shown in Figure II.11. At the lowest scale (s=1) the domains are defined along the unit-cell boundaries. At scale-level 2 two adjacent unit-cell domains can be modeled into a single domain using bifurcation network making four domains at scale 3. This iterative process goes on until the entire array domain is reached at the top-most scale.

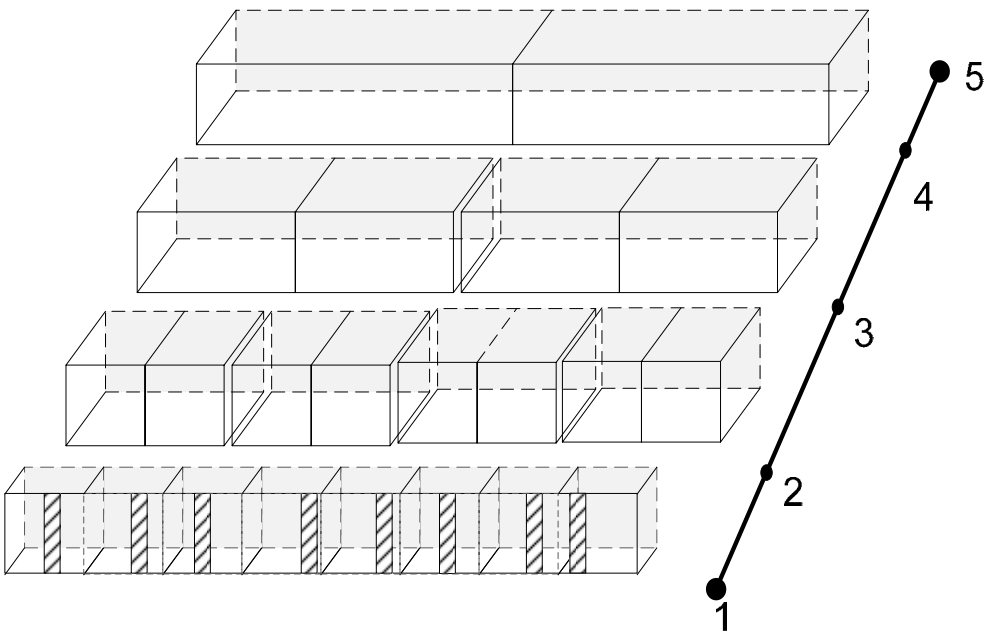

Figure II.11: Decomposition of the discontinuity plane in five scale-levels.

Each of the unit-cell is modeled alone and is represented by its characteristic *surface impedance multipole [Zs]*. Two of these unit-cells can be grouped together by cascading a bifurcation SCN multipole with the surface impedance multipoles of the unit-cells. At scale-level 2, four bifurcation multipoles are required to group eight

cells. Similarly at scale-level 3, two bifurcations are required to group eight cells and finally at the fourth scale only one bifurcation multipole is needed.

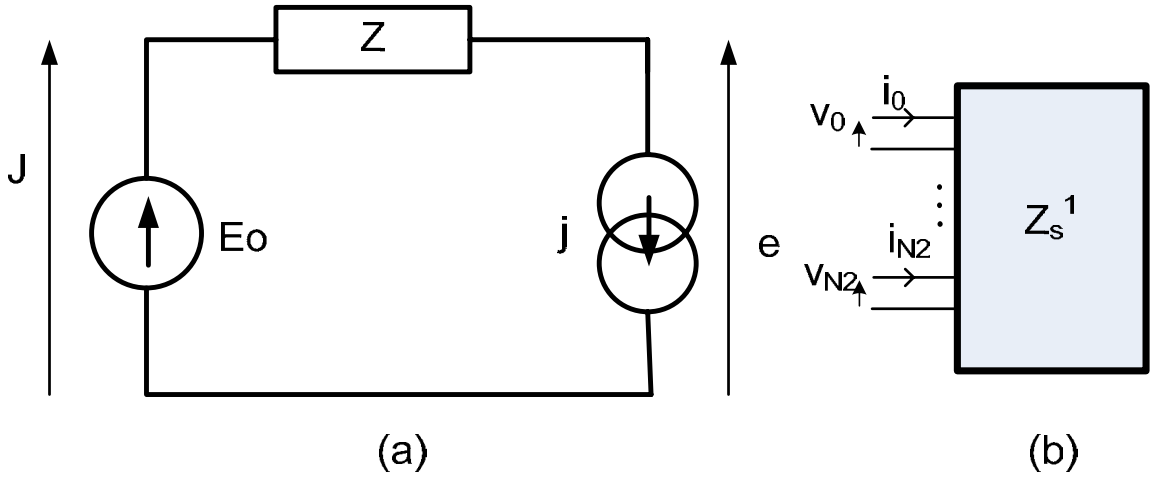

Figure II.12: (a) Equivalent circuit diagram representing a unit cell metallic-strip discontinuity (b) Surface Impedance Multipole defined on the active modes of the unit-cell domain.

It is worth noting here that the computation of all multipoles, at which-ever scale they are present, is mutually independent of one another. This essentially means that each multipole can be computed in parallel on separate machines and it is only as a final step the resulting matrices are cascaded to obtain the overall simulation results for the entire structure.

II.3.2.1.1 Computation of Surface Impedance Multipole

The computation of surface impedance multipole [Zs] has to be performed for each unit-cell. The problem can be represented by the equivalent circuit diagram of Figure II.12 (a). The voltage source $\mathbf{E_0}$ represents the tangential electric field defined on the active modes of the unit-cell domain. The impedance operator **Z** represents the modal impedances of higher order modes that are excited due to the presence of metallic strip discontinuity. And the current source **j** represents the surface currents induced on the strip. Galerkin's method is applied to compute surface impedance matrix (Z_{surf}) which characterizes the surface impedance multipole. It should be noted here that the number of active modes would be chosen by a comprehensive

convergence study to precisely define the coupling between two adjacent scales. The boundary value problem for the first unit-cell domain at scale-level 1 can be expressed as:

$$[v] = \left[Z_{surf}\right][i] \qquad \textbf{(II.13)}$$

where the ***v*** and ***i*** are defined on **N2** active modes of the domain.

$$[v] = \begin{bmatrix} V_0 \\ \vdots \\ V_{N2} \end{bmatrix} \qquad [i] = \begin{bmatrix} i_0 \\ \vdots \\ i_{N2} \end{bmatrix} \qquad \textbf{(II.14)}$$

II.3.2.1.2 Computation of Bifurcation Multipole

The computation of a general bifurcation multipole matrix between a scale *s* and subsequent scale *s-1* was given in section II.2 and is represented mathematically by equation II.10.

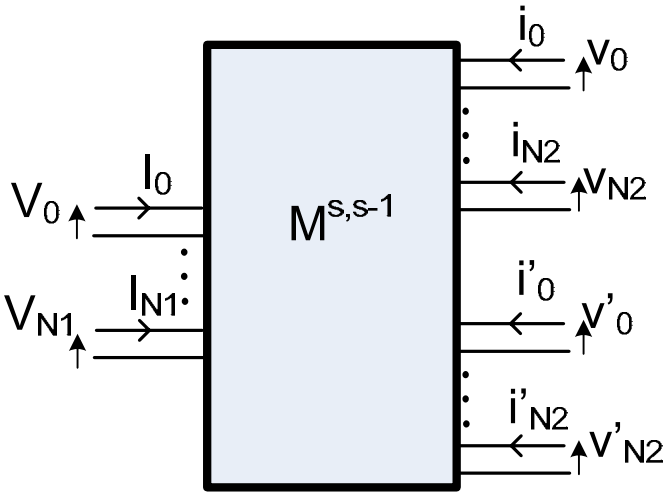

Figure II.13: Bifurcation Scale-changing Network Multipole characterizes mutual coupling between scale-level 's' and 's-1'

The scale-changing network multipole between a domain at scale *s* and two sub-domains at scale *s-1* in represented in Fig-II.13. The tangential field defined on **N1** active modes of the parent domain is represented by **N1** ports on the LHS of the scale-changing network. The fields defined in the two sub-domains, defined on active modes (**N2** and **N2'**) are represented by two sets of ports on the right-hand side. This field interaction can be expressed analytically by the following matrix equation:

$$\begin{bmatrix} [I] \\ [v^{(1)}] \\ [v^{(2)}] \end{bmatrix} = [M^{s,s-1}] \times \begin{bmatrix} [V] \\ [i^{(1)}] \\ [i^{(2)}] \end{bmatrix} \quad \textbf{(II.15)}$$

$[M^{s,s-1}]$ can be expressed in its component sub-matrices.

$$[\mathrm{M}^{s,s-1}] = \begin{bmatrix} [\mathrm{M11}] & [\mathrm{M12}] & [\mathrm{M13}] \\ [\mathrm{M21}] & [\mathrm{M22}] & [\mathrm{M23}] \\ [\mathrm{M31}] & [\mathrm{M32}] & [\mathrm{M33}] \end{bmatrix} \quad \textbf{(II.16)}$$

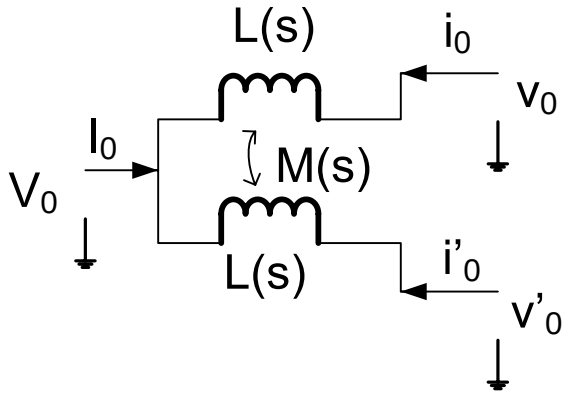

Figure II.14: Electrical Model of the Bifurcation SCN Multipole defined on single TEM mode in each domain.

II.3.2.1.3 Computation of the cascade

The complete simulation of full array is performed by a simple cascade of all scale-changing networks and their underlying surface impedance multipoles. A general cascade step of this iterative process is computed by the following equation.

$$\left[[Y_{surf}^{s,1}\right] = [\mathrm{M11}] - \left([[\mathrm{M12}] \quad [\mathrm{M13}]] \times \left(\begin{bmatrix} [Z_{surf}^{s-1,1}] & [0] \\ [0] & [Z_{surf}^{s-1,2}] \end{bmatrix} + \begin{bmatrix} [\mathrm{M22}] & [\mathrm{M23}] \\ [\mathrm{M32}] & [\mathrm{M33}] \end{bmatrix} \right)^{-1} \times \begin{bmatrix} [\mathrm{M21}] \\ [\mathrm{M31}] \end{bmatrix} \right) \quad \textbf{(II.17)}$$

$[Z_{surf}^{s-1,1}]$ and $[Z_{surf}^{s-1,2}]$ are surface impedance matrices characterizing the sub-domains at scale *s-1*. $[Y_{surf}^{s,1}]$ which characterizes the parent domain at scale *s*, is found by cascading SCN $[M^{s,s-1}]$ with $[Z_{surf}^{s-1,1}]$ and $[Z_{surf}^{s-1,2}]$. The relation of these impedances with the quantities of eq-II.15 is given by:

$$\left[v^{(1)}\right] = -\left[Z_{surf}^{s-1,1}\right]\left[i^{(1)}\right] \qquad \left[v^{(2)}\right] = -\left[Z_{surf}^{s-1,2}\right]\left[i^{(2)}\right] \quad \textbf{(II.18)}$$

$$[\mathrm{I}] = \left[Y_{surf}^{s,1}\right][\mathrm{V}] \quad \textbf{(II.19)}$$

For a very simple case where all tangential fields are defined on a single mode (e.g. TEM mode) the bifurcation multipole can be represented by its equivalent electrical network of two inductances as shown in the Fig-II.14. The mutual coupling between the domains can be visualized by the mutual inductance in this case.

II.3.2.2 Simulation Results and Discussion

Consider a unit-cell shown in Fig-II.10 (c) placed in a parallel plate waveguide. The objective is to determine the equivalent inductance presented by this strip under the excitation of the fundamental TEM mode. The symmetry of the problem along the z-axis permits to treat the problem in even and odd order solutions by using perfect magnetic boundary conditions (PMBC) and perfect electric boundary conditions (PEBC) in the discontinuity plane at z=0. It is clear that for the second case the solution reduces to zero due to short circuit produced at the discontinuity plane by PEBC. Therefore we are interested only in the even order solution where the discontinuity plane is characterized by PEBC in the metallic strip region and PMBC in the non-metallic region.

Configuration	Inductance (nH)	
	SCT	HFSS
A (x0= 0mm)	8.46	8.89
B (x0= 2mm)	4.85	5.19
C (x0= 4mm)	4.0	4.32
D (x0= 6mm)	4.87	5.19
E (x0= 8mm)	8.51	8.89

Table II.1. List of possible unit-cell configurations and their inductance results in single-cell environment.

We can obtain five possible configurations of the unit-cell by simply displacing the metallic strip along the x-axis. Table II.1 lists all five configurations. These configurations are named A, B, C, D and E and they will be used as the constituent building blocks to construct finite arrays. The equivalent inductance values for each of the configuration as obtained by SCT and HFSS are listed in the second and third column respectively. For a single cell the problem can be solved analytically [Aubert03] to validate the SCT results.

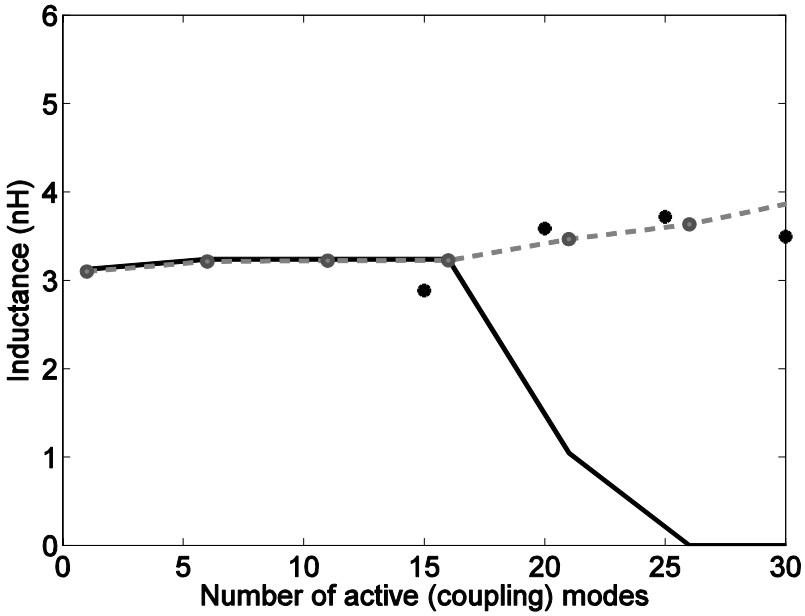

Figure II.15. Convergence results for a 2-cell array. Note matrix ill-conditioning problem for more than 15 modes for a classical mode-matching technique. Padé approximants (o) and conjugate gradient method (-o-) can be used to improve convergence by increasing the number of modes without introducing large numerical errors at a cost of increased simulation times.

Figure II.15 depicts the convergence results for a two-cell array (configuration CC), when the array is modeled using one bifurcation stage. Here the inductance curve is plotted with respect to the number of active modes taken in each unit-cell domain. It is apparent from the plot that the choice of mode count is limited due to matrix ill-conditioning problem [VoyerTh] if more than 15 modes are taken.

Two techniques have been used to overcome this problem in our case. Padé approximants [Brezinski94] can be used to extend the range of modes to reach

convergence without encountering the ill-conditioned matrices but this approach is not easily applicable for 2-D problems [Bose80]. Alternatively an iterative technique called method of Conjugate Gradients [Sarkar84] can be employed to compute the unit-cell surface impedance multipoles which can then be cascaded with bifurcation multipole to model overall problem. The curves resulting from the two techniques are plotted against each other in Fig-II.15. It can be noted that the convergence is achieved in both cases over a larger range of active modes.

Array Size	Simulation Time (sec)	
	SCT	HFSS
1 cell	0.14	18
2 cells	0.59	27
4 cells	0.61	33
8 cells	0.64	36
16 cells	0.68	55
32 cells	0.71	53

Table II.2. Simulation times comparison for SCT and HFSS.

1-D array of 2^n strip elements can be constructed by cascading ***n*** levels of bifurcation multipoles. Table II.2 lists the inductance results for finite arrays of various sizes with number of cells ranging from 2 to 32. The execution time comparison is made for SCT and HFSS simulations. It is clear from the results that for SCT the simulation time increases linearly with the exponential increase in number of array cells, whereas in HFSS which is linear-meshing technique execution time increase exponentially with every additional mesh-refinement. This difference in execution times will be more apparent for the applications with complex unit-cell geometries. These simulations are carried out on a PC with x86 based processor with clock frequency of 3.19 GHz and 2GB of RAM. The convergence criterion used in HFSS simulations is to achieve 2% of convergence on S-parameters matrix.

Figure II.16 plots the results of convergence for a 16 cell array with respect to active-modes at the unit-cell domain. It can be seen that 30 modes are enough to define precise coupling at that scale level. To define intermediate coupling between different bifurcation levels no more than 10 modes are necessary. It is clear that for more complex structures we will need a lot more modes to reach convergence.

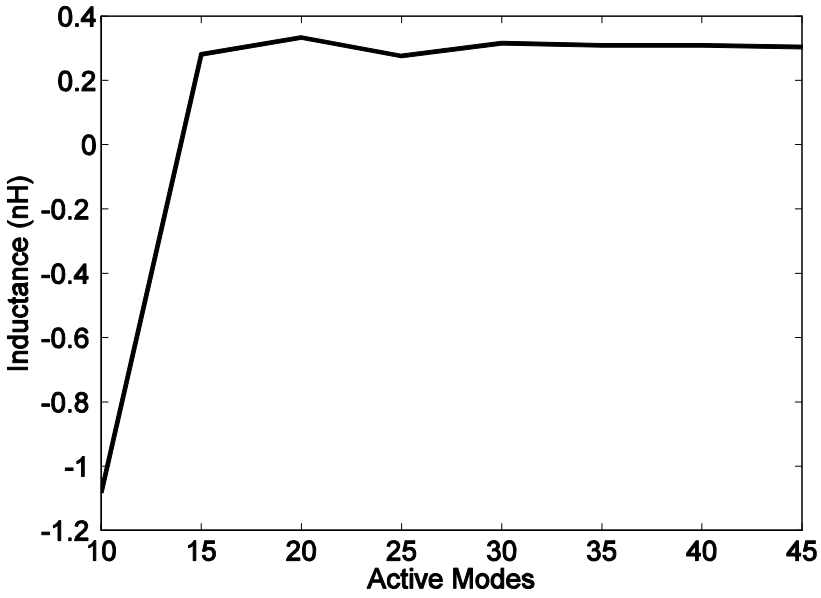

Figure II.16. Convergence results for a 16-cell array.

Array Size	Unit-cell Arrangement	Inductance (nH)	
		SCT	HFSS
2 cells	BC	2.34	2.13
2 cells	DB	2.57	2.30
4 cells	DACD	1.30	1.24
16 cells	ABCDBCABECAABAAD	0.30	0.29
32 cells	EAEAEAEAEAEAEAEA EAEAEAEAEAEAEAEA	0.27	0.26

Table II.3. Inductance results for non-uniform arrays

Various sized 1-D strip arrays with different unit-cell configurations arranged in no-particular order are simulated and the results are presented in Table II.3. Here the results for array comprised of up to 32 unit-cells are presented. For larger arrays HFSS fails to converge with the available amount of memory.

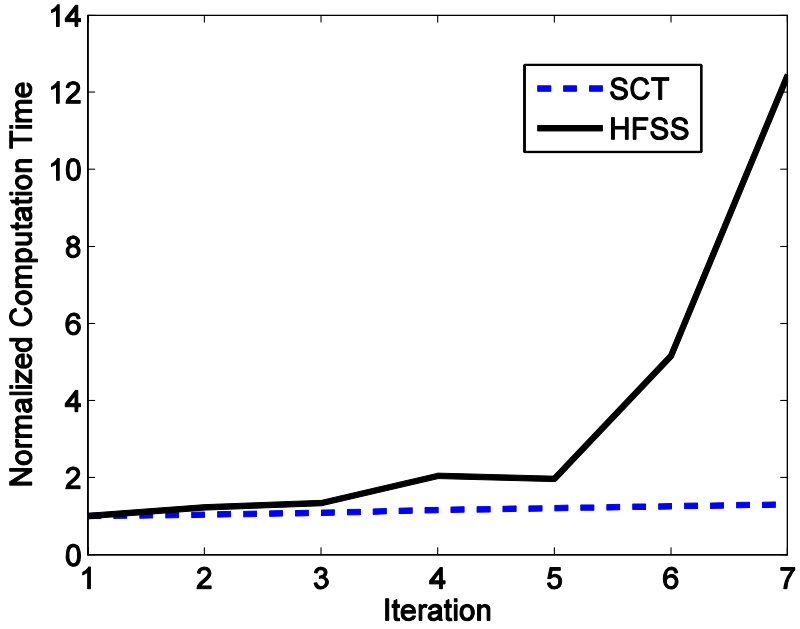

Figure II.17. Evolution of the normalized computation time with respect to bifurcation iterations used. For an iteration *n* the array consists of 2^n cells.

The evolution of computation time with respect to the array size is traced in Figure II.17 for the two simulation techniques. Number of bifurcation iterations is taken along horizontal axis. For an iteration **n** the array size is equal to $\mathbf{2^n}$ cells. The computation time is normalized with respect to the time taken to compute a simple two-cell array using a single bifurcation network. It is quite obvious from the plot that the simulation time increases linearly in case of SCT though there is an exponential increase in the array size. On the other hand for HFSS the evolution of computation time is exponential. It can be concluded from these results that real advantage of SCT over conventional methods is when the array-size is really large i.e. when seven or more bifurcation iterations are involved.

II.3.3. Characterization of a metallic-patch array

In previous section SCT was applied to a linear array of metallic strips. In that case our problem was symmetric along y-axis and therefore the analytical expressions for the modal-basis were simplified (no y-dependence). In real life rectangular patches are most commonly in planar radiators and scatterers therefore it would be interesting to simulate linear arrays of variable sized metallic patches.

II.3.3.1 Introduction

Consider the 1-D non-uniform patch array of Fig-II.18 (a). Each unit-cell of the array is different from the other in terms of difference in dimensions of its patch. Consider a typical unit-cell of such an array shown in Fig-II.18 (a & b) when placed inside a parallel plate waveguide. The patch is considered to be infinitely thin and lossless. In its isolated state each cell can be characterized by its surface-impedance matrix multipole, where each port represents a propagating mode in the parallel plate waveguide. An entire array can be characterized in a similar fashion. The numerical results presented here correspond to TEM mode excitation. Figure II.19 depicts four unit-cell configurations named A, B, C and D that will be used to construct the arrays.

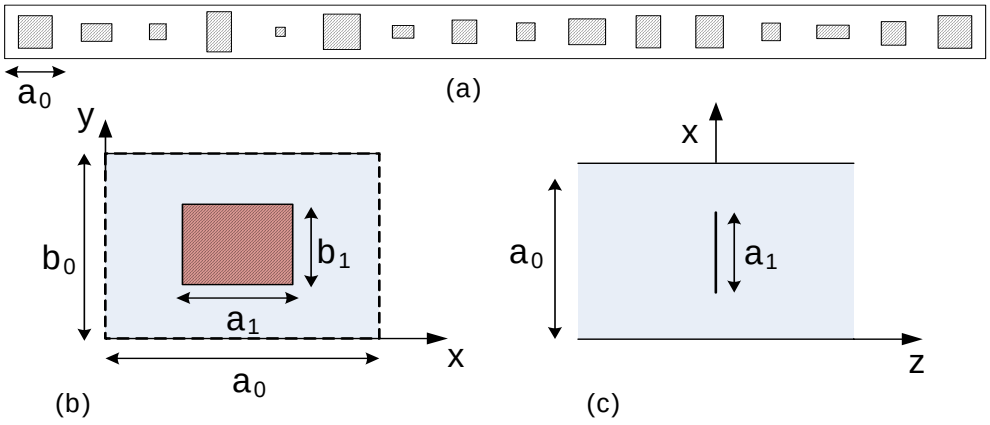

Figure II.18: (a) A finite 1-D non-uniform array of lossless metallic patches (b) A typical unit-cell when placed in a parallel plate waveguide (at z=0) a0=10mm, b0=10mm, (c) Longitudinal view (patch thickness = 0)

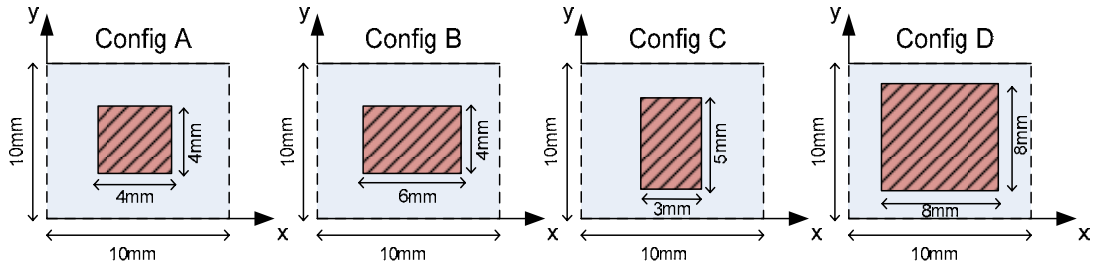

Figure II.19: Four unit-cell configurations that are used to construct 1-D finite arrays of Table.I. Patch dimensions for each configuration given as (a1(mm),b1(mm)) are A(4,4), B(6,4), C(3,5), D(8,8)

The process of discontinuity plane decomposition and the assigning of scale-levels to various domains and sub-domains is the same as in metallic strip array case.

Array Size	Unit-cell Arrangement	Reactance (kΩ)	
		SCT	HFSS
2 cells	BC	-3.41	-3.42
4 cells	BCDA	-0.62	-0.63
8 cells	CBBADADC	-0.33	NC
8 cells	CBABCBBB	-0.87	-0.88
16 cells	BACADBACCABBADAB	-0.23	-0.20
32 cells	DCCCCADDCDCCDDAD CABCDDCCCBACDADD	-0.06	NC

Table II.4. Reactance results for non-uniform arrays

II.3.3.2 Simulation Results and Discussion

Table-II.4 lists equivalent reactance results for six different linear and non-uniform arrays at 5GHz. The first column gives the cell arrangement of the array e.g. array BC comprises of two unit-cells and is formed by placing the unit-cell configurations B and C (Fig-II.19) side by side. A good agreement is found between

the SCT and HFSS results for the first, second and fourth array. For the fifth array HFSS results converge only after relaxing the convergence criterion i.e. from less than 0.2% to less than 2% of variation in S-matrix values for two consecutive passes. This explains the relatively greater difference from SCT results in this case. For the third and sixth cases HFSS results do not converge even with the relaxed criterion.

Figure II.20 plots the simulation time against the array-size in case of the two simulation techniques. If the array-size is represented in the number of unit-cells (N) then for each size-iteration (I) the size of the array is given as $N=2^I$. In other words, for each size-iteration the unit-cells in the array double from the previous value. For each technique execution time results are normalized with respect to the time required to simulate an array of two unit-cells (I=1). The results of Figure II.20 are obtained for a uniform array made up of unit-cell configuration A.

Note that in case of SCT the execution time increases linearly with increase in the number of size-iterations (I=ln(N)/ln(2)). However this is not the case for HFSS which uses linear mesh-refinement procedure. The behavior is similar to that observed in the metallic strip array case as expected. The linear behavior of SCT comes from the fact that for all unit-cells being similar only one Scale-Changing Network needs to be calculated to represent all of them. This allows faster and better convergence for SCT results as compared to Finite Element Method using spatial meshing. In case of non-uniform arrays the linear behavior can be achieved by executing individual Scale-Changing Networks in parallel on multiple processors. The simulation time results presented are for 3.2GHz Intel x86 Family processor with 2GB RAM.

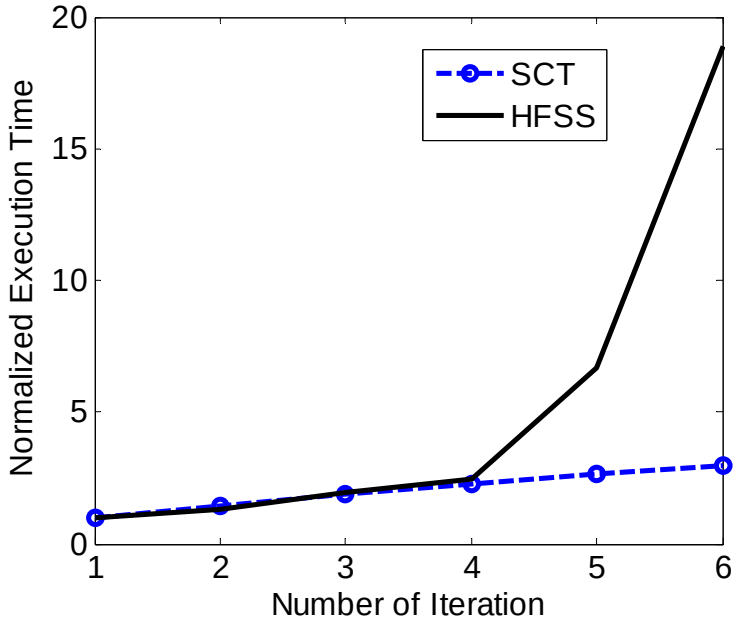

Figure II.20: Evolution of the normalized computation time with respect to bifurcation iterations used. For an iteration *n* the array consists of 2^n cells.

II.4. MODELING OF 2-D PLANAR STRUCTURES

II.4.1. Introduction

In the section-II.2 the concept of bifurcation scale-changing network was introduced and later applied to model linear array discontinuities in parallel-plate waveguides. A similar formulation can be used in the case of a scattering problem involving two dimensional planar structures e.g. Frequency selective surfaces and Reflectarrays.

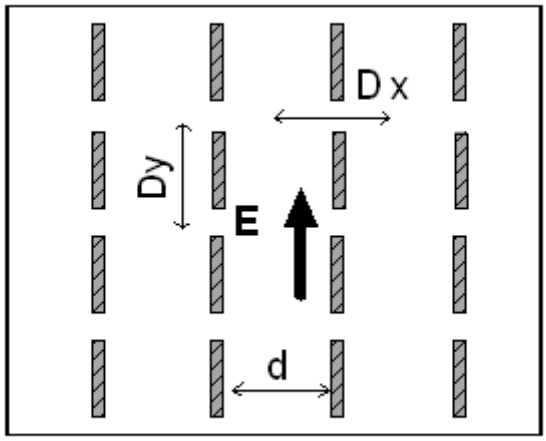

Figure II.21: A 4x4 array of half-wave dipoles under Normal plane-wave incidence.

The scattering problem requires the resolution of a free-space boundary-value problem in which the planar array can be characterized by its surface impedance matrix. The diffraction field patterns can then be calculated from the equivalent surface current induced on the planar surface due to the incident fields [BalanisTh]. Mathematical formulation of the problem is presented in the sub-section II.4.3.

II.4.2. Mutual coupling with 2-D Scale-changing Network

To study the mutual coupling effect in case of a small two-dimensional array, a small 4x4 array of dipole strips has been simulated under normal plane-wave incidence as depicted in Fig-II.21. The dipole elements are separated horizontally by

a distance of half wavelength to maximize the mutual coupling effects between the elements. In this case the scale-changing multipole groups the elements in two dimensions i.e. mutual coupling between four elements is considered in the computation of a single scale-changing network.

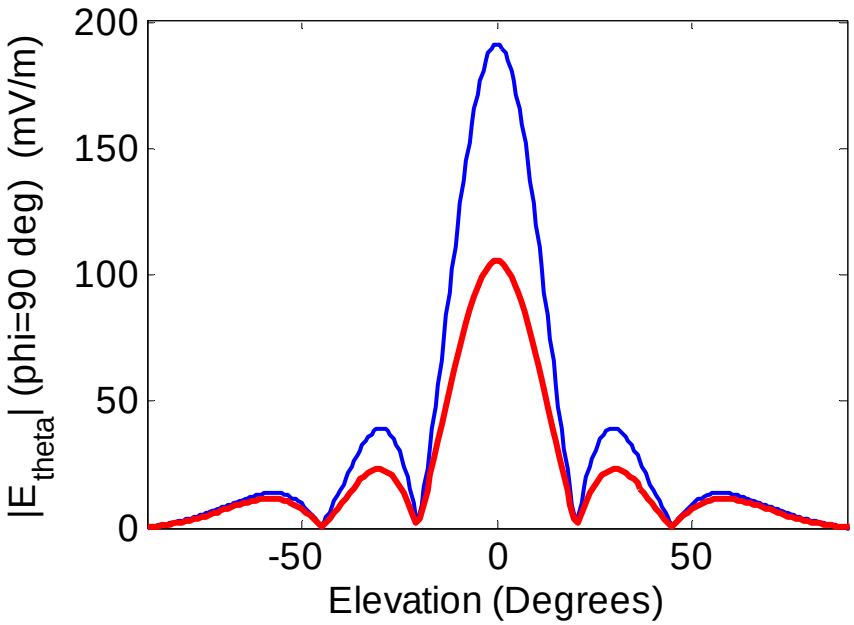

(a)

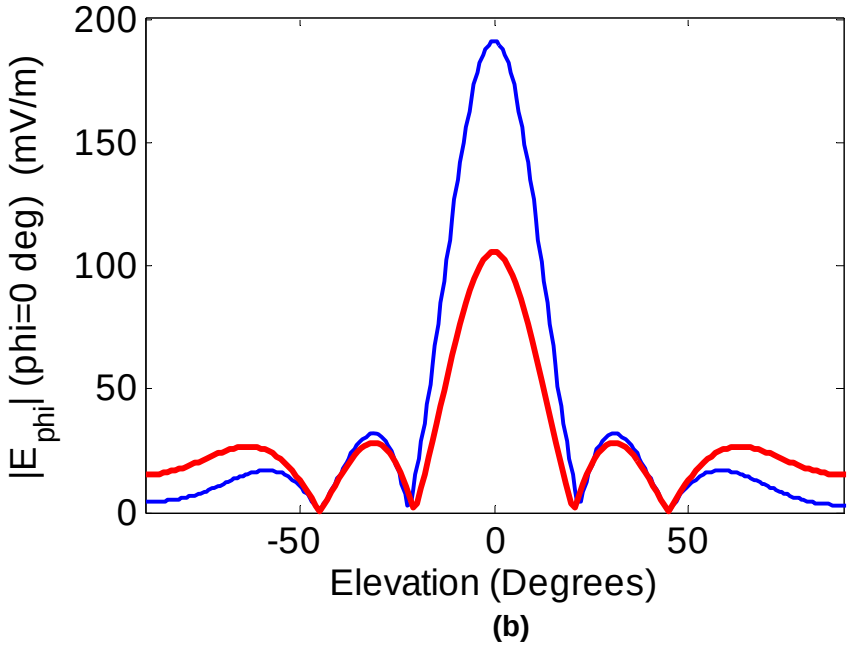

(b)

Figure II.22: Scattering field pattern of a simple 4x4 dipole array for (a) H-plane (b) E-plane. SCT results (blue) takes into account the effect of mutual coupling. Array pattern as calculated from the Array Factor computation neglecting the mutual coupling (red).

To account properly for all mutual coupling effects a convergence study has to be done to ensure that enough coupling modes are considered in the computation of scale-changing networks. Too few modes and the inter-cellular interactions are not well-defined and too many can produce ill-conditioned matrices and other unwanted numerical errors.

The radiation patterns plots in H-plane and E-plane of the array are represented in Fig-II.22 for the normal plane-wave incidence with the incident E-field oriented along the axis of the dipole strips. The radiation pattern of the array in the absence of mutual coupling as computed using the radiation pattern of a single element using the array factor [BalanisAnt] of the 4x4 dipole array is also traced on the same plot for comparison purposes. It is quite apparent from the results that if the mutual-coupling effects are ignored the results can be very different from the actual results and therefore the precise characterization of inter-cellular coupling is vital for planar array problems.

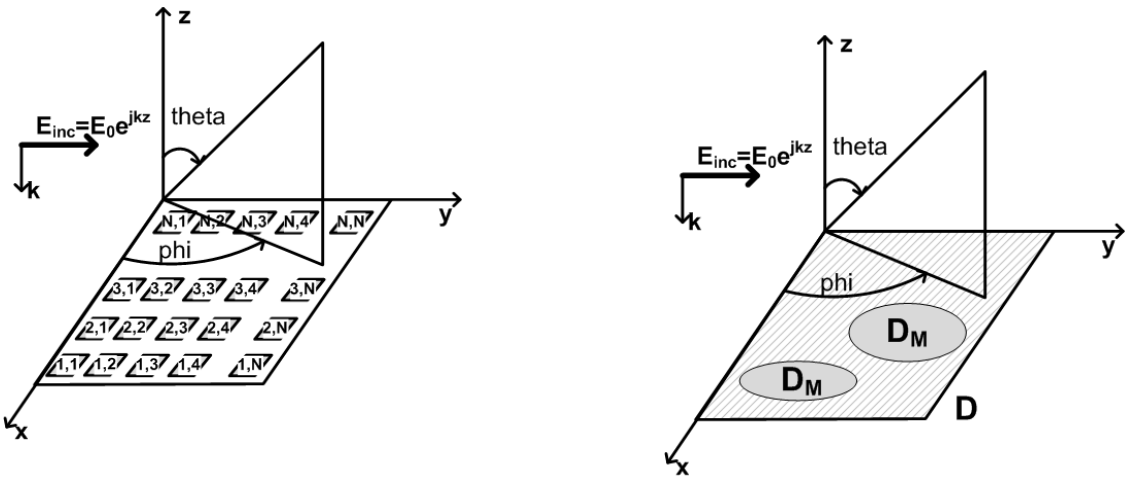

(a) **(b)**

Figure II.23: (a) An NxN array of arbitrary elements under normal plane wave incidence. For all results E-plane and H-plane are elevation planes defined at (φ=90º) and (φ=0º) respectively (b) Array domain (D) with equivalent surface current J; Metal domain (DM)

II.4.3. Formulation of the scattering problem

This sub-section discusses the theory of electromagnetic scattering from a thin planar array. Consider a plane-wave at a normal incidence on an array of finite extent made from unit-cells of arbitrary metallic patterns (Fig-II.23a). These cells are arranged on a two dimensional rectangular lattice. To solve the scattering problem from this regular array first consider a more general planar structure comprised of metal and dielectric regions (Fig-II.23b). The domain D_M denotes the metallic domain which is the sub-set of the array domain D. The time-harmonic regime is assumed for all fields.

II.4.3.1 Derivation of the current density on the array domain D

The integral equation formulation of the boundary value problem on metal domain D_M in the case of planar scatterer of Fig-II.23b can be written as:

$$\vec{E}_{inc}(r) + \vec{E}_{scat}(r) = 0 \qquad for\ r \in D_M \tag{II.20}$$

Where $\vec{E}_{inc}(r)$ and $\vec{E}_{scat}(r)$ denote the incident and scattered field respectively. The total tangential field is zero as dictated by the perfect electric boundary conditions at the metal surface. The scattered field from a planar surface can be written in terms of unknown surface current density $\vec{J}$ on the metal domain D_M and free space Green's functions $G(r,r')$ [Vardaxoglou97].

$$\vec{E}_{scat}(r) = \int_{D_M} G(r,r')\vec{J}(r')dr' \tag{II.21}$$

The primed co-ordinates r' correspond to the observation point.

With SCT, we substitute the current $\vec{J}$ defined on the metal domain (D_M) by an equivalent current $\overrightarrow{J_{eq}}$ defined on the entire array domain (D). The planar surface domain D is characterized by a surface impedance matrix $[Z_s]$ (which fixes the new boundary conditions of the problem) such as:

$$\vec{E}^{total} = [Z_s] * \overrightarrow{J_{eq}} \tag{II.22}$$

The boundary value problems at all scale-levels in SCT are formulated in spectral domain therefore it is convenient to evaluate the scattering problem in the spectral domain as well. Thus the new formulation in spectral domain can be written by using eq-II.20 and eq-II.21 in eq-II.22:

$$\vec{E}_{inc}(r) + \hat{G}\overrightarrow{J_{eq}} = [Z_s]\overrightarrow{J_{eq}} \quad \textbf{(II.23)}$$

Where $\hat{\mathrm{G}}$ designates the Green function (in operator form) in the spectral domain.

Artificial boundary conditions (PPWG BC) are first introduced at the contour of the domain D. These boundary conditions are assumed not to perturb significantly the electromagnetic field of the original problem. They allow defining an orthogonal set of discrete modes for expanding the unknown surface current density J_{eq} in the domain D as given by the following mathematical expression.

$$\vec{J}_{eq} = \sum_{i=1}^{NXN} \vec{I}_{eq\_i}\vec{g}_{eq\_i} \quad \textbf{(II.24)}$$

$\vec{g}_{eq\_i}$ being the orthogonal modal basis in D and N being the number of active modes along each dimension of the planar domain.

In practice, same entire-domain orthogonal basis functions are used for this expansion as well as for representing the equivalent surface impedance matrix $[Z_s]$ that models the array. The number of modes may be determined à posteriori from convergence criteria of the numerical results. The derivation of $[Z_s]$ from the scale-changing technique will follow in the subsection *II.4.3.1.3*.

To determine the scattered electric field when illuminated by a plane wave, the equivalent surface current density J_{eq} in the domain D needs to be calculated. This current density may be computed from the resolution of the following matrix equation derived from the Integral Equation Formulation of the boundary value problem given by eq-II.23 using Galerkin's method [Harrington96] [Harrington61].

$$[\mathrm{I_{eq}}] = \left[\left[\mathrm{Z_{space}}\right] + [\,\mathrm{Z_s}]\right]^{-1} [\mathrm{V_{inc}}] \quad \textbf{(II.25)}$$

$[Z_{space}]$ is the matrix representation of the free space Green functions in the spectral domain. $[V_{inc}]$ and $[I_{eq}]$ are the vectors containing known expansion coefficients of the incident electric-field and the unknown coefficients of surface current density J_{eq} defined on the modal-basis of the array-domain D.

II.4.3.1.1 Calculation of [Vinc]

V^{inc} can be obtained from the following scalar product:

$$[V^{inc}] = \langle \vec{g}_{eq\_j}, E^{inc} \rangle = \int_{-\infty}^{+\infty} \int_{-\infty}^{+\infty} \vec{g}_{eq\_j}(x,y)^* \vec{E}^{inc}(x,y)dxdy \quad \textbf{(II.26)}$$

where E^{inc} is the tangential component of the field incident on the planar domain D. For example in the case of plane-wave incidence the tangential component of the incident field can be written as

$$\vec{E}^{inc} = \begin{cases} E_{0x} e^{-j(k_x^i x + k_y^i y)} \vec{x} \\ E_{0y} e^{-j(k_x^i x + k_y^i y)} \vec{y} \end{cases} \quad \textbf{(II.27)}$$

With k_x^i ,k_y^i are the components of the tangential incident-wave vector given by: $\begin{cases} k_x^i = k\cos\theta^i \sin\emptyset^i \\ k_y^i = k\cos\theta^i \cos\emptyset^i \end{cases}$

θ^i and $\emptyset^i$ are the polar angles of incidence.

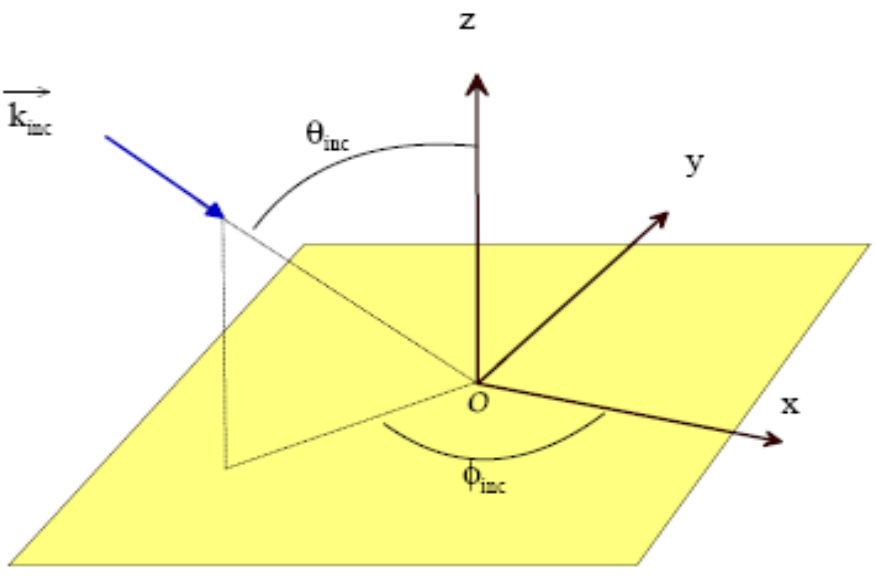

Figure II.23: Co-ordinate system convention for plane-wave incidence.

For antenna sources, $\vec{\mathrm{E}}^{\mathrm{inc}}$ is tangential component of the radiated electric-field incident on the planar surface and can be calculated from the radiation pattern characteristics and the position of the source with respect to the array. This process is outlined in the Annex B for a case of pyramidal horn source. In addition $\vec{\mathrm{E}}^{\mathrm{inc}}$ can be found numerically by simulating the source antenna with any 3-D EM simulation tool (e.g. GRASP) and using the tangential component of the field projected on the array-plane in equation II.26 to find $\mathrm{V}^{\mathrm{inc}}$. Alternatively the projection of antenna measurement data expressed on spherical modes can be used in place of $\vec{\mathrm{E}}^{\mathrm{inc}}$.

II.4.3.1.2 Calculation of $[\boldsymbol{Z_{space}}]$

The calculation of $\boldsymbol{Z_{space}}$ in spatial domain is quite delicate. Indeed the expression of $\boldsymbol{Z_{space}}$ in spatial domain brings up the spatial form of the dyadic Green functions given by the following equation [Harrington96].

$$\varphi(x,y\,;x',y') = \frac{e^{-jk[(x-x')^2+(y-y')^2]^{1/2}}}{4\pi[(x-x')^2+(y-y')^2]^{1/2}} \qquad \textbf{(II.28)}$$

$\mathrm{Z}_{\mathrm{space}}$ can then be found from the following expression obtained by the application of Galerkin's method on equation II.23.

$$\left[\mathrm{Z}_{\mathrm{space}}\right]_{i,j} = -\langle g_{eq\_i}, G * g_{eq\_j}\rangle \qquad \textbf{(II.29)}$$

The spatial formulation of the above equation gives the following complex equation which requires the computation of the convolution product of two functions inside a double integral equation.

$$\left[\mathrm{Z}_{\mathrm{space}}\right]_{i,j} =$$

$$\int_{-\infty}^{+\infty}\int_{-\infty}^{+\infty} \vec{g}_{eq\_i}(x,y)^{*}.\frac{j}{\omega\varepsilon_0}\begin{bmatrix} k_0^2+\frac{\partial^2}{\partial x^2} & \frac{\partial^2}{\partial x\partial y} \\ \frac{\partial^2}{\partial y\partial x} & k_0^2+\frac{\partial^2}{\partial y^2}\end{bmatrix}\varphi(x,y\,;x',y') * \vec{g}_{eq\_j}(x',y')dxdy \qquad \textbf{(II.30)}$$

The convolution product is given by the following equation

$$\varphi(x,y\,;x',y') * g_{eq\_j}(x',y') = \int_{-\infty}^{+\infty}\int_{-\infty}^{+\infty} \frac{e^{-jk\left[(x-x')^2+(y-y')^2\right]^{1/2}}}{4\pi[(x-x')^2+(y-y')^2]^{1/2}} * \vec{g}_{eq\_j}(x',y')dx'dy' \quad \textbf{(II.31)}$$

As the entire domain trial functions are defined in spectral domain it is easier to solve the expression of equation (II.30) in spectral domain rather than spatial domain. Moreover the expression in equation (II.31) simplifies in the spectral domain as the product of convolution in spatial domain becomes a simple multiplication operation in the spectral domain. Fourier transforms are used to achieve this domain transformation:

$$F\big(u(x,y)\big) = \tilde{u}\big(k_x,k_y\big) = \int_{-\infty}^{+\infty}\int_{-\infty}^{+\infty} u(x,y)\, exp\big(-j\big[k_x x + k_y y\big]\big)\, dxdy \quad \textbf{(II.32)}$$

$$F^{-1}\left(\tilde{u}\big(k_x,k_y\big)\right) = u(x,y) = \frac{1}{4\pi^2}\int_{-\infty}^{+\infty}\int_{-\infty}^{+\infty} \tilde{u}\big(k_x,k_y\big)\, exp\big(+j\big[k_x x + k_y y\big]\big)\, dk_x dk_y \quad \textbf{(II.33)}$$

Where F and F^{-1} denote the forward and inverse transforms respectively.

Therefore equation II.30 can be rewritten using Parseval's theorem and utilizing Fourier transform equations as under:

$$\big[\mathrm{Z}_{\mathrm{space}}\big]_{i,j} = \frac{1}{4\pi^2}\int_{-\infty}^{+\infty}\int_{-\infty}^{+\infty} \vec{\tilde{g}}_{eq\_i}\left(k_x,k_y\right)^{*}.\frac{1}{j\omega\varepsilon_0}\begin{bmatrix} k_x^2-k_0^2 & k_xk_y \\ k_yk_x & k_y^2-k_0^2 \end{bmatrix}\tilde{G}\big(k_x,k_y\big)\vec{\tilde{g}}_{eq\_j}\big(k_x,k_y\big)dk_xdk_y \quad \textbf{(II.34)}$$

$\tilde{G}\big(k_x,k_y\big)$ is the spectrum of the free-space Green's function.

$$\tilde{G}\big(k_x,k_y\big) = \begin{cases} \dfrac{-j}{2\sqrt{k_0^2-k_x^2-k_y^2}} & if\ k_0^2 > k_x^2+k_y^2 \\ \dfrac{1}{2\sqrt{k_x^2+k_y^2-k_0^2}} & if\ k_0^2 < k_x^2+k_y^2 \end{cases} \quad \textbf{(II.35)}$$

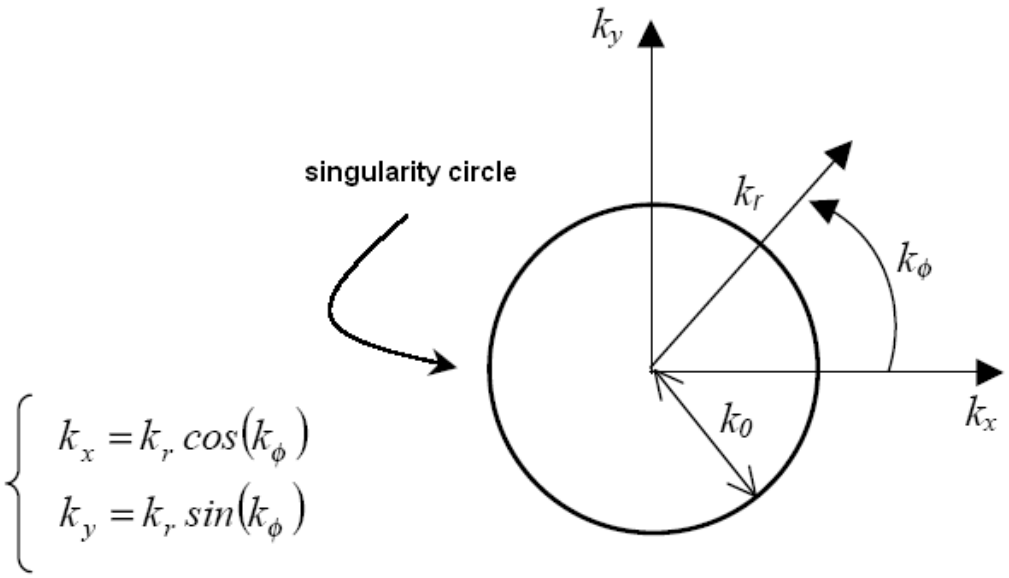

Figure II.24: Wave-vector transformation from Cartesian to Polar co-ordinates.

Thus the computation of Z_{space} has been reduced to the computation of a single double integral in the spectral domain. Moreover since the test functions $\vec{g}_{eq\_n}(x, y)$ are defined in the rectangular domain their Fourier transform can be calculated analytically.

In the computation of the integral of equation II.34 a singularity appears at $k_x^2 + k_y^2 = k_0^2$. While the continuous integral is computed numerically as a discrete sum, the discontinuity can easily be avoided. Using polar co-ordinates k_φ and k_r, singular values of k_x and k_y translates into a circle of $k_r = k_0$ as shown in the Fig-II.24. The numerical computation of the integral in equation II.34 is performed in polar coordinates avoiding the singularity circle.

II.4.3.1.3 Derivation of $[Z_s]$ of the array from the Scale Changing Technique

In a complex discontinuity surface the metallic patterns can be viewed as set of several domains and embedded sub-domains. In order to demonstrate the partitioning process of the discontinuity plane in the case of simple array structures consider the array of Fig-II.23a with individual cells of arbitrary geometry arranged on

a uniform rectangular lattice. For a special case of 16 cell array the process can be described as follows (Fig-II.25):

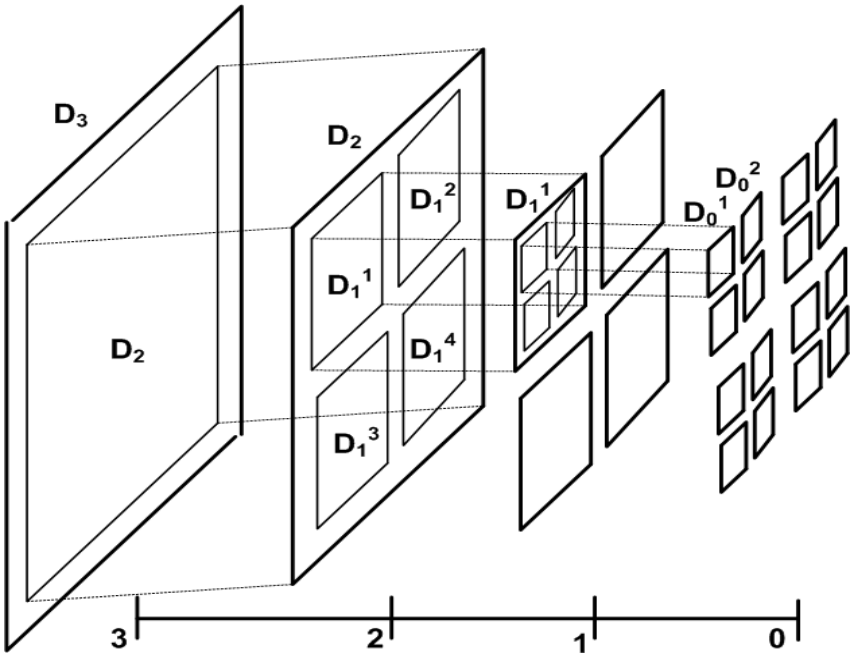

Figure II.25: Decomposition of a 4x4 array in four scale-levels

1) The entire planar domain of the array denoted by D_3 lies at the top most scale-level (s=3). This domain contains all unit-cells plus any border regions around them.

2) D_3 contains a single sub-domain D_2 which is defined at the subsequent scale-level i.e. s=2. D_2 encompasses all 16 unit-cells of the array and contains four sub-domains D_1^1, D_1^2, D_1^3 and D_1^4 all defined at scale-level s=1.

3) Each domain at s=1 contains 4 sub-domains of its own defined at the lowest scale-level s=0 (e.g. D_1^1 contains D_0^1, D_0^2, D_0^3 and D_0^4). Each of the four domains at s=1 are comprised of 4 elementary cells of the array.

4) At scale-level s=0 each domain contains only a single unit-cell which in turn is modeled by its surface impedance [Zs] or admittance matrix [Ys] defined on the modal-basis of this domain.

This process of partitioning the array plane is applicable for the array of any size. In general in case of cells arranged on rectangular lattice, an array containing n cells can be partitioned in $\log_2 n$ scale-levels. For other cell-arrangements the

partitioning technique is still valid only in this case the sub-domains may not be regular-shaped which would affect the choice of modal basis for these domains.

Artificial boundary conditions are considered at the contours of the domains and sub-domains. Physical nature of the problem need to be considered in the choice of boundary conditions. Or alternatively several boundary conditions can be tested and the one with the best convergence results are chosen.

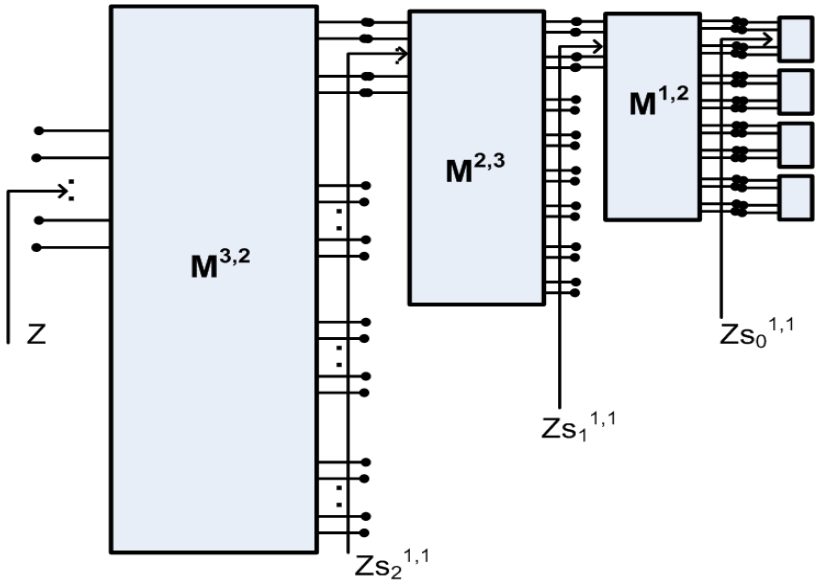

Figure II.26: Calculation of surface impedance of array by cascading Scale-changing networks and surface impedance multipoles.

The computation of all scale-changing networks is mutually independent therefore each multipole can be computed separately on different machines and it is only in the final step the resulting matrices are cascaded to obtain the overall simulation of the entire structure (Fig-II.26).

II.4.4. Numerical results and discussion

Once it has been demonstrated that SCT successfully characterizes mutual coupling between the elements of a small and simple finite array of dipoles the next logical step is to apply the concept to the case of larger arrays and with complex geometries that are traditionally used in modern array applications.

II.4.4.1 Planar Structures under Plane-wave incidence

In this subsection the scattered field results for two types of arrays are presented. The uniform array which is made up of identical metallic patches each of dimensions 13.5mm x 13mm. The non-uniform array is made up of non-identical unit-cells with each unit-cell geometry comprised of a patch loaded with a slot. The length of the patch is 13.5mm whereas the slot-width is 1mm for all cells. But the patch-width (b_1) and slot-length (a_2) are variable from cell to cell. The combination of these parameters will give each unit-cell its unique geometry.

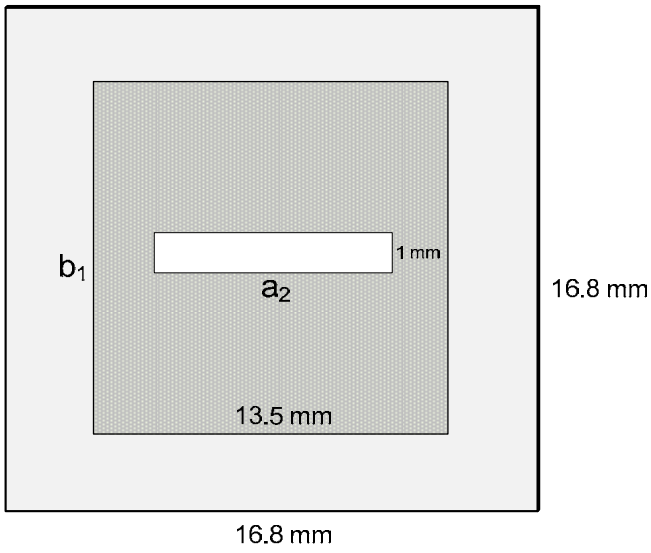

Figure II.27: A unit-cell geometry for non-uniform arrays. Patch-width b_1 and slot-length a_2 is difference for each array element.

First a uniform-array of 64 identical patch-elements arranged in an 8x8 element grid is simulated. Plane-wave normal excitation with vertical E-field polarization (perpendicular to the slot) has been considered. The equivalent surface-current J_{eq} is computed by the procedure detailed in the section II.4.3 on the planar surface of the array. The fields radiated by this current source can be computed by the procedure described in [BalanisAnt Ch:3] by calculating auxiliary Magnetic vector potential (**A**) function.

The radiation pattern results of scattered E-field in the H-plane for the 8x8 uniform patch array is given in Fig-II.28. For the uniform case the pattern is symmetric as expected around 0º elevation. As all the unit-cells are same in this case only a single surface impedance multipole need to be calculated. Four levels of scale-changing networks are used to model the entire array. The structure is simulated with HFSS under plane-wave incidence. Non-normalized results of the reradiated field in H-plane are compared and an excellent agreement is found between the results of the two methods.

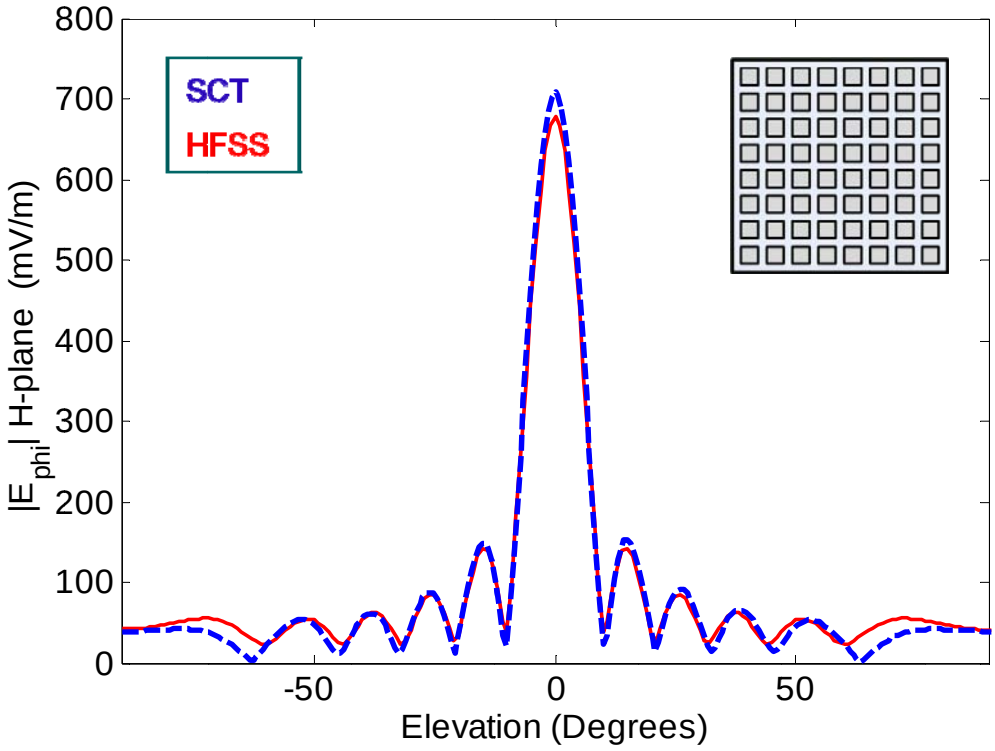

Figure II.28: H-plane radiation pattern of an 8x8 uniform array of identical patches. The patch dimensions are 13.5x13 mm. Unit-cell dimensions 16.8x16.8 mm, at 12.5GHz

In the second case a non-uniform array of 64 elements is analyzed. The array is constructed by varying cell-geometries along horizontal axis whereas the array is kept symmetric along vertical axis. This means that a non-uniform pattern is expected in H-plane when the incident field is polarized in the vertical direction. The radiation pattern results of scattered E-field in the H-plane are given in Fig-II.29. It can be seen that the pattern is not uniform and displaced. Here the SCT results are compared to the results of two other techniques (HFSS and IE3D). It is quite clear that for certain elevation angles the results are more close to one technique and for other angles to

the other. The same is true when the results from the other simulation tools are compared with one another. But overall a general pattern is followed in all three cases and the disagreement at certain angles can be due to the small electrical size of the array.

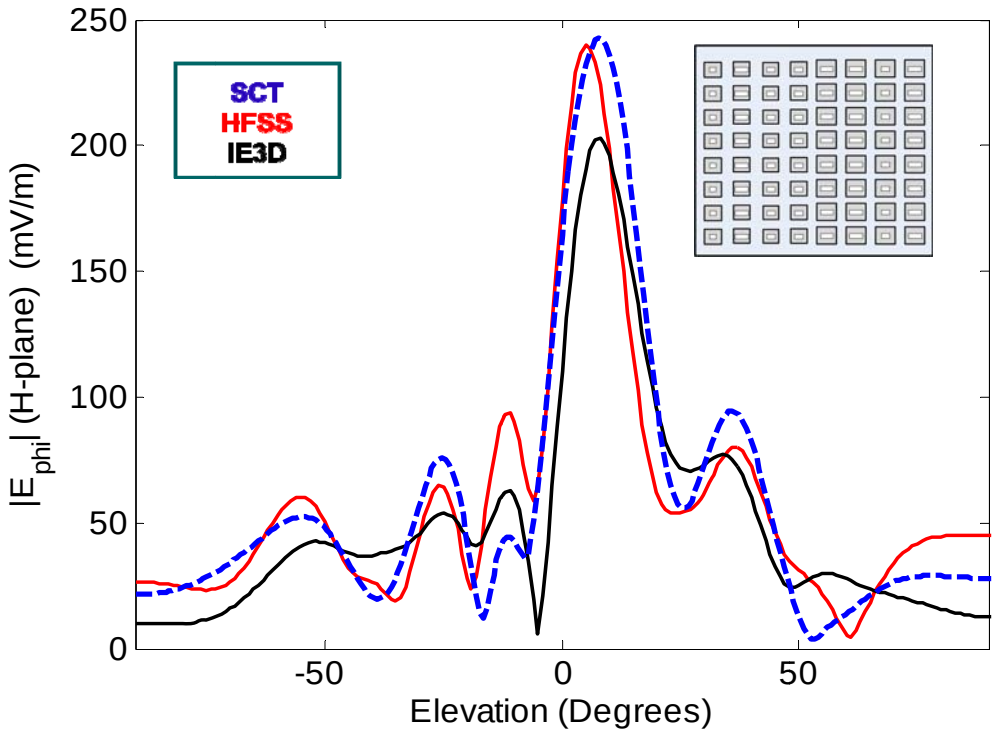

Figure II.29: H-plane radiation pattern of an 8x8 non-uniform array of patch and slots.

Once SCT results have been validated in the case of small sized 2-D arrays it is interesting to apply it to much larger arrays with sizes comparable to real-life designs. Figure II.30 gives the results for a 256 elements uniform patch array arranged in a 16x16 rectangular grid. The scattered field amplitude patterns are given for both H-plane and E-plane. Results from HFSS and IE3D are also presented in the same plots. A very good agreement is observed for the main lobes and first five side-lobes. The results tend to diverge for the elevation angles greater than 50º but the side-lobe levels for these angles are well below 20dB.

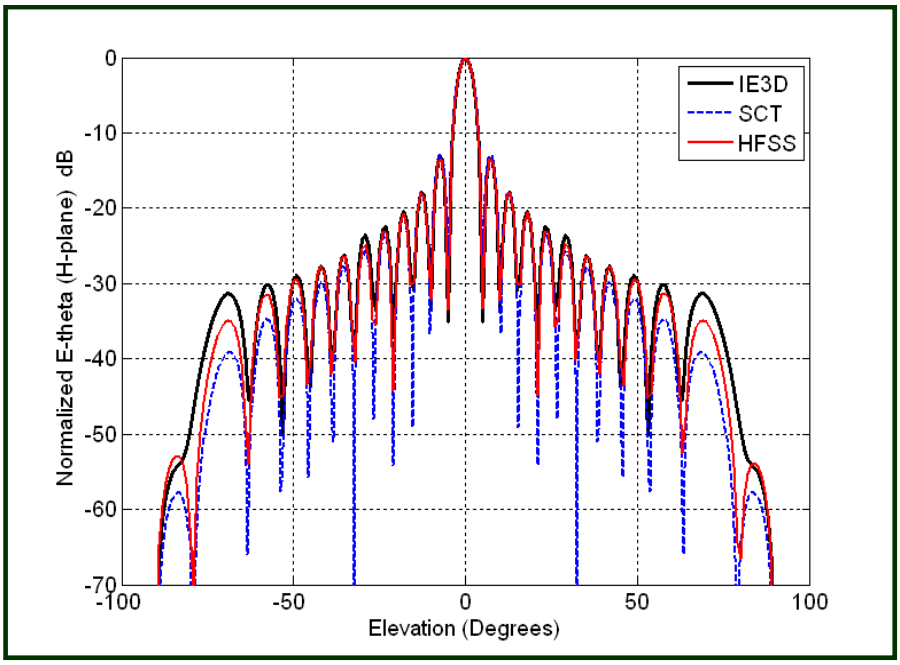

(a)

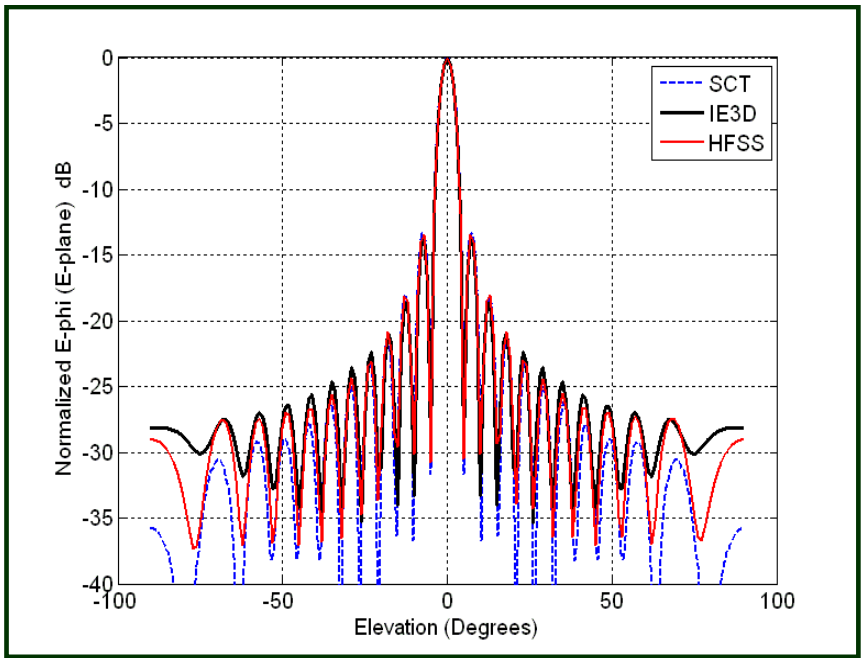

(b)

Figure II.30: Scattering pattern of a 16x16 uniform patch array. The patch dimensions are 13.5x13 mm. (a) H-plane (b) E-plane

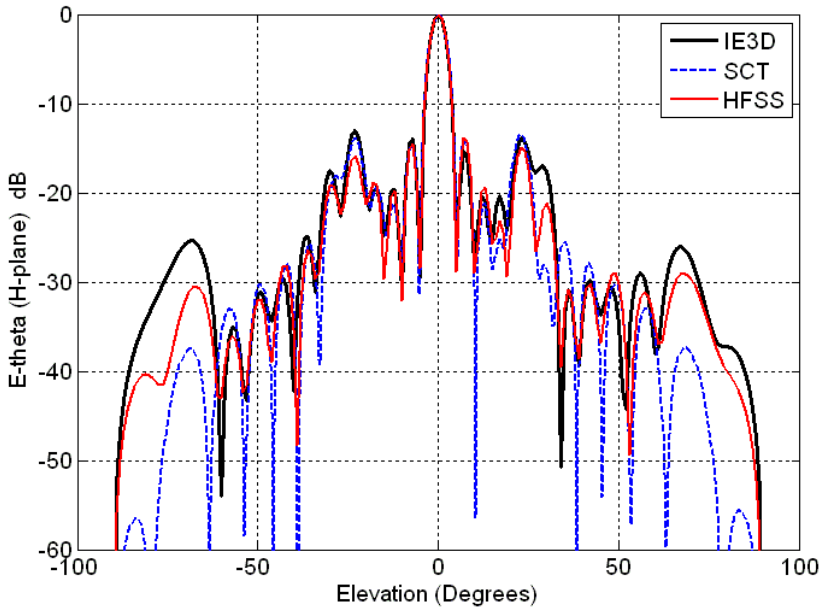

(a)

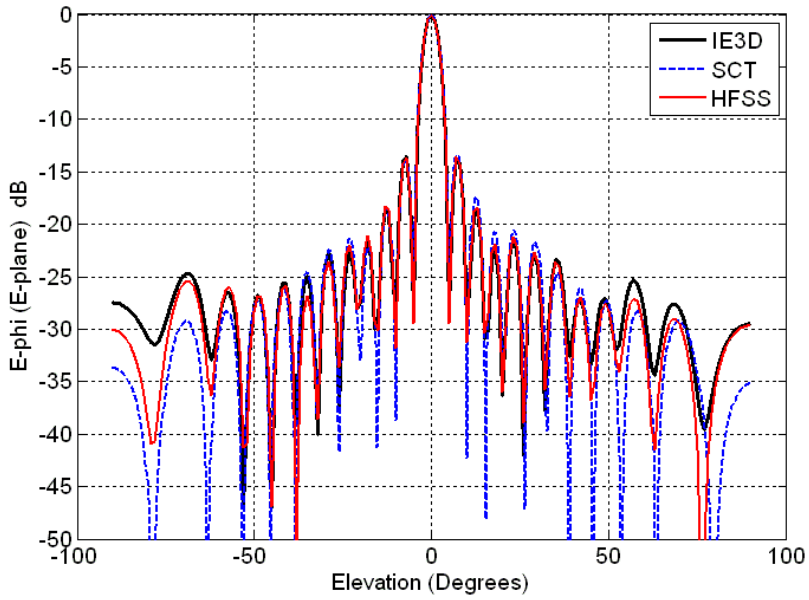

(b)

Figure II.31: Scattering pattern of a 16x16 non-uniform patch array. (a) H-plane (b) E-plane

The results for the 256 element non-uniform array case are given in Fig-II.31. (The individual patch dimensions are taken from ACE array design). This non-uniform patch array is symmetric along vertical axis therefore we have a symmetric pattern in E-plane. The H-plan pattern is non-symmetric as expected. Again a good agreement with the results of other methods is observed for small elevation angles where most of the energy of the radiated field is concentrated.

II.4.4.2 Planar Structures under Horn antenna

In the above sub-section both uniform and non-uniform planar structures were simulated under plane-wave incidence. The plane-wave excitation condition is valid for the applications where the planar structure is used at a far receiving end or when the excitation source is placed very far from the surface of the array. In most practical applications an antenna illumination source is placed in close proximity to the planar array therefore it needs to be simulated along with the planar structure.

As SCT is a 2.5D simulation technique it cannot be directly applied to simulate 3D antenna sources. To incorporate the source in the simulations, SCT can be used in hybrid with other 3-D modeling tools. For example, a source antenna can be modeled using tools like GRASP, FEKO or HFSS and the projection of the radiation fields in the array domain can be used in SCT as an excitation source. Alternatively, some antennas can be modeled analytically e.g. analytical modeling of a pyramidal horn is detailed in Appendix-B.

II.4.4.2.1 Radiation Characteristics of Pyramidal Horn

In Appendix-B a pyramidal horn antenna has been modeled analytically by approximating its behavior by that of a radiating aperture. Taking aperture dimensions equal to that of horn's aperture and a similar aperture field distribution, the far-field radiation patterns of the aperture can approximate the horn's radiation pattern over certain elevation range in the main-beam direction.

The far-field radiation patterns from the aperture field are compared to that of the pyramidal horn radiation patterns to see if the approximation holds. Both H-plane and E-plane radiation patterns are shown in Figure-II.32. It is clear that for the elevation angles between -30º and 30º, the two radiation patterns overlap precisely. Therefore as long as the planar array is placed within this elevation range with respect to source, the behavior of the horn can be modeled accurately. This approximation holds only if the source horn is placed at a distance greater than $2D^2/\lambda$ (where D is the largest horn dimension) which may not always be the case in

practical applications. Nonetheless this approach is presented here to demonstrate how the excitation source can be incorporated with SCT simulations.

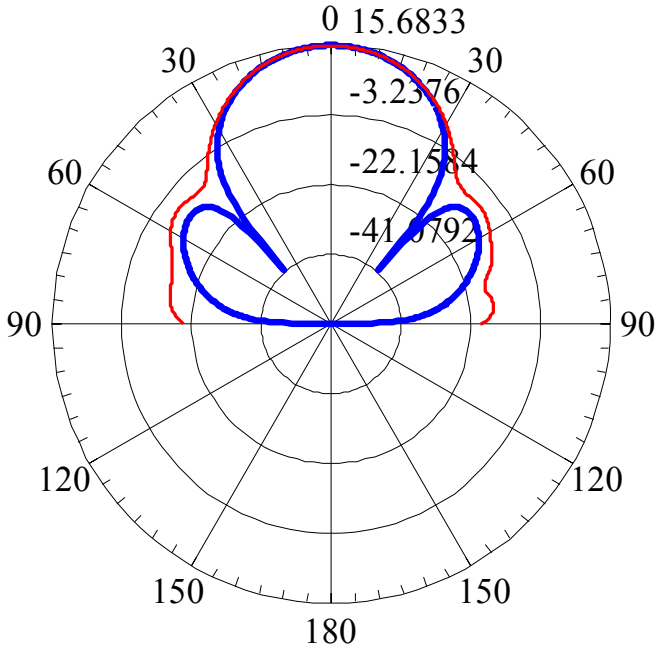

(a)

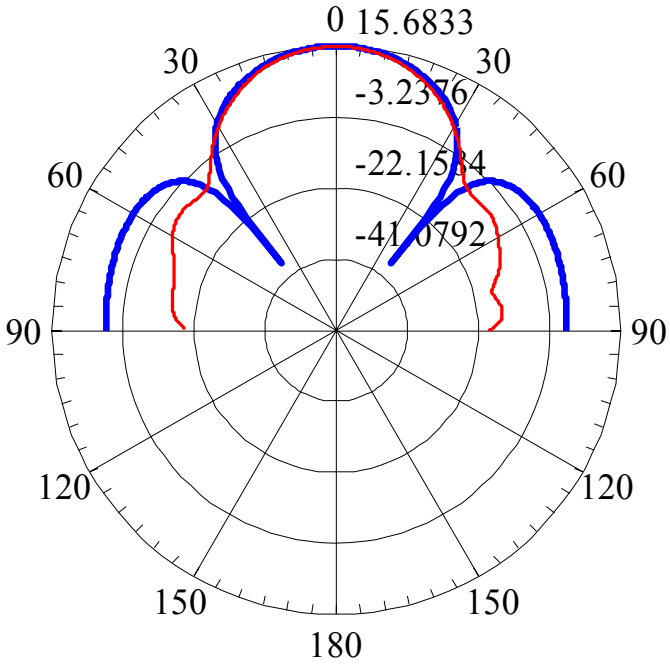

(b)

Figure II.32: Directivity pattern of a pyramidal horn (red) compared to that of Aperture antenna (blue) (a) H-plane (b) E-plane

II.4.4.2.2 Horn Excitation vs Plane-wave Excitation

In this subsection a comparison between the scattering patterns for the two types of excitations i.e. plane-wave excitation and the horn excitation is given. For horn simulations, the antenna is placed along the vertical axis directly above the centre of the planar structure. The distance of the horn can be varied along the vertical axis.

First a simple metal sheet of the dimensions equal to that of an 8x8 array described before has been simulated. The scattering pattern results for the normal plane-wave excitation are shown in blue in Fig-II.33. The horn excitation results when it is positioned at a distance of 66cm and 100 cm from the metal sheet is given in red and black. As expected as the distance of the horn from the sheet is increased its results tend towards the plane-wave results.

Fig-II.34 presents the scattering results from an 8x8 uniform patch array under both plane-wave and horn excitation. Here again we see the similar behavior. At a distance of 100cm the horn field illuminating the array surface is effectively seen as a plane-wave. The horn and plane-wave results are normalized for comparison purposes.

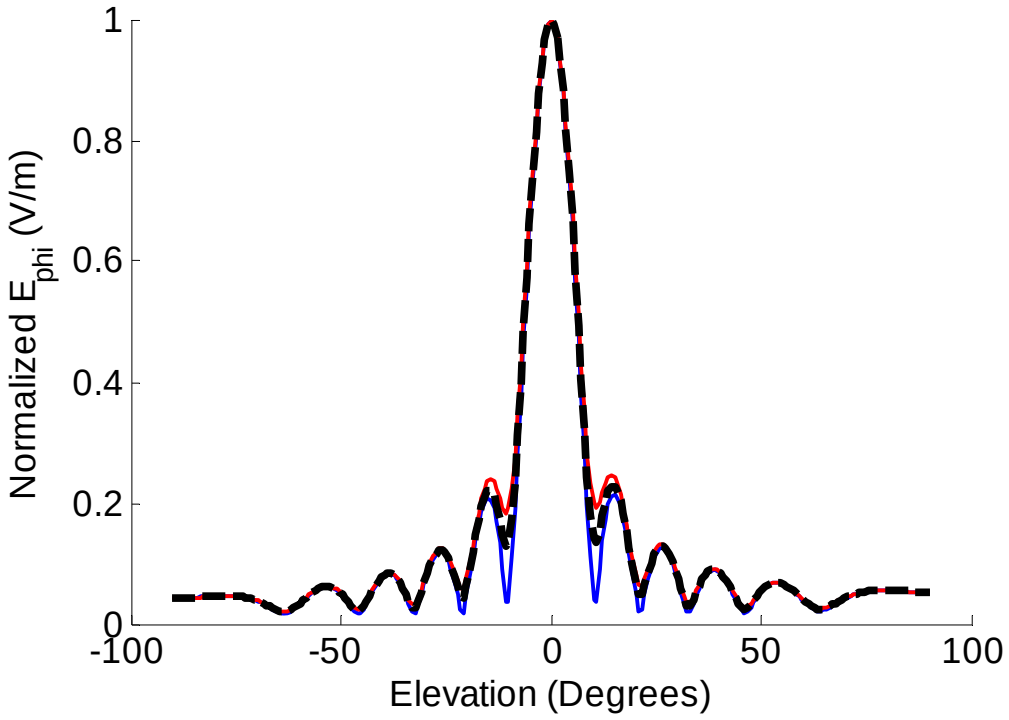

(a)

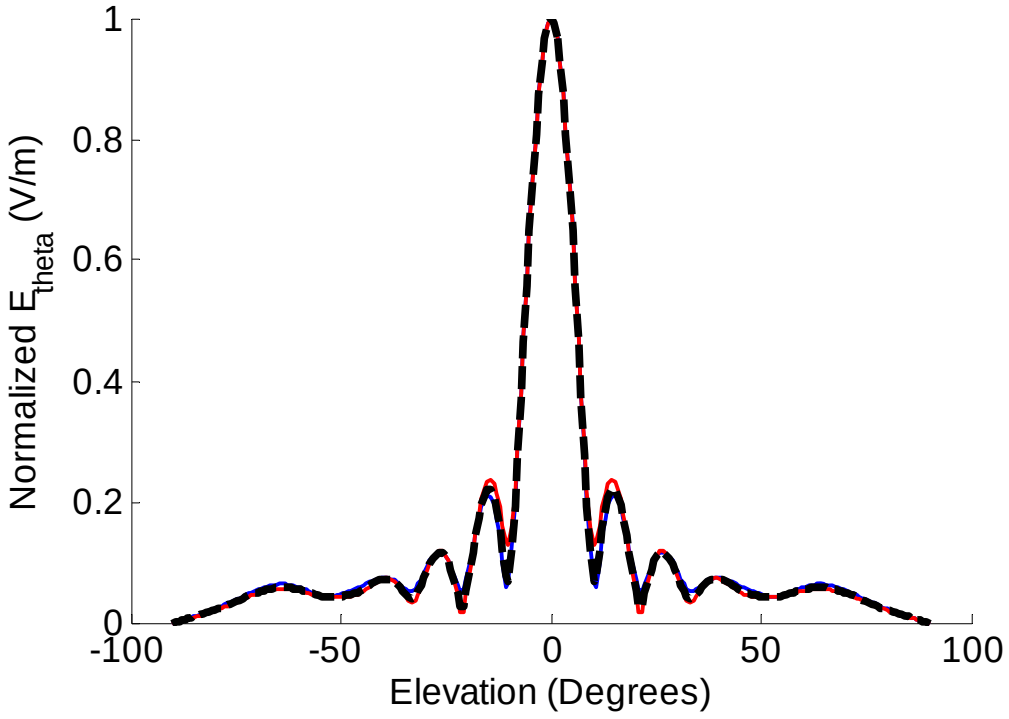

(b)

Figure II.33: Scattering from a metal sheet for different excitations at 12.5GHz. Plane wave (blue) Horn (d=660mm) (red) Horn (d=1000mm) (dotted black) (a) H-plane (b) E-plane

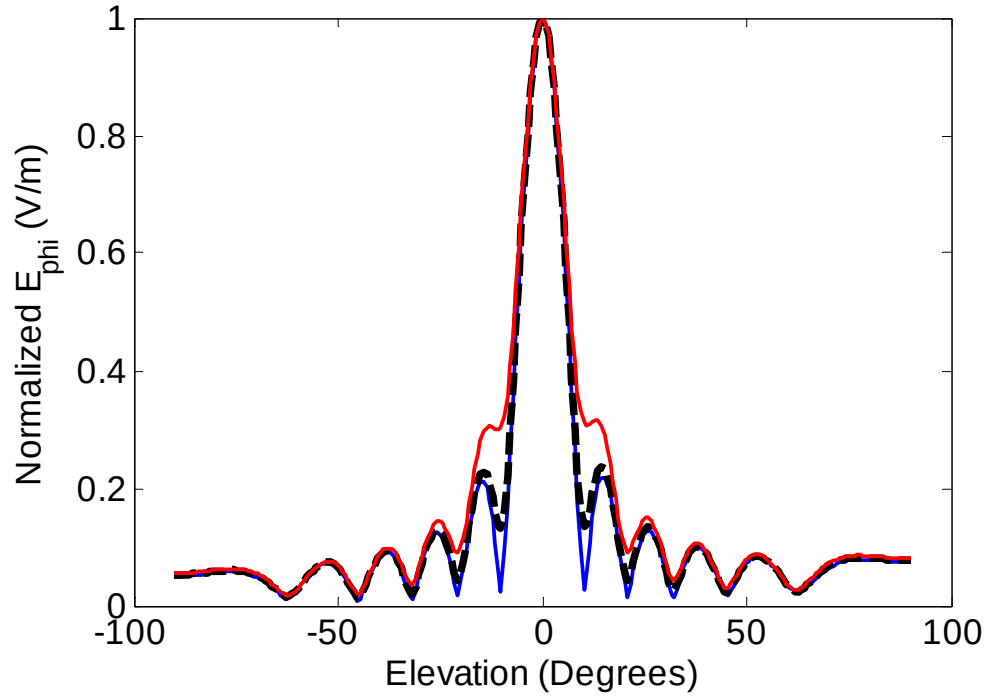

(a)

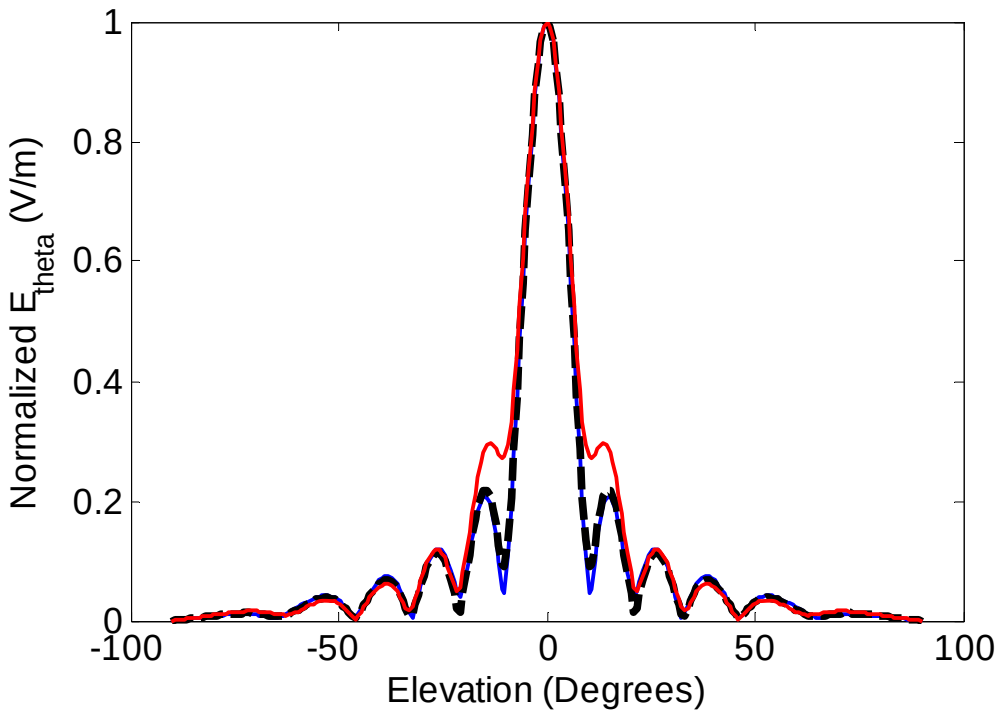

(b)

Figure II.34: Radiation pattern diagrams for a 8x8 uniform patch array at 12.5GHz. Plane wave (blue) Horn (d=400mm) (red) Horn (d=1000mm) (dotted black) (a) H-plane (b) E-plane

II.4.4.2.3 Horn antenna with an offset and angle of inclination

For practical applications the source antenna is not usually placed directly at the top of centre of the planar structure to avoid the masking effect of the source on the backscattered field. Conventionally it is placed at an offset with respect to the center of the planar structure with a certain angle of inclination to center the main lobe of the antenna in the middle of the array (see Fig-B.3).

In this subsection results for several array structures under such an excitation are presented. Same structures are simulated using FEKO (MOM solver) and the results of these simulations are presented in the same plots for the comparison purposes. FEKO was chosen due to its surface meshing capability contrary to HFSS which performs meshing in the whole volume and therefore cannot be used with the memory resources available on a common PC.

A metal sheet of 8x8 array dimensions is simulated and the results of scattered field both in E-plane and H-plane are presented in Fig-II.35. The horn is placed at 66cm above the metal sheet at an offset of 67.2mm from its centre along the vertical axis. It is given an inclination of 6.5º to center its main beam in the middle of the sheet. As the metal sheet is modeled as a perfect conductor we expect to see the specular reflection in the E-plane. The 6.5º displaced main-lobe results in the E-plane demonstrate this effect. In the H-plane the pattern is symmetric around 0º as expected. FEKO results for the similar excitation conditions are represented in green. The non-normalized comparison shows good agreement in the magnitude as well as main-lobe position of the reflected field components. For all FEKO results, rapid jittery variations are present on the radiation pattern curves. One explanation is that this may be due to convergence errors if the meshing step is not fine enough. For all FEKO results presented here λ/10 is taken as mesh-step. A smaller step cannot be taken due to the limitations of memory resources. Nonetheless the FEKO results validate the general form and amplitude of the scattered field patterns.

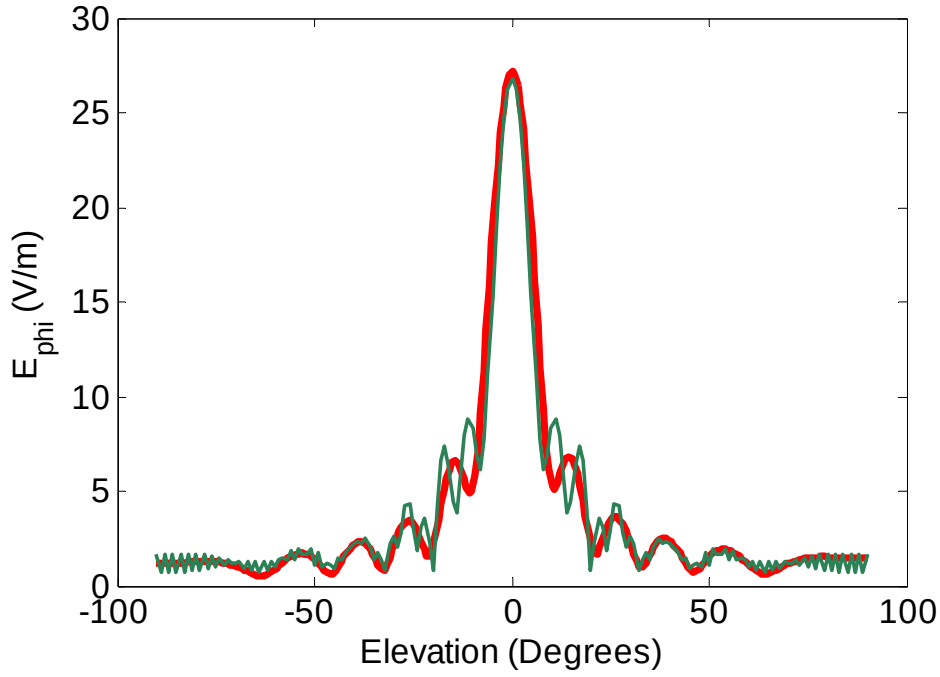

(a)

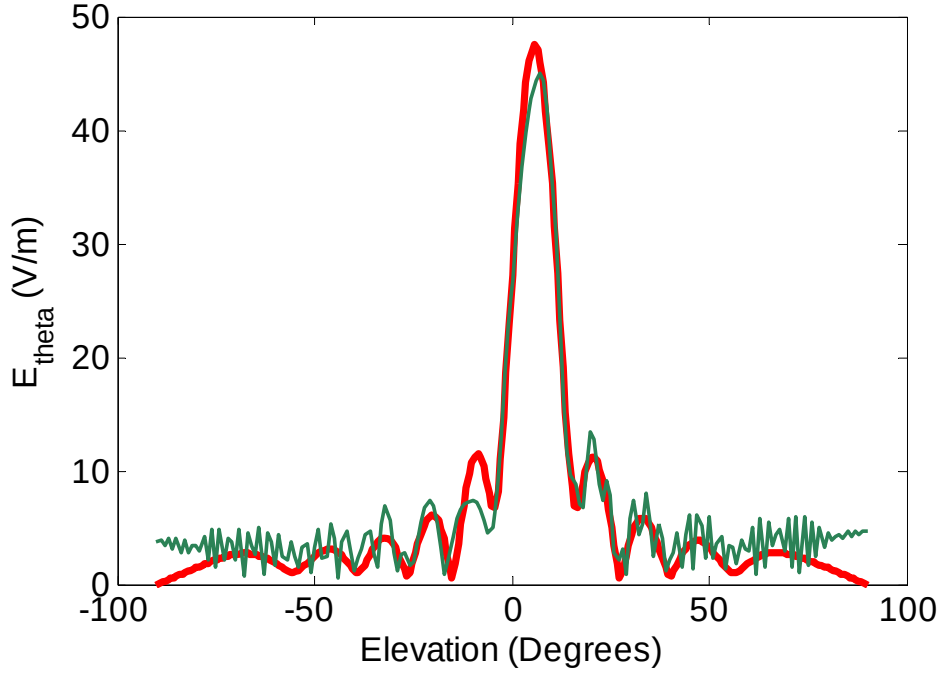

(b)

Figure II.35: Radiation pattern diagrams for a 8x8 metal sheet. FEKO (green) Horn (d=660mm) (red) alpha=6.5º (a) H-plane (b) E-plane

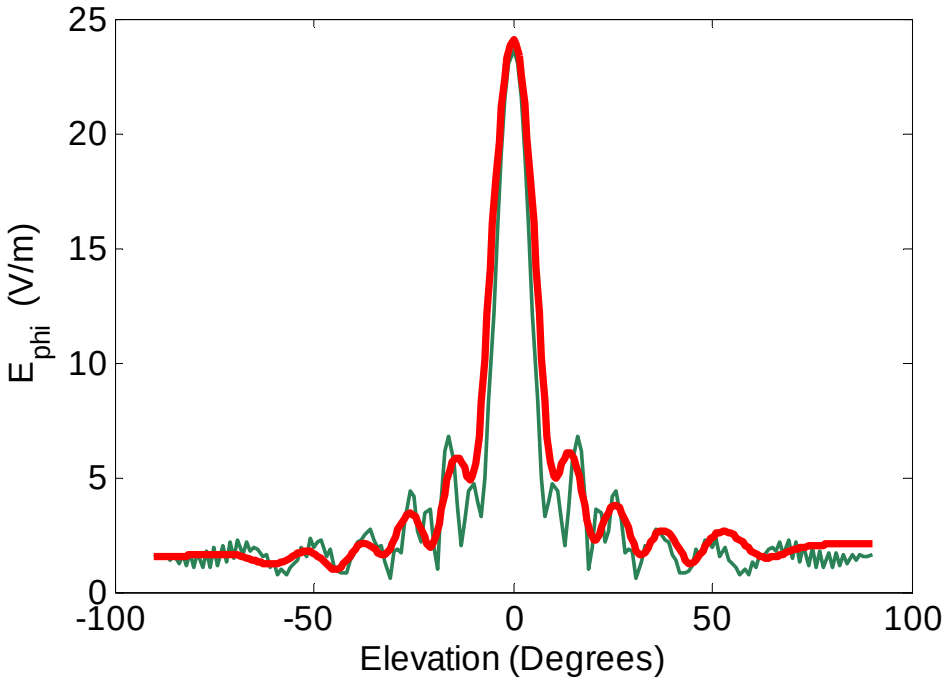

(a)

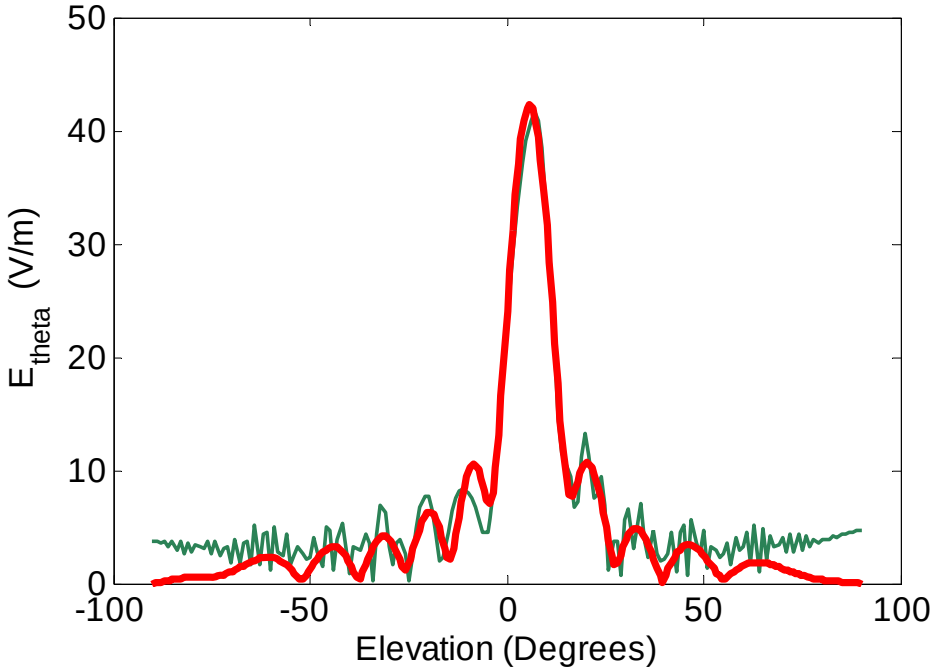

(b)

Figure II.36: Radiation pattern diagrams for a 8x8 uniform patch array. FEKO (green) Horn (d=660mm) (red) alpha=6.5º (a) H-plane (b) E-plane

Fig-II.36 shows the field patterns for an 8x8 uniform patch array under similar excitation conditions as described in the case of metal sheet. The comparison of SCT and FEKO results are presented. Again we see a displaced pattern in E-plane and a symmetric pattern in H-plane as expected.

H-plane radiation pattern results for an 8x8 non-uniform array with the unit-cell geometry comprised of patch loaded with slot is depicted in Fig-II.37. FEKO results in this case have even higher oscillations as compared to the uniform array case. Due to the presence of slots inside the patches usually very fine-scale meshing is required to effectively calculate the rapid field variations around the edges of the slots. The mesh-step used for the FEKO simulations is 2mm (λ/10=2.4mm) in this case it takes around 4 hours to run one complete simulation. The mesh-step cannot be further reduced due to memory constraints. Nonetheless it is very clear that average form of the FEKO pattern closely follows the SCT results in amplitude and form.

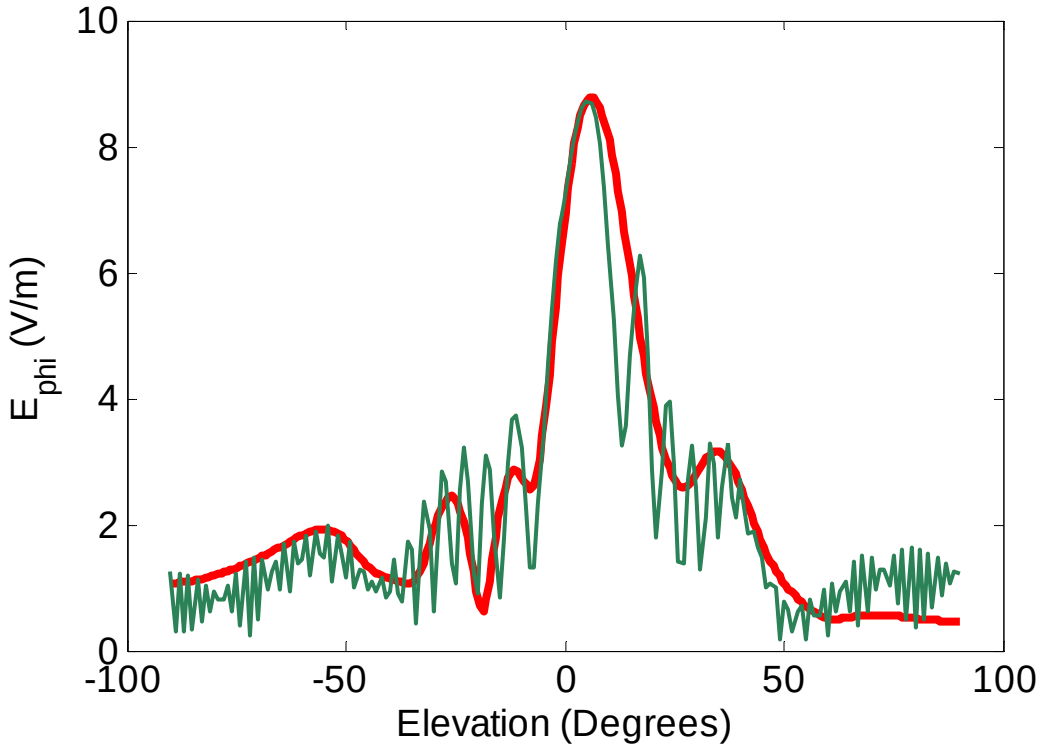

Figure II.37: Scattering pattern of an 8x8 non uniform patch-slot array in H-plane. FEKO (green) Horn (d=660mm) (red) alpha=6.5º

II.4.4.3 SCT Execution Times

The execution times for SCT simulations depend on a number of factors. The scattering patterns are calculated from the equivalent surface current defined in equation II.25. The solution of the fore-mentioned equation requires the computation of three matrices i.e. $[Z_g]$, the projection matrix of free-space Green's functions in the spectral domain, $[V_{in}]$, tangential incident fields on the planar array defined on the array modal-basis and $[Z_s]$ surface impedance matrix characterizing the planar-array structure. The computation of both Z_g and V_{in} does not involve the application of SCT and although they are sensitive to choice of modal-basis in the array-domain at the top-scale, they are not required to be recomputed if any change is made to an individual cell-geometry. Therefore in parametric studies and optimization loops, the computation time of Z_s is the most important.

The computation of Z_s depends on the size of the array as well as the unit- cell geometries. Size of the array will determine the number of scale-changing networks to be computed where as the unit-cell geometry will principally determine the number of active and passive modes required to compute the surface-impedance multipoles. Also if two or more cells have the same geometry, the surface-impedance multipole for each of them needs to be calculated only once.

	CPU Time (sec)
[Zs] complete array	43.06
Zs unit-cell	11.7
SCN (100 active 4000 passive) (1 SCN + 1 cascade)	13
SCN (120 active 4000 passive) (1 SCN + 1 cascade)	11
SCN (200 active 2000 passive) (1 SCN + 1 cascade)	6

Table II.5. [Zs] computation time for 8x8 uniform patch slot array

In the case of a 64 element (8x8) uniform patch-slot array, only one surface-impedance multipole needs to be computed along with three scale-changing networks to compute the surface-impedance for the entire array. The whole process takes around 43 seconds (Table II.5**)**. At scale-level 1 single-unit cell requires 11

seconds to compute; at scale 2 one scale-changing network along with a single cascade (scale-changing network multipole with 4 surface-impedance multipoles) requires 13 seconds and so on. For a uniform array case at each scale-level only a single scale-changing network and a single cascade computation needs to be performed therefore the computation of Z_s in this case is the most efficient.

The execution times in the case of an 8x8 non-uniform patch-slot array comprised of 8 different unit-cell configurations are given in Table II.6. In this case at the scale-level 1, eight surface impedance matrices have to be computed each corresponding to one geometric configuration. At scale-level 2, one scale-changing network has to be computed but 4 cascades need to be performed. The process continues likewise at higher scales. It is clear from these results that SCT make use of redundant nature of the geometry to efficiently characterize the whole structure. It can be deduced from the results of Table II.6 that in the case of an array where all unit-cells differ from one another, the CPU time required to compute Zs of the complete array would be around 1130 seconds.

	CPU Time (sec)
[Zs] complete array	172
Zs unit-cell (8 configs)	135
SCN (100 active 4000 passive) (1 SCN + 4 cascades)	16
SCN (120 active 4000 passive) (1 SCN + 2 cascades)	12
SCN (200 active 2000 passive) (1 SCN + 1 cascade)	6

Table II.6. [Zs] computation time for 8x8 non-uniform patch slot array

II.5. CONCLUSIONS

In this chapter the Scale-changing technique has been applied to characterize several planar structures. In the first part of the chapter, the concept of a scale-changing network to model the mutual coupling between array elements was introduced. It has been shown that SCT can effectively be used to characterize the mutual coupling in the planar arrays. This was demonstrated both in the case of mutual coupling between two half-wave dipole elements as well as between the elements in a planar dipole array. Later the SCT has been applied for modeling non-uniform linear array and it was shown that SCT is manifolds more efficient than other conventional EM modeling tools in case of large arrays.

In the second part of this chapter, SCT has been applied to the problem of electromagnetic scattering from two dimensional non-uniform planar array structures. The scattered field patterns for several types of arrays are calculated under plane-wave and horn-antenna excitation. These results are compared to simulation results from other 3D full-wave analysis tools. Finally the execution times to compute the surface impedances in the case of both uniform and non-uniform arrays are given. It has been shown that SCT effectively reuses the redundancy in a design. Moreover, the highly parallelizable execution capability of scale-changing network makes SCT a promising tool to design, analyze and optimize large complex planar structures, which is not usually convenient to do with the existing techniques.

CONCLUSIONS

A technique based on interconnecting Scale-changing networks has been proposed for the electromagnetic modeling of planar array structures. The problem of electromagnetic scattering from these arrays was addressed and it has been shown that the Scale-changing technique can effectively be used to calculate the field scattering patterns and surface currents. In the course of this thesis SCT has been applied to the scattering problem of several planar arrays and it has been demonstrated that the technique effectively models the mutual interactions between the array elements.

The unique formulation of the Scale-changing Technique avoids the direct computation of structures with high aspect ratios. Thanks to hierarchical domain-decomposition provided by the partitioning process, the complex geometries are broken down into finite number of simpler geometries at distinct scale-levels. Moreover, the scale-changing networks that relate the electromagnetic field at adjacent scales are computed separately, therefore providing an inherent parallelization capability.

This modular nature of the technique can be exploited by distributed processing algorithms to reduce the simulation-time many folds. Similarly the convergence study (finding the appropriate number of active and passive modes at each domain) can be parallelized by running convergence passes as separate processes. It has been demonstrated that for certain planar structures the simulation times can be reduced by 90% by implementing both of above stated approaches [Khalil09].

Domain decomposition not only allows the rapid processing of the overall simulation, it also helps solving the memory problems for simulating large structures. As the complex problem is now partitioned into much smaller problems, the new equations are made up of fewer unknowns and thus can be represented by smaller matrices requiring much less memory resources. In addition this gradual change of dimensions from one scale-level to the next helps to avoid the numerical conditioning errors linked to critical aspect ratios in a structure.

Typically, if N orders of magnitude separate the largest to the smallest dimensions in the structure, the Scale-changing Technique requires the computation of N Scale-changing Networks. In design and optimization processes small modifications in the structure geometry is often required. For example, if modifications in the structure geometry occur at a given scale S, only the SCNs between scale S and S-1 and between S and S+1 need to be recalculated. This gives SCT a huge advantage on classical meshing based techniques which require the recalculation of the overall structure. This built-in modularity makes the scale-changing technique a very powerful optimization and parameterization tool.

Although as a stand-alone method, SCT is applicable only to 2D or 2.5D planar structures, but it can be used in hybrid with other classical methods for 3D applications. The idea is to use the SCT for the planar sub-domains and one of the classical methods e.g. FDTD, FEM or TLM for the volume sub-domains. The interlinking between the methods can be performed using IE formulation by relating tangential electromagnetic fields at the exterior surfaces of the volume sub-domains to the active modes of the planar sub-domains.

Apart from all the positive features SCT has its limitations as well. First of all, there is no simple and automatic convergence criterion for determining the number of active modes in the sub-domains. For the moment the appropriate number of active modes has to be manually determined from the convergence curves. Moreover in certain cases the matrix ill-conditioning problems may lead to numerical convergence issues requiring additional processing e.g. iterative solver methods to resolve them.

Presently, planar structures comprised of simple canonical domains have been treated only. The rectangular domains and sub-domains allow the field description in terms of purely analytical entire-domain trail functions and therefore

save the complex numerical treatment necessary in the case of non-analytical trial functions required to describe the electromagnetic field in non-canonical shaped domains.

Another limitation concerns the introduction of artificial boundary conditions at the boundaries of domains formed by the partitioning process. Normally these boundary conditions are selected taking into account physical nature of the problem that is the behavior of electromagnetic fields in their vicinity. But even a different set of boundary conditions does not seem to affect the accuracy of the solution significantly, only in this case the solution would need a larger number of modes to converge. Similarly introducing artificial boundary conditions around the unit-cell domains of the arrays does not significantly perturb the accuracy of the simulations as shown by the mutual-coupling study.

Concerning the perspectives of this work, it will be highly interesting to design a real-life planar array application e.g. a cassegrain FSS or a reflectarray using Scale-changing Technique and a possible optimization using Grid-computing. The experimental validation of such a case would help to demonstrate the potential of the SCT in the design and analysis of real-life applications.

ANNEX A:

DEFINITIONS OF ORTHOGNAL MODAL-BASIS

ANNEX B:

MODELING OF SOURCE HORN BY RECTANGULAR APERTURE

A.1. INTRODUCTION

This annex gives the expressions of the orthogonal modal-basis for the various kinds of boundary conditions described in Part I of this thesis. Assuming a rectangular domain of dimensions A (along x-axis) and B (along y-axis) with the lower left corner placed at the origin. If this rectangular domain is bounded by any of the following boundary conditions, the transverse electromagnetic field in the domain can be expressed on the orthogonal modes as under.

A.2. ELECTRIC BOUNDARY CONDITIONS

The rectangular domain is bounded by perfect electric boundary conditions on all sides.

$$\vec{f}^{\alpha}(x,y) = \begin{cases} M^{\alpha} \cos\left(\frac{m\pi}{A}x\right) \sin\left(\frac{n\pi}{B}y\right)\vec{x} \\ N^{\alpha} \sin\left(\frac{m\pi}{A}x\right) \cos\left(\frac{n\pi}{B}y\right)\vec{y} \end{cases}$$

$$where\ \ \alpha = TE, TM\ \ A\ and\ B\ are\ the\ dimensions\ of\ the\ array$$

$$M^{\alpha} = \begin{cases} -\frac{n}{B}\frac{\sqrt{2T}}{\sqrt{m^2\left(\frac{B}{A}\right) + n^2\left(\frac{A}{B}\right)}} & (TE) \\ \frac{m}{A}\frac{\sqrt{2T}}{\sqrt{m^2\left(\frac{B}{A}\right) + n^2\left(\frac{A}{B}\right)}} & (TM) \end{cases} \quad N^{\alpha} = \begin{cases} \frac{m}{A}\frac{\sqrt{2T}}{\sqrt{m^2\left(\frac{B}{A}\right) + n^2\left(\frac{A}{B}\right)}} & (TE) \\ \frac{n}{B}\frac{\sqrt{2T}}{\sqrt{m^2\left(\frac{B}{A}\right) + n^2\left(\frac{A}{B}\right)}} & (TM) \end{cases}$$

$$where \begin{cases} T = 1 & m\ or\ n = 0 \\ T = 2 & otherwise \end{cases}$$

A.3. MAGNETIC BOUNDARY CONDITIONS

The rectangular domain is bounded by perfect magnetic boundary conditions on all sides.

$$\vec{f}^{\alpha}(x,y) = \begin{cases} M^{\alpha} \sin\left(\frac{m\pi}{A}x\right) \cos\left(\frac{n\pi}{B}y\right)\vec{x} \\ N^{\alpha} \cos\left(\frac{m\pi}{A}x\right) \sin\left(\frac{n\pi}{B}y\right)\vec{y} \end{cases}$$

$$where\ \ \alpha = TE, TM\ \ A\ and\ B\ are\ the\ dimensions\ of\ the\ array$$

$$M^{\alpha} = \begin{cases} -\dfrac{n}{B}\dfrac{\sqrt{2T}}{\sqrt{m^2\left(\frac{B}{A}\right)+n^2\left(\frac{A}{B}\right)}} & (TE) \\ \dfrac{m}{A}\dfrac{\sqrt{2T}}{\sqrt{m^2\left(\frac{B}{A}\right)+n^2\left(\frac{A}{B}\right)}} & (TM) \end{cases} \quad N^{\alpha} = \begin{cases} \dfrac{m}{A}\dfrac{\sqrt{2T}}{\sqrt{m^2\left(\frac{B}{A}\right)+n^2\left(\frac{A}{B}\right)}} & (TE) \\ \dfrac{n}{B}\dfrac{\sqrt{2T}}{\sqrt{m^2\left(\frac{B}{A}\right)+n^2\left(\frac{A}{B}\right)}} & (TM) \end{cases}$$

$$where\ \begin{cases} T = 1 & m\ or\ n = 0 \\ T = 2 & otherwise \end{cases}$$

A.4. PARALLEL-PLATE WG BOUNDARY CONDITIONS

The rectangular domain is bounded by perfect electric boundary conditions at the top and bottom but perfect magnetic boundary conditions at side walls.

$$\vec{f}^{\alpha}(x,y) = \begin{cases} M^{\alpha}\, sin\left(\dfrac{m\pi}{A}x\right) sin\left(\dfrac{n\pi}{B}y\right)\vec{x} \\ N^{\alpha}\, cos\left(\dfrac{m\pi}{A}x\right) cos\left(\dfrac{n\pi}{B}y\right)\vec{y} \end{cases}$$

$$where\ \ \alpha = TE, TM\ \ A\ and\ B\ are\ the\ dimensions\ of\ the\ array$$

$$M^{\alpha} = \begin{cases} -\dfrac{n}{B}\dfrac{\sqrt{2T}}{\sqrt{m^2\left(\frac{B}{A}\right)+n^2\left(\frac{A}{B}\right)}} & (TE) \\ -\dfrac{m}{A}\dfrac{\sqrt{2T}}{\sqrt{m^2\left(\frac{B}{A}\right)+n^2\left(\frac{A}{B}\right)}} & (TM) \end{cases} \quad N^{\alpha} = \begin{cases} -\dfrac{m}{A}\dfrac{\sqrt{2T}}{\sqrt{m^2\left(\frac{B}{A}\right)+n^2\left(\frac{A}{B}\right)}} & (TE) \\ \dfrac{n}{B}\dfrac{\sqrt{2T}}{\sqrt{m^2\left(\frac{B}{A}\right)+n^2\left(\frac{A}{B}\right)}} & (TM) \end{cases}$$

$$where\ \begin{cases} T = 1 & m\ or\ n = 0 \\ T = 2 & otherwise \end{cases}$$

For m=n=0, we have a TEM mode, so in this case,

$$\vec{\mathrm{f}}^{\mathrm{TEM}}(x,y) = \frac{1}{\sqrt{\mathrm{AB}}}\vec{\mathrm{y}}$$

A.5. PERIODIC BOUNDARY CONDITIONS

The rectangular domain is bounded by periodic boundary conditions (Floquet conditions) at all sides.

$$\vec{f}^{\alpha}(x,y) = \begin{cases} M^{\alpha}\, exp\left(j\frac{2m\pi}{A}x\right) exp\left(j\frac{2n\pi}{B}y\right)\vec{x} \\ N^{\alpha}\, exp\left(j\frac{2m\pi}{A}x\right) exp\left(j\frac{2n\pi}{B}y\right)\vec{y} \end{cases}$$

$$where\ \ \alpha = TE, TM\ \ A\ and\ B\ are\ the\ dimensions\ of\ the\ array$$

$$M^{\alpha} = \begin{cases} j\frac{n}{B}\frac{1}{\sqrt{m^2\left(\frac{B}{A}\right)+n^2\left(\frac{A}{B}\right)}} & (TE) \\ j\frac{m}{A}\frac{1}{\sqrt{m^2\left(\frac{B}{A}\right)+n^2\left(\frac{A}{B}\right)}} & (TM) \end{cases} \quad N^{\alpha} = \begin{cases} -j\frac{m}{A}\frac{1}{\sqrt{m^2\left(\frac{B}{A}\right)+n^2\left(\frac{A}{B}\right)}} & (TE) \\ j\frac{n}{B}\frac{1}{\sqrt{m^2\left(\frac{B}{A}\right)+n^2\left(\frac{A}{B}\right)}} & (TM) \end{cases}$$

For m=n=0, we have two TEM modes, (or modes TE00 and TM00)

$$\vec{\mathrm{f}}^{\mathrm{TEM1}}(x,y) = \frac{1}{\sqrt{\mathrm{AB}}}\vec{x} \qquad \vec{\mathrm{f}}^{\mathrm{TEM2}}(x,y) = \frac{1}{\sqrt{\mathrm{AB}}}\vec{y}$$

B.1. INTRODUCTION

This annex details the mathematical modeling of a pyramidal horn antenna of the dimensions shown in the figure. At the simulation frequency (12.5GHz), the feed-waveguide has only TE_{10} as the propagation mode. Therefore at the aperture of the horn the field distribution can be approximated to that of TE_{10} mode distribution.

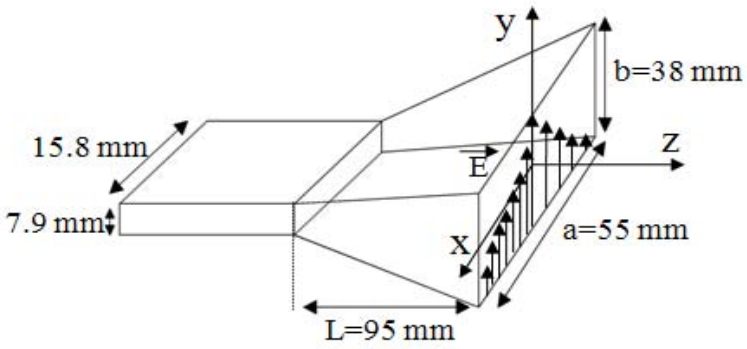

Figure B.1: Dimension of the pyramidal horn along with its aperture field distribution.

B.2. APPROXIMATION BY RADIATING APERTURE

Far-field radiation from a pyramidal horn can be approximated by the radiation from a rectangular aperture inside an infinite ground plane if the aperture field distribution is close to that of the field on the horn aperture. The expressions for the far field radiation pattern for different aperture field distributions can be found analytically [BalanisAnt Ch12].

Consider a rectangular aperture of dimensions **a** and **b** with the electric field distribution given by the following expression.

$$\boldsymbol{E}_a = E_0 \cos\left(\frac{\pi}{a}x'\right)\,\hat{a}_y \quad \begin{Bmatrix} -\frac{a}{2} \le x' \le +\frac{a}{2} \\ -\frac{b}{2} \le y' \le +\frac{b}{2} \end{Bmatrix}$$

The far-field radiated by this field distribution is given in spherical co-ordinates by the following expressions.

$$E_r = H_r = 0$$

$$E_\theta = -\frac{\pi}{2} C \sin\phi \frac{\cos X}{(X^2) - \left(\frac{\pi}{2}\right)^2} \frac{\sin Y}{Y}, \qquad E_\phi = -\frac{\pi}{2} C \cos\theta \cos\phi \frac{\cos X}{(X^2) - \left(\frac{\pi}{2}\right)^2} \frac{\sin Y}{Y}$$

$$H_\theta = -\frac{E_\phi}{\eta} \quad , \quad H_\phi = \frac{E_\theta}{\eta}$$

where

$$X = \frac{ka}{2}\sin\theta\cos\phi \;\; , \;\; Y = \frac{kb}{2}\sin\theta\sin\phi \;\; , \;\; C = j\frac{abkE_0 e^{-jkr}}{2\pi r} \;\; , k = w\sqrt{\mu_0\varepsilon_0} \;\; , \;\; \eta = \sqrt{\frac{\mu_0}{\varepsilon_0}}$$

B.3. TANGENTIAL COMPONENT OF FAR-FIELD ON A PLANAR SURFACE

B.3.1. Horn centered on the planar surface

Following figure shows the tangential component E_{tg} of the radiated field on an incident planar surface located in the x-y plane at a distance z=660mm from the feed horn (in the far-field region).

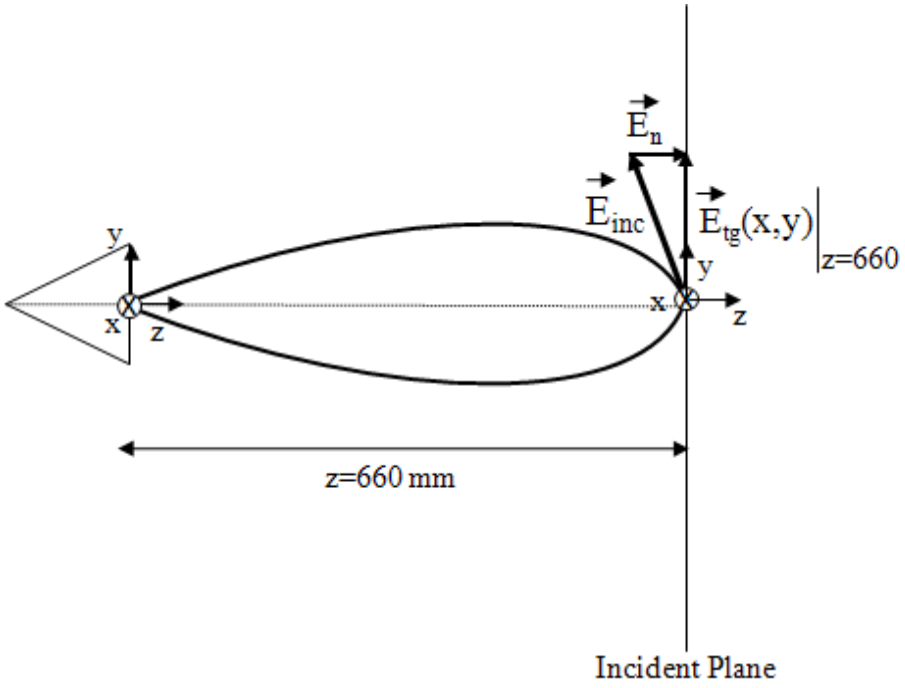

Figure B.2: Computation of the tangential component of the incident field of a horn centered on a planar domain

The incident field can be written in the planar-domain co-ordinate systems as

$$\vec{E}_{inc} = E_x\hat{x} + E_y\hat{y} + E_z\hat{z}$$

Where,

$E_x = E_r \sin\theta \cos\phi + E_\theta \cos\theta \cos\phi - E_\phi \sin\phi$

using far-field expressions from section C.2 in the above equation.

$$E_x = 0 - \frac{\pi}{2} C \sin\phi \frac{\cos X}{(X^2) - \left(\frac{\pi}{2}\right)^2} \frac{\sin Y}{Y} \cos\theta \cos\phi + \frac{\pi}{2} C \cos\theta \cos\phi \frac{\cos X}{(X^2) - \left(\frac{\pi}{2}\right)^2} \frac{\sin Y}{Y} \sin\phi = 0$$

Similarly E_y and E_z can be written as under

$E_y = E_r \sin\theta \sin\phi + E_\theta \cos\theta \sin\phi + E_\phi \cos\phi$

$$E_y = 0 - \frac{\pi}{2} C \sin\phi \frac{\cos X}{(X^2) - \left(\frac{\pi}{2}\right)^2} \frac{\sin Y}{Y} \cos\theta \sin\phi - \frac{\pi}{2} C \cos\theta \cos\phi \frac{\cos X}{(X^2) - \left(\frac{\pi}{2}\right)^2} \frac{\sin Y}{Y} \cos\phi$$

$$E_y = -\frac{\pi}{2} C \frac{\cos X}{(X^2) - \left(\frac{\pi}{2}\right)^2} \frac{\sin Y}{Y} \cos\theta \left[\sin\phi^2 + \cos\phi^2\right]$$

$$E_y = -\frac{\pi}{2} C \frac{\cos X}{(X^2) - \left(\frac{\pi}{2}\right)^2} \frac{\sin Y}{Y} \cos\theta$$

$E_z = E_r \cos\theta - E_\theta \sin\phi$

$$E_z = \frac{\pi}{2} C \sin\phi \frac{\cos X}{(X^2) - \left(\frac{\pi}{2}\right)^2} \frac{\sin Y}{Y} \sin\theta$$

Now $\vec{E}_{inc}$ and $\vec{E}_{tg}$ can be computed from the following equations.

$\vec{E}_{inc} = E_x\hat{x} + E_y\hat{y} + E_z\hat{z} = E_y\hat{y} + E_z\hat{z}$

$\vec{E}_{tg} = \left(E_y\hat{y} + E_z\hat{z}\right).(\hat{x} + \hat{y})$

Since planar surface is normal to the plane of the horn's aperture-plane, the tangential field has only the y-component.

$$\vec{E}_{tg} = E_y\hat{y}$$

B.3.1. Horn with an offset and an inclination angle

In most practical cases the horn antenna is not centered on the reflecting structure but placed at an offset to avoid the masking effect. The horn antenna is

inclined at a certain angle to position its main beam at the centre of the planar structure. In the figure below the horn antenna is displaced a distance 'd' along the y-axis. Angle α represents the orientation of the feed horn with respect to the co-ordinate system of the incident plane. In this case the tangential electric field $\vec{E}_{tg}$ on the planar surface can be found as follows.

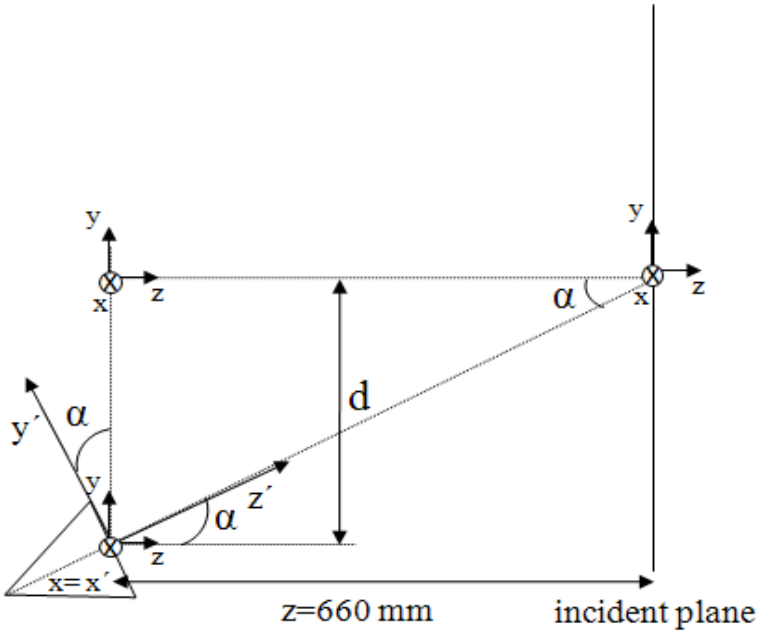

Figure B.3: Computation of the tangential component of the incident field of a horn with an offset and an inclination angle

The new observation point coordinates on the incident plane with respect to the new position and orientation of the feed horn are,

$$x = x'$$

$$y = y' \cos\alpha + z' \sin\alpha$$

$$z = z' \cos\alpha - y' \sin\alpha$$

So the tangential component $\vec{E}_{tg}$ of the field in this case is given by,

$$E_{tg} = \left(E_x\widehat{x'} + E_y\widehat{y'} + E_z\widehat{z'}\right).(\hat{x} + \hat{y})$$

$$E_{tg} = E_x(\widehat{x'}.\hat{x}) + E_y(\widehat{y'}.\hat{y}) + E_z(\widehat{z'}.\hat{y})$$

$$E_{tg} = 0 + E_y \cos\alpha + E_z \sin\alpha$$

$$E_{tg} = E_y \cos\alpha + E_z \sin\alpha$$

Now we plot the magnitude of the tangential component on the planar surface. There are two cases in this respect, first is, in which feed horn is placed normal to

incident plane and the second is in which it is placed with some offset and inclination angle, both of these cases are described below.

B.4. CALCULATION OF $[V_{inc}]$

With parallel-plate boundary conditions as the orthogonal modal basis of the rectangular incident plane, we have

$$[V_{inc}]_{TEM} = \langle \vec{f}, \vec{E}_{tg} \rangle = \iint_{x=0\ y=0}^{A\ B} f_y^*\ E_y\ dx\ dy = \frac{1}{\sqrt{AB}} \iint_{x=0\ y=0}^{A\ B} E_y\ dx\ dy$$

$$[V_{inc}]_{TE,TM} = \langle \vec{f}, \vec{E}_{tg} \rangle = \iint_{x=0\ y=0}^{A\ B} f_y^*\ E_y\ dx\ dy.$$

$$[V_{inc}] = \iint_{x=0\ y=0}^{A\ B} N^{\alpha}\ cos\left(\frac{m\pi}{A}x\right) cos\left(\frac{n\pi}{B}y\right) E_y\ dx\ dy$$

Where $\alpha = \mathrm{TE}, \mathrm{TM}$

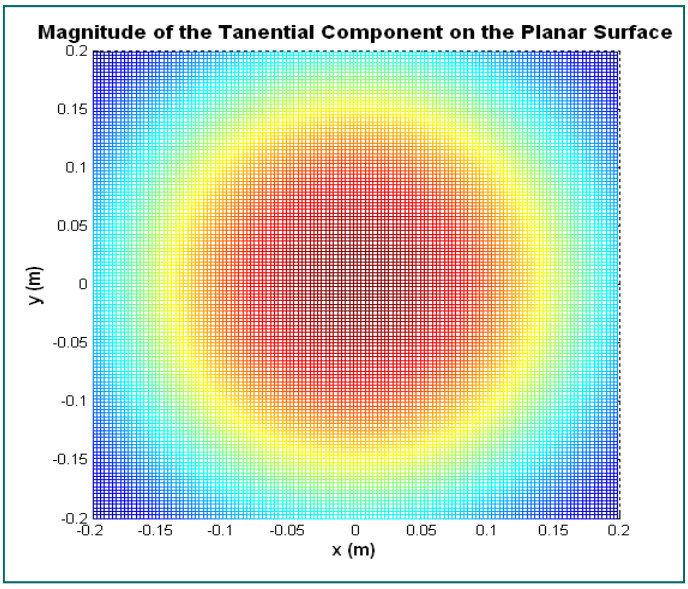

Figure B.4: Tangential field pattern of a horn antenna placed at the center of the planar surface at a distance 'd' from it. d=660mm

B.4.1. Horn centered

By using the analytical expression of E_y in the above equation, we get the following integral. This integral is too complex to resolve analytically and therefore has been solved using numerical integration.

$$[V_{inc}] = \int_{x=0}^{A}\int_{y=0}^{B} \left[N^{\alpha} cos\left(\frac{m\pi}{A}x\right) cos\left(\frac{n\pi}{B}y\right)\right] \left[-\frac{\pi}{2}\left(j\frac{abkE_0 e^{-jk\sqrt{x^2+y^2+z^2}}}{2\pi r}\right)\cos\left(\cos^{-1}\frac{z}{\sqrt{x^2+y^2+z^2}}\right)\right] \left[\frac{\cos\left(\frac{ka}{2}sin\left(\cos^{-1}\frac{z}{\sqrt{x^2+y^2+z^2}}\right)cos\left(\tan^{-1}\frac{y}{x}\right)\right)}{\left(\frac{ka}{2}sin\left(\cos^{-1}\frac{z}{\sqrt{x^2+y^2+z^2}}\right)cos\left(\tan^{-1}\frac{y}{x}\right)\right)^2-\left(\frac{\pi}{2}\right)^2}\right]\left[\frac{\sin\left(\frac{kb}{2}sin\left(\cos^{-1}\frac{z}{\sqrt{x^2+y^2+z^2}}\right)sin\left(\tan^{-1}\frac{y}{x}\right)\right)}{\frac{kb}{2}sin\left(\cos^{-1}\frac{z}{\sqrt{x^2+y^2+z^2}}\right)sin\left(\tan^{-1}\frac{y}{x}\right)}\right] dxdy$$

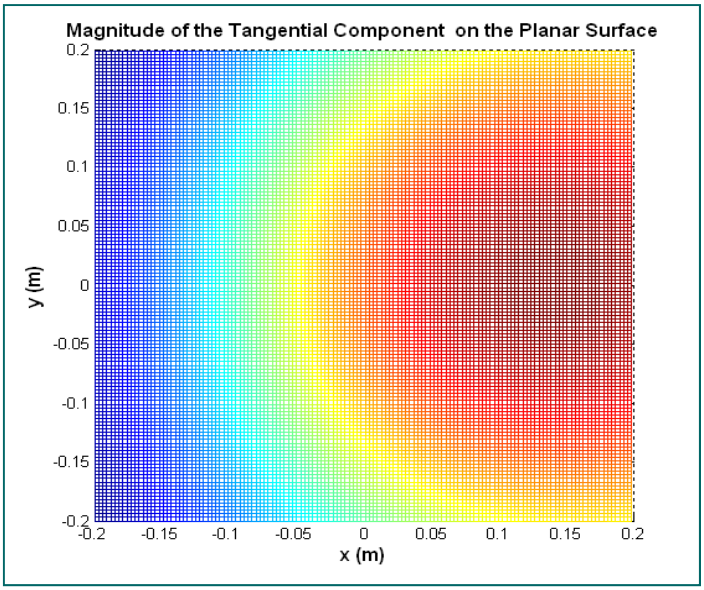

Figure B.5: Tangential field pattern of a horn antenna placed at an offset of 200mm from the center of the surface with an angle of inclination equal to 30º. d=660mm

B.4.2. Horn at an offset with an inclination

If the Horn Antenna is at oblique angle α with an offset of d, then we have to simply replace the coordinates x, y and z in the above equation with x´, y´ and z´ as follows:

$$x' = -z\sin\alpha + (x + d)\cos\alpha$$
$$y' = y$$
$$z' = z\cos\alpha + (x + d)\sin\alpha$$

THESIS SUMMARY

(FRENCH)

Abstract

Les structures planaires de grandes tailles sont de plus en plus utilisées dans les applications des satellites et des radars. Deux grands types de ces structures à savoir les FSS et les Reflectarrays sont particulièrement les plus intéressants dans les domaines de la conception RF. Mais en raison de leur grande taille et de la complexité des cellules élémentaires, l'analyse complète de ces structures nécessite énormément de mémoire et des temps de calcul excessif. Par conséquent, les techniques classiques basées sur maillage linéaire soit ne parviennent pas à simuler de telles structures soit, exiger des ressources non disponibles à un concepteur d'antenne. Une technique appelée « technique par changement d'échelle » tente de résoudre ce problème par partitionnement de la géométrie du réseau par de nombreux domaines imbriqués définis à différents niveaux d'échelle du réseau. Le multi-pôle par changement d'échelle, appelé « Scale changing Network (SCN) », modélise le couplage électromagnétique entre deux échelles successives, en résolvant une formulation intégral des équations de Maxwell par une technique basée sur la méthode des moments. La cascade de ces multi-pôles par changement d'échelle, permet le calcul de la matrice d'impédance de surface de la structure complète qui peut à son tour être utilisées pour calculer la diffraction en champ lointain. Comme le calcul des multi-pôles par changement d'échelle est mutuellement indépendant, les temps d'exécution peuvent être réduits de manière significative en parallélisant le calcul. Par ailleurs, la modification de la géométrie de la structure à une échelle donnée nécessite seulement le calcul de deux multi-pôles par changement d'échelle et ne requiert pas la simulation de toute la structure. Cette caractéristique fait de la SCT un outil de conception et d'optimisation très puissant. Des structures planaires uniformes et non uniformes excité par un cornet ont étés modélisés avec succès, avec des temps de calcul délais intéressants, employant les ressources normales de l'ordinateur.

Introduction générale

La prédiction exacte de la diffraction d'ondes planes par des réseaux de taille finie est d'un grand intérêt pratique dans la conception et l'optimisation des surfaces sélectifs en fréquences (FSS), reflectarrays et transmittarrays. Une analyse (full-wave) complète de ces structures nécessite énormément de ressources de calcul en raison de leur grandes dimensions électriques qui exigeraient la résolution d'un grand nombre d'inconnues. Ainsi, l'absence des outils de conception précis et efficaces pour ces applications limite les ingénieurs à choisir des conceptions simplistes et de faible performance qui ne demandent pas énormément de mémoire et de ressources de traitement.

En outre, la caractérisation des grands réseaux devrait normalement nécessiter une deuxième étape pour l'optimisation et l'ajustement de plusieurs paramètres de conception parce que la procédure initiale de la conception suppose plusieurs approximations, par exemple dans le cas de reflectarrays la conception est généralement basée sur la caractérisation d'une cellule seule sous les conditions d'incidence normales, ce qui n'est pas le cas pratique. Par conséquent, une analyse full-wave de la conception initiale de la structure complète est nécessaire avant la fabrication, a fin de s'assurer que la performance est conforme aux exigences de conception. Une technique d'analyse modulaire qui est capable d'intégrer de petits changements au niveau des cellules individuelles, sans la nécessité de relancer la simulation entière est extrêmement souhaitable à ce stade.

Historiquement plusieurs approches ont été suivies lors de l'analyse des structures planaires de grande taille [Huang07]. Dans le cas des réseaux uniformes, où nous avons la périodicité de la géométrie, une approche infinie est souvent utilisée. En utilisant le théorème de Floquet, l'analyse est en fait réduit à la résolution d'une seule cellule unitaire; ce qui réduit significativement les inconnues et donc le temps de simulation [Pozar84] [Pozar89]. Bien que les conditions aux limites périodiques prennent en compte l'effet de couplage mutuel dans l'environnement périodique, l'approximation ne serait pas valable dans le cas des réseaux où les géométries des

cellules individuelles sont très différentes. En outre il s'agit d'une approximation très mauvaise pour les cellules situées sur les bords des réseaux.

Une technique simple basée sur la méthode des différences finis (FDTD) est proposée pour justement tenir compte des effets de couplage mutuel. Il s'agir d'éclairer une seule cellule du réseau en présence de cellules voisines et le calcul de l'onde réfléchie. Si elle permet d'excitation précise et des conditions aux limites pour chaque cellule dans le réseau, elle n'est pas très pratique pour concevoir des réseaux de grandes en raison de délais d'exécution très longue [Cadoret2005a].

Différentes méthodes conventionnelles ont été testées pour une analyse full-wave des structures périodiques, par exemple la méthode des moments (MOM) utilisés dans le domaine spectral pour les structures multi-échelles [Mittra88] [Wan95], méthode des éléments finis (FEM) [Bardi02] et FDTD [Harms94]. Mais toutes ces méthodes nécessitent des ressources prohibitives pour les cas où l'hypothèse de périodicité locale ne peut pas être appliquée. Une approche immitance dans le domaine spectrale a été utilisée dans l'analyse d'un réseau planaire de dipôles avec la procédure de Galerkin en utilisant l'ensemble des fonctions d'essais en domaine entier (entire-domain trial functions) [Pilz97].

La méthode des moments pour la simulation électromagnétique des réseaux de taille finie nécessite grand temps de calcul et les ressources de mémoire, en particulier lorsque les géométries des patches sont non-canoniques et donc fonctions des base sous-domaine doivent être utilisés. Le problème de mémoire peut être résolu en utilisant diverses techniques itératives (par exemple, méthode de gradient conjugué) [Sarkar82] [Sarkar84] au prix d'une augmentation du temps d'exécution. Une amélioration prometteuse de la MoM, appelée *Characteristic Basis Method of Moments* a été proposée pour réduire le temps d'exécution et le stockage de la mémoire pour des grandes structures [Mittra05] [Lucente06]. Toutefois, la convergence des résultats numériques reste délicate à atteindre systématiquement.

Afin de surmonter les difficultés théoriques et pratiques mentionnés ci-dessus, une formulation monolithe originale pour la modélisation électromagnétique des

structures planaires multi-échelles a été proposée [Aubert09]. La puissance de cette technique appelée *la technique par changement d'échelles (SCT),* provient de la nature modulaire de sa formulation du problème. Au lieu de la modélisation de la surface plane complète, comme un grand problème unique, il est divisé en un ensemble de nombreux petits problèmes dont chacun peut être résolu de manière indépendante en utilisant les techniques variationnelles [Tao91]. La solution de chaque un de ces petits problèmes peut être exprimée sous forme de matrice qui caractérise un multiport appelé « *Scale changing Network* (SCN) ». SCT modélise toute la structure en interconnectant tous les multipoles, où chaque SCN modélise le couplage électromagnétique entre les niveaux de l'échelle adjacents.

La cascade de SCNs permet la simulation électromagnétique globale de toutes sortes de géométries planaires multi-échelle. La simulation électromagnétique globale des structures par la cascade de SCNs a été appliquée avec succès à la conception et la simulation électromagnétique de structures planaires spécifiques tels que les surface sélectives en fréquences multiples [Voyer06], structures auto-similaire (pré-fractale) [Voyer04] [Voyer05], antennes patch [Perret04] [Perret05] et cellule déphaseurs reconfigurables [Perret06] [Perret06a]. L'objectif de ce travail est pour valider SCT dans le cas de diverses géométries de réseau planaire y compris les réseaux FSS, reflectarrays et transmittarrays.

Une autre approche modulaire basée sur du domaine spectral MoM a été utilisée dans le cas des structures périodiques multicouches [Wan95], qui consiste à caractériser chaque couche du réseau par un « *generilzed scattering matrix* (GSM) » puis à analyser la structure complète par une cascade simple de ces GSM. SCT diffère de cette approche, car en cas de SCT le cloisonnement est appliqué à une même surface et donc SCT est applicable à réseaux d'une seule couche. Pour les réseaux multicouches SCT peut être utilisé en l'hybride avec l'approche mentionnée au-dessus pour la modélisation efficace des problèmes électromagnétiques plus complexes, par exemple dans le cas de réseaux des patches empilés des tailles variables [Encinar99-patch] [Encinar01] [Encinar03] et les réseaux couplés par l'ouverture [Robinson99] [Keller00].

Cette thèse est divisée en deux parties. Dans la première partie la théorie derrière la technique par changement d'échelle est présenté dans un contexte général en utilisant l'exemple d'un problème de la discontinuité générique. Plusieurs concepts liés à la technique sont introduits et développés. Comment le problème de discontinuité peut être exprimée en termes de composants de circuit équivalent est démontré [Aubert03]. Le problème est alors formulé en termes d'équations matricielles à partir de ce circuit équivalent, et résolu à l'aide de la technique basée sur le méthode de moments. La deuxième partie de cette section montre l'application de la SCT pour les réseaux réflecteurs périodiques.

Dans la deuxième partie de la thèse, SCT est utilisé a fin de modéliser les réseaux planaires finis et non-uniforme. D'abord, il est démontré que SCT modélise efficacement le couplage électromagnétique entre les cellules voisines d'un réseau. Plus tard, la technique est utilisée pour modéliser des réseaux linéaires non-uniformes des bandes métalliques et des patches. Les résultats de simulation ainsi que les temps de calcules sont comparés à des outils de simulation classiques. Enfin, SCT est appliqué au problème de diffraction en l'espace libre par les réseaux planaires 2D. Les réseaux uniformes et non-uniformes sont simulés sous l'excitation d'onde plane et le cornet. Les résultats de diagrammes de rayonnement sont comparés aux résultats obtenus par d'autres techniques.

Partie 1

Introduction

Actuellement, la méthode la plus utilisée pour calculer les champs de diffraction par des structures planaires est de résoudre des équations de Maxwell dans leur formulation intégrales. Cette approche permet d'exprimer le problème à conditions limitées dans l'espace libre en termes d'une équation intégrale formulées sur la surface plane finie de structure. Cette réduction d'une dimension spatiale rend cette méthode très efficace dans le cas de géométries planes. Pourtant, cette méthode dans sa formulation traditionnelle n'est pas particulièrement adaptée pour les grandes structures planaires multi-échelle avec des motifs métalliques complexes. Les variations rapides et fines dans la géométrie de la structure peuvent provoquer de brusques changements dans le champ électromagnétique exigeant maillage local à une échelle très petites ce qui nécessiterait de un stockage et les ressources de calcul immenses.

Nous proposons de résoudre ce problème en introduisant la description locale des champs dans différentes régions de la surface plane. La procédure peut être résumée par les étapes suivantes:

1. La surface plane est décomposée en plusieurs sous-domaines surfaciques.
2. Le champ électromagnétique est exprimé sur la base modale de chacun de ces sous-domaines bornés par leurs conditions aux limites spécifiques.
3. Les contributions modales sont traitées séparément pour les modes d'ordre inférieur et les modes d'ordre supérieur. Les modes d'ordre supérieur contribuent seulement au niveau local alors que les modes d'ordre inférieurs définissent le couplage avec le domaine à l'échelle supérieure.
4. Le couplage électromagnétique entre deux échelles successives est modélisé par un « *scale changing network* » définie par les modes d'ordre inférieur des deux sous-domaines.
5. Une solution électromagnétique pour la structure entière est obtenue par une cascade simple de ces SCNs.

Conclusion

Dans ce chapitre, nous avons présenté la théorie de la technique par changement d'échelles et certains concepts liés à l'application de cette technique à des structures planaires ont été expliqué. Il a été montré que la SCT est particulièrement adaptée pour les applications qui nécessitent des grandes géométries planaires complexes avec des motifs variant sur une large gamme d'échelle. Le concept de SCN pour modéliser le couplage électromagnétique entre les échelles adjacentes est mis en avant et il est montré que le calcul de ces SCNs est mutuellement indépendant. Cette formulation, par sa nature même est hautement parallélisable, ce qui donne SCT un énorme avantage sur d'autres techniques qui doivent être adaptées pour un traitement distribué.

Dans la seconde moitié de ce chapitre, la SCT est appliquée dans le cas d'une cellule déphaseur sous des conditions périodiques infinité. Les résultats de déphasage introduit à une onde plane en incidence normales et puis obliques sont calculés et comparés à un autre outil de simulation. Le bon accord entre les résultats démontre que SCT est une technique fiable pour la conception et la simulation.

Partie 2

Introduction

Dans la partie précédente, nous avons détaillé la théorie derrière la SCT avec l'exemple d'une cellule déphaseur passif sous les conditions périodiques. Dans cette section, nous allons voir comment cette technique peut être utilisée de manière efficace a fin de modéliser des grands réseaux de géométrie non-uniforme.

Tout d'abord nous allons introduire la notion du multipole de bifurcation qui est essentiellement un multipole de changement d'échelle (SCN), pour modéliser le couplage électromagnétique entre les cellules voisines dans un réseau. Le couplage mutuel entre deux dipôles planaires sera caractérisé par ce SCN et il sera démontré que dans le cas d'un dipôle planaire l'effet de couplage mutuel est correctement pris en compte lors de la modélisation par SCT. Plus tard nous allons utiliser le multipole de bifurcation pour calculer les impédances de surface des réseaux 1D de bandes métalliques et des patches dans un guide d'ondes. Une comparaison des temps de simulation avec celle des techniques conventionnelles sera faite pour souligner l'efficacité du SCT.

Plus tard dans cette partie, le concept du multipole de bifurcation est renforcé a fin de intégrer le couplage mutuel dans les réseaux 2D. Les réseaux planaires non-uniforme de grande taille sont analysés pour le problème de diffraction électromagnétique et un bon accord est obtenu avec les résultats de simulation d'outils de simulation classiques. Puis, ces structures sont analysées en utilisant l'antenne cornet pyramidal comme une source d'excitation. Les résultats sont présentés pour les deux configurations de la source c'est à dire quand le corne est placé à une distance verticale du centre du réseau et quand il est placé avec un offset et un angle d'inclinaison. Une comparaison des temps de simulation est donnée pour chaque cas.

Conclusion

Dans ce chapitre, la technique par changement d'échelles à été appliquée à la caractérisation de plusieurs structures planaires. Dans la première partie du chapitre, la notion d'un multipole de changement d'échelle a été introduite pour modéliser le couplage mutuel entre les éléments des réseaux. Il a été montré que SCT peut effectivement être utilisée pour caractériser le couplage mutuel dans les réseaux planaires. Cela a été démontré à la fois dans le cas de couplage mutuel entre deux dipôle demi-ondes, ainsi que dans le cas des éléments d'un réseau de dipôle. Puis la SCT a été appliquée pour la modélisation d'un réseau linéaire et non-uniforme et il a été montré que la SCT est beaucoup plus efficace que d'autres outils classiques de modélisation dans le cas de grands réseaux

Dans la deuxième partie de ce chapitre, la SCT a été appliquée au problème de la diffusion électromagnétique par les réseaux planaires en 2D. Les diagrammes de champ électrice diffusé par plusieurs types de réseaux sont calculés sous l'excitation d'onde plane et l'antenne cornet. Ces résultats sont comparés aux résultats de la simulation obtenu par autres outils d'analyse full-wave en 3D. À la fin, les temps d'exécution pour calculer les impédances de surface dans le cas des réseaux uniforme et non-uniforme sont présentés. Il a été montré que la SCT réutilise efficacement la redondance d'une conception. En outre, la capacité de l'exécution en parallèle de SCNs rendre SCT un outil prometteur pour concevoir, analyser et optimiser les structures planaires grandes et complexes, ce qui n'est généralement pas facile à faire avec les techniques existantes.

Conclusion générale

Une technique basée sur l'interconnexion des multipole de changement d'échelles a été proposée pour la modélisation électromagnétique de réseaux planaires. Le problème de la diffraction électromagnétique par ces structures a été abordé et il a été montré que la SCT peut être utilisés efficacement pour calculer les diagrammes de rayonnement et les courants de surface. Dans le cadre de cette thèse, la SCT a été appliquée au problème de diffraction électromagnétique dans le cas de plusieurs réseaux planaires et il a été démontré que cette technique modélise de manière efficace les interactions mutuelles entre les éléments du réseau.

La formulation unique de la technique par changement d'échelles permet d'éviter la computation directe des structures avec des rapports de dimensions tres élevé. Grace à la décomposition hiérarchique de domaine de discontinuité par le processus de partitionnement, les géométries complexes sont décomposées en des géométries simples de nombre finis à l'échelle des niveaux distincts. En outre, les multipoles de changement d'échelles qui relient les champs électromagnétiques à des échelles adjacentes sont calculés séparément, offrant ainsi une capacité inhérente à la parallélisation.

Ce caractère modulaire de la technique peut être exploité par des algorithmes de traitement distribué à fin de réduire l'énormément le temps de simulation. De même, l'étude de convergence (en calculant le nombre approprié de modes actifs et passifs à chaque domaine) peut être parallélisée en exécutant les passes de convergence comme des processus séparés. Il a été démontré que pour certaines structures planaires, le temps de simulation peut être réduit de 90% en mettant en œuvre les deux approches indiquées ci-dessus [Khalil09].

La décomposition de domaine permet non seulement le traitement rapide de la simulation globale, elle contribue également à résoudre les problèmes de mémoire pour la simulation de grandes structures. Puisque le problème complexe est

maintenant divisé en plusieurs petits problèmes, les nouvelles équations sont composées de moins de variable inconnues et peuvent donc être représentées par les petites matrices nécessitant moins de ressources de mémoire. De plus, ce changement graduel des dimensions de niveau d'une échelle à l'autre permet d'éviter les erreurs numériques de conditionnement associées à rapport critique de dimensions dans une structure.

En règle générale, si la séparation entre le plus grand et plus petit des dimensions de la structure est à l'ordre de grandeur N, la technique par changement d'échelles nécessite le calcul de N multipoles de changement d'échelles. Dans les processus de la conception et l'optimisation, des petites modifications sont souvent nécessaires dans la géométrie de la structure. Par exemple, si à un moment donné, des modifications dans la géométrie de la structure se produisent à l'échelle S, seuls les SCNs entre l'échelle S et S-1 et entre S et S +1 doivent être recalculés. Cela donne la SCT un énorme avantage par rapport à les techniques classique basées sur le maillage linéaire qui nécessitent au nouveau le calcul de la structure globale. Cette modularité inhérente de la SCT fait de sort que l'on obtient un outil puissant pour l'optimisation et le paramétrage.

Même si la SCT est applicable uniquement pour les structures planaires en 2D ou 2.5D, elle peut être utilisée en hybrides avec d'autres méthodes pour les applications 3D. L'idée est d'utiliser la SCT pour les sous-domaines planaires et l'une des méthodes classiques, par exemple FDTD, FEM ou TLM pour les sous-domaines volumiques. Le rapport entre les méthodes peut être réalisé en utilisant la formulation IE en mettant en relation des champs électromagnétiques tangentiels sur les surfaces extérieures de sous-domaines volumiques par les modes actifs des sous-domaines planaires.

En dehors de toutes les caractéristiques positives la SCT a ses propres limites. Tout d'abord, il n'y a pas de critère simple et automatique de la convergence pour déterminer le nombre de modes actifs dans des sous-domaines. Pour l'instant, le nombre approprié de modes actifs doit être déterminé manuellement à partir des courbes de convergence. En outre, dans certains cas, les problèmes de mauvais

conditionnement des matrices peuvent entraîner des problèmes de convergence numérique nécessitant un traitement supplémentaire.

Actuellement, seulement les structures planaires composées des formes simples canoniques ont été traitées. Les domaines et sous-domaines rectangulaires permettent la description du champ en termes de fonctions d'essaies purement analytique donc évitant les traitements numériques complexes nécessaires dans le cas de fonctions d'essaies non-analytiques nécessaires à la description du champ électromagnétique dans des domaines de formes non-canoniques.

Une autre limitation concerne l'introduction de conditions aux limites artificielles aux bords de domaines formés par le processus de partitionnement. Normalement, ces conditions aux limites sont choisies en tenant compte de la nature physique du problème. Mais même un choix différent de conditions aux limites ne semble pas affecter la précision de la solution de manière significative sauf que dans ce cas, la solution aurait besoin d'un plus grand nombre de modes pour sa converger. De même l'introduction de conditions aux limites artificielles autour des domaines de cellules unitaires de réseaux ne va pas perturber significativement la précision des simulations, comme indiqué par l'étude du couplage mutuelle.

En ce qui concerne les perspectives de ce travail, il sera très intéressant de concevoir, dans les premiers temps, une application réelle de réseau planaire, par exemple une FSS ou un réseau réflecteur Cassegrain en utilisant la technique par changement d'échelles et après une optimisation de cette structure en faisant un calcule sur la grille. La validation expérimentale d'un tel cas, permettrait de démontrer le potentiel du SCT dans la conception et l'analyse des applications réelles.

REFERENCES

[Aubert03] H.Aubert and H.Baudrand : *L'Electromagnétisme par les Schémas Equivalents*, Cepaduès éditions, 2003.

[Aubert09] H. Aubert "The Concept of Scale-Changing Network in the Global Electromagnetic Simulation of Complex Structures," *Progress In Electromagnetics Research B*, vol. 16, page 127-154, 2009.

[BalanisAnt] C. A. Balanis: *Antenna Theory: Analysis and Design*, Wiley Editions

[BalanisTh] C. A. Balanis: *Theory of Electromagnetics*, Wiley Editions

[Bardi02] I. Bardi, R. Remski, D. Perry, and Z. Cendes, "Plane wave scattering from frequency selective surfaces by finite element method", *IEEE Transactions Magazine.* Vol. 38 no. 2, pp. 641- 644, March 2002.

[Bozzi03] M. Bozzi and L. Perregrini, "Analysis of multilayered printed frequency selective surfaces by the MoM/BI-RME method," *IEEE Transactions on Antennas and Propagation*, Vol. 51, pp. 2830-2836, October 2003.

[Bose80] N.K.Bose: "Two-Dimensional Matrix Padé Approximants: Existence, Non-uniqueness and Recursive Computation", *IEEE Transactions on Automatic Control*, June 1980, volume 25, No. 3.

[Brezinski94] Brezinski C. and Van Iseghem J.: *Padé Approximants in Handbook of Numerical Analysis*, P.G. Ciarlet and J.L.Lions Editors, 1994, volume III part 1, pp. 47-223.

[Cadoret05] D.Cadoret, A.Laisne, R.Gillard, H.Legay, "Design and measurement of new reflectarray antenna using microstrip patches loaded with slot", *Electronic Letters*, Vol. 41, No.11, May 2005, pp. 623-624.

[Cadoret05a] D.Cadoret, A.Laisne, M.Milon, R.Gillard, H.Legay, " FDTD analysis of reflectarray radiating cells, "*IEEE/ACES International Conference on Wireless Communications and Applied Computational Electromagnetics*, pp. 853-856, April 2005.

[Collin91] Robert E.Collin: *Field Theory of Guided Waves*, IEEE Press, Second Edition, 1991.

[Encinar99] J. A. Encinar, "Printed circuit technology multilayer planar reflector and method for the design thereof", *European Patent EP 1120856*, June 1999.

[Encinar01] J. A. Encinar , " Design of two - layer printed reflectarrays using patches of variable size , " *IEEE Transactions on Antennas and Propagation*, Vol. 49 , No. 10 , pp. 1403 – 14010 , October 2001

[Encinar03] J. A. Encinar and J. A. Zornoza , " Broadband design of three - layer printed reflectarrays , " *IEEE Transactions on Antennas and Propagation*, Vol. 51, No. 7 , pp. 1662 – 1664 , July 2003

[Gianvittorio04] J.P.Gianvittorio, Y.Rahmat-Samii, "Reconfigurable reflectarray with variable height patch elements: design and fabrication", *IEEE Antennas and Wireless Propagation Symposium*, Vol.2, Pages 1800-1803, June 2004.

[Harrington96] R.F.Harrington: *Field Computation by Moment Methods*, IEEE Press, 1996.

[**Harrington61**] R.F.Harrington: *Time-Harmonic Electromagnetic Fields*, New York McGraw-Hill, 1961.

[Harms94] P. Harms, R. Mittra and K. Wae, "Implementation of periodic boundary condition infinite-difference time-domain algorithm for FSS structures", *IEEE Transactions on Antennas and Propagation*, Vol. 42, pp. 1317-1324, September 1994.

[Huang91] J. Huang, "Microstrip reflectarray", *Antennas and Propagation Society International Symposium*, APS Digest, pp. 612-615, 1991.

[Huang07] J. Huang and J. A. Encinar: *Reflectarray Antennas*, IEEE Press, 2007.

[Khalil09] F. Khalil, C.Barrios-Hernandez, A.Rashid, H.Aubert et al. "Parallelization of the Scale Changing Technique in Grid Computing environment for the Electromagnetic Simulation of Multi-scale Structures", *Wiley International Journal of Numerical Modeling*. (Accepted)

[Keller00] M. G. Keller , M. Cuhaci , J. Shaker , and A. Petosa , A. Ittipiboon , and Y. M. M. Antar ," Investigations Novel Reflectarray Configurations, "*Symposium on Antenna Technology and Applied Electromagnetics* , pp. 299 – 302 , 2000.

[Lucente06] E. Lucente, A. Monorchio, R. Mittra, Generation of Characteristic Basis Functions by using Sparse MoM Impedance Matrix to Construct the Solution of Large Scattering and Radiation Problems," *IEEE Antennas and Propagation Society International Symposium 2006*, Page(s):4091 – 4094.

[Lee71] S.W. Lee, W.R. Jones, J. J. Campbell, "Convergence of numerical solutions of iris-type discontinuity problems", *IEEE Transactions on Microwave Theory and Techniques*, vol. MTT-19, No. 6, June 1971, pp.528-536.

[Mittra05] Mittra, R.; Ji-Fu Ma; Lucente, E.; Monorhio, A.;, **"**CBMOM – an iteration free MoM approach for solving large multiscale EM radiation and scattering problems**,** " *IEEE Antennas and Propagation Society International Symposium*, Volume 2B, 3-8 July 2005 Pages:2-5

[Mittra88] R.Mittra, C.H.Chan, T.Cwik: "Techniques for analyzing frequency selective surfaces a review ", *Proceedings of IEEE* , Vol. 76, No. 12, pp. 1593-1615, December 1988.

[Milon07] Milon, M-A., Cadoret, D., Gillard, R., Legay, H., “Surrounded-element approach for the simulation of reflectarray radiating cells,” *IET Microwaves Antennas and Propagation*, Vol. 1, No. 2, 289–293, 2007.

[Nadarassin95] M.Nadarassin, H.Aubert, H.Baudrand: "Analysis of Planar Structures by an Integral Multi-Scale Approach", *Microwave Symposium Digest IEEE MTT-S International*, Mai 1995, volume 2, pp. 653 – 656.

[Nadarassin95a] M.Nadarassin, H.Aubert and H.Baudrand: "Analysis of Planar Structures by an Integral Approach using Entire Domain Trial Functions", *IEEE Transactions on Microwave Theory and Technique,* October 1995, volume 43 No. 10, pp. 2492-2495.

[Nayanthara87] Nayanthara K., Rao S. M. and Sarkar T. K.: "Analysis of Two-Dimensional Conducting and Dielectric Bodies Utilizing the Conjugate Gradient Method", *IEEE Transactions on Antennas and Propagation*, April 1987, volume 35 No. 4, pp. 451-453.

[Perret04] E.Perret, H.Aubert, “A Multi-scale Technique for the Electromagnetic Modeling of Active Antennas”, *IEEE AP-S International Symposium on Antennas Propagation* and *USNC/URSI National Radio Science Meeting*, Monterey, California, USA, June 20-25, 2004, Conference proceedings volume 4, pp. 3923-3926.

[Perret05] E.Perret, H.Aubert, “Scale-changing technique for the computation of the input impedance of active patch antennas”, *IEEE Antennas and Wireless Propagation Letters*, Vol.4, 2005, Pages: 326-328.

[Perret06] E.Perret, H.Aubert, H.Legay, “Scale-changing technique for the electromagnetic modeling of MEMS-controlled planar phase-shifters”, *IEEE Transactions on Microwave Theory and Techniques*, Vol.54, No.9, September 2006, Pages: 3594-3601.

[Perret06a] E.Perret, N Raveu, H.Aubert, H.Legay, “Scale Changing Technique for MEMS-controlled phase-shifters,” *European Microwave Week* (EuMW’06), Manchester, United Kingdom, 10-15 September 2006, Conference proceedings pp.866-869.

[PerretTh] E.Perret : "Application de l’approche par changements d’échelle aux circuits planaires hyperfréquences", *thèse laboratoire d’électronique de l’ENSEEIHT*, 2005.

[Pozar84] D.M.Pozar, D.H.Schaubert, “Analysis of an infinite array of rectangular microstrip patches with idealized probe feeds”, *IEEE Transactions on Antennas and Propagation*, Vol.32, pp. 1101-1107, October 1984.

[Pozar89] D. M. Pozar, “Analysis of an infinite phased array of aperture coupled microstrip patches”, *IEEE Transactions on Antennas and Propagation*, Vol. 37, pp. 418-425, April 1989.

[Pozar93] D. M. Pozar and T. A. Metzler , " Analysis of a reflectarray antenna using microstrip patches of variable size ", *Electronics Letters* Vol. 29, No. 8, pp. 657 – 658, April 1993.

[Pilz97] D.Pilz and W.Menzel, "Full wave analysis of a planar reflector antenna", *Asia Pacific Microwave Conference*, December 1997.

[Rashid08] A.Rashid, H.Aubert, N.Raveu, H.Legay "Modeling of Infinite Passive Planar Structures using Scale-Changing Technique". *IEEE Antennas and Wireless Propagation Society International Symposium (APS 2008)*, San Diego, July 5-11, 2008.

[Rashid09] A.Rashid, H,Aubert, H,legay " Modeling of finite and non-uniform patch arrays using scale-changing technique", *IEEE Antennas and Wireless Propagation Society International Symposium (APS 2009),* Charleston, USA.

[Rashid10] A.Rashid, H.Aubert, "Modeling of Electromagnetic Coupling in Finite Arrays Using Scale-changing Technique", *Progress In Electromagnetics Research Symposium (PIERS),* 5-8 July 2010, Cambridge, USA.

[Raveu07] N.Raveu, G.Prigent, H.Aubert, P.Pons, H.Legay, "Scale Changing Technique Design and Optimization Tool for Active Reflect-arrays Cell," *37th European Microwave Conference* (EuMC'07), Munich, Germany, October 2007, Conference proceedings pp.736-739.

[Robinson99] A. W. Robinson , M. E. Bialkowski , and H. J. Song , " An X - band passive reflect – array using dual - feed aperture - coupled patch antennas, " *Asia Pacific Microwave Conference* , pp. 906 – 909 , December 1999.

[Sarkar84] T.K.Sarkar S.M.Rao: "The Application of Conjugate Gradient Method for the Solution of Electromagnetic Scattering from Arbitrarily Oriented Wire Antennas", *IEEE Transactions on Antennas and Propagation*, April 1984, volume 32, No. 4, pp. 398-403.

[Sarkar82] T.K.Sarkar S.M.Rao: "An Iterative Method for Solving Electrostatic Problems", *IEEE Transactions on Antennas and Propagation*, July 1982, volume 30 No. 4, pp. 611-616.

[Tao91] J.W. Tao, H.Baudrand, "Multimodal variational analysis of uniaxial waveguide discontinuities," *IEEE Transactions on Microwave Theory and Techniques*, Vol. 39, Issue 3, pp. 506 – 516, March 1991.

[Targonski94] S. D. Targonski and D. M. Pozar "Analysis and design of a microstrip reflectarray using patches of variable size", *Antennas and Propagation Society International Symposium*, 1994. AP - S. Digest, pp. 1820 – 1823, June 1994.

[Tchikaya09] E.B.Tchikaya, A.Rashid, F.Khalil, H.Aubert, H.Legay, N.Fonseca, "Multi-scale Approach for the Electromagnetic modeling of metallic FSS Grids of Finite Thickness with Non-uniform Cells", *Asia Pacific Microwave Conference (APMC),* 7-10 December 2009, Singapore.

[Vardaxoglou97] J. C. Vardaxoglou: *Frequency Selective Surfaces: Analysis and Design*, Research Studies Press LTD, 1997.

[Voyer06] D.Voyer, H.Aubert, J.David, “Scale-changing technique for the electromagnetic modeling of planar self-similar structures”, *IEEE Transactions on Antennas and Propagation*, Vol.54, No.10, October 2006, Pages: 2783-2789.

[Voyer04] D.Voyer, H.Aubert, J.David, “Radar Cross Section of discrete self-similar objects using a recursive electromagnetic analysis”, *IEEE AP-S International Symposium and USNC/URSI National Radio Science Meeting, Monterey*, California, USA, 20-26 June 2004, Conference Proceedings volume 4, pp. 4260-4263.

[Voyer05] D.Voyer, H.Aubert, J.David, “Radar Cross Section of Self-similar Targets,” *Electronics Letters*, vol. 41, No. 4, pp. 215 – 217, February 17, 2005.

[VoyerTh] D.Voyer: "Modélisation électromagnétique par changement d’échelle appliquée aux structures fractales planaires", *thèse laboratoire d’électronique de l’ENSEEIHT*, 2005.

[Wan95] C. Wan and J. A. Encinar, “Efficient computation of Generalized Scattering Matrix for analyzing multilayered periodic structures”, *IEEE Transactions on Antennas and Propagation*, Vol. 43, pp. 1233-1242, October 1995.

PUBLICATIONS

International Publications

A.Rashid, H.Aubert "Electromagnetic Modeling of a Finite Array of Thin Metallic Strips using Scale-Changing Technique (SCT)", *Wiley International journal of RF and Microwave Computer-Aided Engineering.* (Under Review)

F. Khalil, C.Barrios-Hernandez, A.Rashid, H.Aubert et al. "Parallelization of the Scale Changing Technique in Grid Computing environment for the Electromagnetic Simulation of Multi-scale Structures", *Wiley International Journal of Numerical Modeling*. (Accepted)

A.Rashid, H.Aubert "Full-wave analysis of large, complex planar arrays using Scale-Changing Technique (SCT)". (Under Preparation)

International Communications

A.Rashid, H.Aubert, N.Raveu, H.Legay, "Modeling of Infinite Passive Planar Structures using Scale-Changing Technique". *IEEE Antennas and Wireless Propagation Society International Symposium (APS 2008),* San Diego, July 5-11, 2008.

A.Rashid, H,Aubert, H,legay " Modeling of finite and non-uniform patch arrays using scale-changing technique", *IEEE Antennas and Wireless Propagation Society International Symposium (APS 2009),* Charleston, USA.

A.Rashid, H,Aubert, H,legay " Scale-Changing Technique for the numerical modeling of large finite non-uniform array structures", *Progress In Electromagnetics Research Symposium (PIERS),* 18-21 August 2009, Moscow, Russia.

A.Rashid, H.Aubert, "Modeling of Electromagnetic Coupling in Finite Arrays Using Scale-changing Technique", *Progress In Electromagnetics Research Symposium (PIERS),* 5-8 July 2010, Cambridge, USA.

F. Khalil, A.Rashid, H.Aubert, F.Coccetti, R.Plana, C.Barrios-Hernandez, "Application of Scale Changing Technique - Grid Computing to the Electromagnetic Simulation of Reflectarrays", *IEEE Antennas and Wireless Propagation Society International Symposium (APS 2009),* Charleston, USA.

E.B.Tchikaya, A.Rashid, H.Aubert,H.Legay,N.Fonseca, "Electromagnetic Modeling of Finite Metallic Grid FSS Structures using Scale Changing Technique", *Progress In Electromagnetics Research Symposium (PIERS)*, 22-26 March 2010, Xi'an, China.

E.B.Tchikaya, A.Rashid, F.Khalil, H.Aubert, H.Legay, N.Fonseca, "Multi-scale Approach for the Electromagnetic modeling of metallic FSS Grids of Finite Thickness with Non-uniform Cells", *Asia Pacific Microwave Conference (APMC),* 7-10 December 2009, Singapore.

E.B.Tchikaya, A.Rashid, F.Khalil, H.Aubert, Maxime Romier, N.Fonseca, “Full Wave Analysis of Large Non-Uniform Metallic Grid FSS Under Oblique Incidence Using Scale Changing Technique”, *Asia Pacific Microwave Conference (APMC),* 7-10 December 2010, Yokohama,Japan.

National Communications

A.Rashid, H.Aubert, H.Legay “ Modélisation Electromagnétique d’un Réseau Fini et Non-Uniforme par la Technique par Changements d’Echelle”, *Journée National Microonde JNM 2009*, Grenoble, France.

A.Rashid, “Electromagnetic Modeling of large Finite and Non-Uniform Arrays using Scale-Changing Technique”, Ecole Doctorale (GEET) Day, Toulouse, 5 March 2009.